UNIVERSITA' degli STUDI di ROMA
TOR VERGATA

Facoltà di Scienze Matematiche, Fisiche e Naturali
Erasmus Mundus Master Course in Astronomy and Astrophysics
(Astromundus)

Master Thesis

Studio della formazione dei Cold Fronts e dei Mini Aloni Radio indotta dall'Oscillazione del Gas Intergalattico nel centro degli Ammassi di Galassie

(Study of the formation of Cold Fronts and Radio Mini-halos induced by the Intergalactic Gas Sloshing in the Cores of Galaxy Clusters)

Candidato:
Khan Muhammad Bin Asad

Relatore Interno:
Dr. Giancarlo de Gasperis

Relatore Esterno:
Prof. Dr. Pasquale Mazzotta

Correlatori:
Dr. Hervé Bourdin
Dr. Chiara Ferrari
Dr. Simona Giacintucci

Anno Accademico 2011/2012

Abstract

Some cool-core non-major merging galaxy clusters host diffuse amorphous radio sources in their central regions ($r = 100 - 300$ kpc) named Radio Mini-halos (MH). MHs are characterized by steep synchrotron spectra. Their diffuse radio emission surrounds a bright radio source associated to the brightest cluster galaxy (BCG). The corresponding radio emitting particles cannot be connected to the central radio galaxy in terms of particle diffusion. It has been proposed that they could result from a relic population of relativistic electrons re-accelerated by MHD turbulence, necessary energetics being supplied by the cool-core region. Later the MHs in two clusters, namely MS1455.0+2232 and RX J1720.1+2638, were found to be confined within the region delimited by the cold fronts (CF), i.e. edges of dense and cold structures in the thermal intracluster gas observed in X-rays. These MHs have also been found to be spatially correlated with the X-ray spiral structure created by gas sloshing at the cluster centre. Gas sloshing is one of the possible mechanism behind the formation of the CFs. Being a turbulent mechanism, it has been suggested that gas sloshing should also be responsible for the re-acceleration of radio emitting electrons. To examine this possibility we analysed *Chandra* X-ray data of six clusters (including the aforementioned ones) that host MHs and correlated them with the corresponding radio data. We found that, beside R1720 and MS1455, the MHs and the CFs in R1504, R1347 and A1835 are also spatially correlated. This is consistent with the hypothesis that the electrons responsible for MH emission could be re-accelerated by sloshing induced MHD turbulence.

Riassunto

Tra gli ammassi non in fase di merger e caratterizzati dalla presenza di una regione fredda centrale (regione detta *cool-core*) ce ne sono alcuni che ospitano radio-sorgenti peculiari e diffuse nelle loro regioni interne ($r = 100 - 300$ kpc). Tali sorgenti radio sono dette mini-aloni (*mini-halos*, MH). I MHs sono caratterizzati da spettri di sincrotrone ripidi. La loro emissione radio diffusa circonda una sorgente radio brillante associata alla galassia più brillante dell'ammasso (*brightest cluster galaxy*, BCG). Le particelle che danno origine all'emissione di sincrotrone diffusa non possono essere semplicemente espulse dalla radio galassia centrale. È stato proposto che esse risultino da una popolazione di elettroni relativistici residuali ri-accelerati da turbolenze magneto-idro-dinamiche (MHD), l'energia necessaria essendo fornita dalla regione del *cool-core*. Successivamente è stato scoperto che i MHs di due ammassi, MS1455.0+2232 e RX J1720.1+2638, sono confinati all'interno della regione delimitata dai cosiddetti *fronti freddi* (*cold fronts*, CF), strutture dense e fredde presenti nel gas termico intra-ammasso osservato nei raggi X. Si è anche scoperto che questi MHs sono spazialmente correlati con una struttura a spirale nella distribuzione del gas osservato in X. Tale struttura sarebbe creata dall'oscillazione (*sloshing*) del gas al centro dell'ammasso. Lo *sloshing* del gas è uno dei possibili meccanismi in grado di spiegare l'esistenza e le proprietà dei CFs. Inoltre, essendo un meccanismo turbolento, è stato suggerito che sia anche responsabile della ri-accelerazione della particelle. Per esaminare questa possibilità abbiamo analizzato i dati Chandra di sei ammassi (compresi i due sistemi menzionati precedentemente) che ospitino MHs e li abbiamo confrontati con i relativi dati radio. Abbiamo trovato che, oltre ai casi già noti di R1720 e MS1455, anche i MHs ed i CFs in R1504, R1347 e A1835 sono correlati spazialmente. Questo risultato è consistente con l'ipotesi che gli elettroni responsabili dell'emissione radio dei MHs possano essere ri-accelerati da turbolenze MHD dovute al meccanismo di *sloshing* del gas.

Acknowledgements

First of all, I would like to thank Prof. Pasquale Mazzotta for giving me the opportunity to work on a very interesting topic and supervising me regarding the goals of the thesis, the path that I should follow to achieve the goals and finally writing the thesis.

I would like to thank Dr. Hervé Bourdin for teaching me how to use the X-ray data analysis software and advising me in countless circumstances throughout this thesis project.

I thank Dr. Chiara Ferrari for helping me to chose the mobility path in this *Erasmus Mundus* master program (*Astromundus*), for providing the analysed radio data and advising me regarding the writing of the thesis.

I thank Dr. Simona Giacintucci for taking the time to analyse the radio data and sending me the end results.

I thank Dr. Giancarlo de Gasperis for helping me with all the administrative tasks.

I would also like to take this opportunity to express my gratitude to Radha Gobinda Chandra (1878-1975) whose life and works inspired me to become an astronomer.

Last but not the least I thank the *European Commission* for financing the *Astromundus* program.

Contents

List of Figures

Chapter 1

Introduction

Galaxy clusters are the most massive gravitationally bound structures in the universe. They contain galaxies, intra-cluster medium and dark matter. Also there are relativistic electrons and magnetic fields in many clusters. Hot thermal gas in the ICM emits in the X-ray band via the thermal bremsstrahlung mechanism. The relativistic electrons gyrating around the the magnetic filed lines emit in the radio band via the synchrotron mechanism.

Some cool core non-major merging galaxy clusters host diffuse radio emission in their central regions with a radius comparable to the size of the cooling region ($r \leq 100 - 300$ kpc) called Radio Mini-halos (MH). Power law spectra of the MHs indicate that the emission mechanism is synchrotron. The intracluster medium (ICM) contains both the relativistic electrons and the magnetic field. The relativistic electrons can be injected into the ICM by past and on-going AGN activity. But they lose energy via radiative and collisional processes. They have a short radiative lifetime (~ 100 Myr) compared to their crossing time of several hundreds of Myrs. Thus it is not well understood how they are still emitting at relativistic energies.

The relativistic electrons can be re-accelerated by turbulence in the central regions of the relaxed cool core clusters. Turbulence induced by cooling flows has been proposed as a possible mechanism for re-acceleration (Gitti et al., 2002, 2004). Later MHs have been found to be confined within the region delimited by the cold fronts (CF) in two clusters, MS 1455.0+2232 and RX J1720.1+2638. Gas sloshing is one of the possible mechanism behind the formation of CFs (Markevitch Vikhlinin, 2007). Being a turbulent mechanism, it has been suggested that gas sloshing should also be responsible for re-acceleration of the electrons (Mazzotta & Giacintucci, 2008).

We analysed Chandra X-ray observations of six galaxy clusters that host radio MHs including the two clusters analysed by Mazzotta & Giacintucci (2008). Then we correlated the X-ray data with the corresponding radio data. The theoretical background and our work are presented in this thesis in seven chapters.

The first chapter gives a general introduction to clusters of galaxies- what are their main components, what techniques are used to observe them and what is the most accepted theory about their origin and evolution.

The second chapter contains description of the X-ray observation of galaxy clusters.

We give a general introduction to the ICM and describe the emission mechanism in the X-ray band and the cooling flow model in brief. Then a detailed description of CFs is presented- especially the procedure that is followed to detect them, the physical model of CF, their classification and formation via gas sloshing. Results of a simulation about the formation of CFs via gas sloshing are also presented.

The third chapter is about the radio observations of clusters. We start with the emission mechanism in the radio band and later give a brief overview of the classification of the cluster radio sources. The properties of the radio MHs are presented in more detail. Then the currently most accepted theory about the origin of the radio sources in the clusters is presented. In the end we focus on the hypothesis that the MHs might have originated from the gas sloshing mechanism. A simulation on the re-acceleration of the relativistic electrons in the MH region is also described.

In the fourth chapter we start with an introduction to the Chandra X-ray telescope and the ACIS instrument. Then we describe the technique that was used to analyse the ACIS-I observations of the clusters. The procedure followed to prepare and analyse the data are also presented in this chapter. A list of the X-ray and radio observations of our targeted clusters and the results are presented in the sixth chapter. We conclude with the general implications of our analyses in the seventh chapter.

Chapter 2

Clusters of galaxies

Clusters of galaxies are the most massive gravitationally bound structures in the universe. Small clusters that contain only a few dozen galaxies are called groups of galaxies. The Milky Way is a member of the Local Group which contains almost 50 galaxies. Most galaxies are members of groups or binary systems. On the other hand large clusters of galaxies contain hundreds or even thousands of galaxies within a radius of 1-2 Mpc. They have four principal components that are studied by different observational techniques. Most massive component is dark matter which contributes to almost 80-90% of the total mass of the cluster. Intracluster medium (ICM) or intergalactic medium is the second most massive component making up about 9-15% of the total mass and galaxies themselves with their numerous stars constitute only 1-3% of the mass of a typical cluster. Additionally there are relativistic electrons and magnetic fields in the ICM that produce radio emission.

Fritz Zwicky first found mass anomaly in the clusters of galaxies. He found the velocity dispersions of the member galaxies in the Coma cluster to be too large to be justified by the total visible or luminous mass in the cluster. A large amount of matter seemed to be hidden from us that is now called dark matter (Zwicky, 1937). After more than three quarter of a century of Zwicky's discovery, dark matter is still a mystery although many other observational evidences of its presence have been found at different scales. Its nature is still unknown except that it is probably cold and collisionless. Its distribution can be directly mapped through gravitational lensing of distant background galaxies by the dark matter rich clusters of galaxies in the foreground (Bartelmann & Schneider, 2001). One of the most direct evidence of dark matter has been found by observing clusters of galaxies. In some merging clusters most of the mass is found to be concentrated in a region completely devoid of luminous matter. Because collisionless dark matter component was separated from the collisional components. One of the most exciting example of such merging clusters is the famous 1E 0657-56, also called the Bullet cluster (Clowe et al., 2006). It has a mass of almost 10^{15} $M_{\odot}$ among which only 1-3% is stellar mass in the member galaxies.

The Virgo cluster is the nearest cluster to our own galaxy and the Coma cluster is the nearest rich cluster. In 1966, X-ray emission was detected from the region around M87 located in the centre of the Virgo cluster. In fact, it was the first extragalactic X-ray source to be detected. In later years more and more X-ray galaxy clusters were

discovered and through the observations of *Uhuru* space telescope it was established for the first time that clusters are prominent X-ray sources. This emission is spatially extended with a size comparable to the size of the distribution of the galaxies in the cluster. Their luminosity is in the range of 10^{43-45} erg/s and does not vary in time. They are emitted via thermal bremsstrahlung mechanism from the hot gas in the ICM. The hot gas has a very high temperature ($\sim 10^8$ K) but low density ($\sim 10^{-3}$ atoms/cm^3).

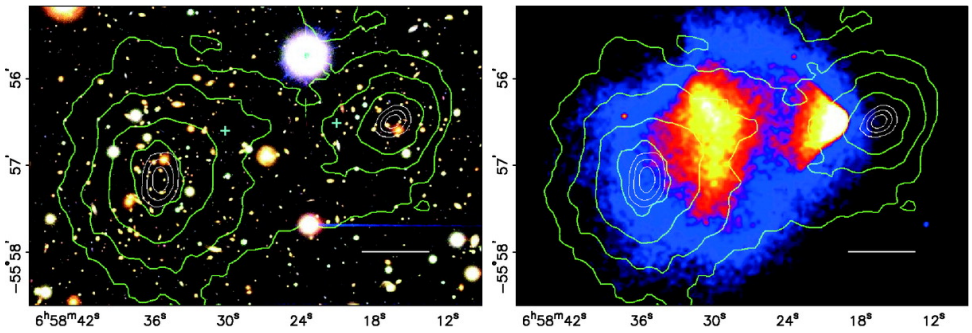

Figure 2.1: *Left panel*: Optical image of 1E 0657-56 or the Bullet cluster taken by Magellan telescopes. *Right panel*: *Chandra* image of the cluster with an exposure time of 500 ks. In both the panels, white bar indicates 200 kpc and green contours show the mass distribution measurement from weak gravitational lensing. Dissipationless stellar component and the fluid-like X-ray emitting plasma (red-yellow-white) are spatially segregated. Galaxy distribution approximately traces the gravitational potential but the ICM plasma does not. From Clowe et al. (2006)

2.1 Optical observations

Frequently cited catalogues of galaxy clusters are the Abell catalogue (Abell, 1958) and the Zwicky catalogue (Zwicky et al., 1961-68). Both of them were compiled by observing an enhancement in the surface number density of galaxies in the *National Geographic Society- Palomar Observatory Sky Survey* in optical band. For inclusion in the Abell catalogue clusters need to satisfy four criteria: they must have a minimum population of 50 members within a magnitude range of m_3 to m_{3+2} (where m_3 is the magnitude of the third brightest member of the cluster), they have to be compact within the Abell radius (1.5 H^{-1} Mpc), should have a nominal redshift between 0.02 and 0.2 and finally they have to be situated in the regions outside the plane of the Milky Way. There are 4,073 rich clusters in the Abell catalogue. Zwicky catalogue also had its own set of criteria.

But these catalogues mainly focus on the northern sky. Later, some smaller surveys have been carried out to find clusters in the southern sky and/or at a redshift higher than 0.2. Digital surveys over large areas of the sky have been performed which are free from subjective selection effects. The APM (Automatic Plate Measuring) Galaxy Survey covered an area of 4300 square degrees in the southern sky and contains over 2 million galaxies (Maddox et al., 1990). The 2dF (Two-degree-Field) Galaxy Redshift Survey (2dFGRS) is a spectroscopic survey conducted using the 2dF facility built by the Anglo-Australian Observatory (Colless et al., 2001). It covers an area of 1500 square degrees selected from the APM survey and contains spectra of 245,591 galaxies.

Richness of a cluster is the measure of its total number of galaxies. But the absolute measurement of the number of member galaxies is very difficult because of the presence of background galaxies. Thus instead of counting the exact numbers, richness is measured by density contrast. The number distribution of the optical luminosities of the galaxies within a cluster is its luminosity function. The differential luminosity function, $n(L)dL$, gives the number of galaxies with luminosities in the range L to $L+dL$. Schechter proposed an analytic approximation to the differential luminosity function,

$$n(L)dL = N^* \left(\frac{L}{L^*}\right)^{-\alpha} e^{-L/L^*} d\left(\frac{L}{L^*}\right) \tag{2.1}$$

where L^* is a characteristic luminosity, $N^*\Gamma(1-\alpha, 1)$ is the number of galaxies with $L > L^*$ and α is the slope of the function. Schechter calculated the value of faint end slope as $\alpha = 5/4$. This function fits the distribution of galaxies in the cluster quiet well if the brightest cD galaxies are excluded.

Various characteristics have been taken into account to construct a morphological classification of clusters of galaxies over the years. But there exists a very crude yet effective one-dimensional classification scheme of the clusters, one that runs from very regular all the way to the irregular clusters. Regular clusters are dynamically more evolved and relaxed than the irregular ones. Among some more concrete classification systems, Rood-Sastry (RS) classification is one of the most frequently used. It is based on the nature and distribution of the ten brightest member galaxies as shown in the following table.

Class	Charecteristics	Example
cD	Dominated by a central cD galaxy	Abell 2199
B	Binary: dominated by a pair of luminous galaxies	Coma
L	Line: at least 3 of the brightest galaxies appear to be in a straight line	Perseus
C	Core: four or more of the ten brightest galaxies form a core	Abell 2065
F	Flat: the brightest galaxies form a flattened distribution on the sky	Abell 2151
I	Irregular: distribution of the brightest galaxies is irregular with no core or centre	Abell 400

Table 2.1: Rood-Sastry morphological classification of galaxy clusters. (Sarazin, 1988)

2.2 Formation and evolution of galaxy clusters

The current standard theory of structure formation holds that at early times universe was almost perfectly homogeneous except for some tiny density fluctuations. It is often argued that these fluctuations were the result of quantum fluctuation in the very early universe which were later boosted by an exponential expansion called inflation to macroscopic scale. As time went on and universe kept on expanding,

these macroscopic density fluctuations grew and at redshift, $z \sim 30$ structure formation began. In the current paradigm of structure formation huge structures like galaxy clusters are formed via hierarchical sequence of mergers of smaller mass units (groups and poor clusters) and continuous accretion of field galaxies driven by the dark matter as it dominates the gravitational field (Ferrari et al., 2008). Pre-existing equilibrium of a cluster is destroyed by periodic interruptions by mergers. After each merger the cluster resumes relaxing toward a new equilibrium state, continuing until it is interrupted again Ricker & Sarazin (2001).

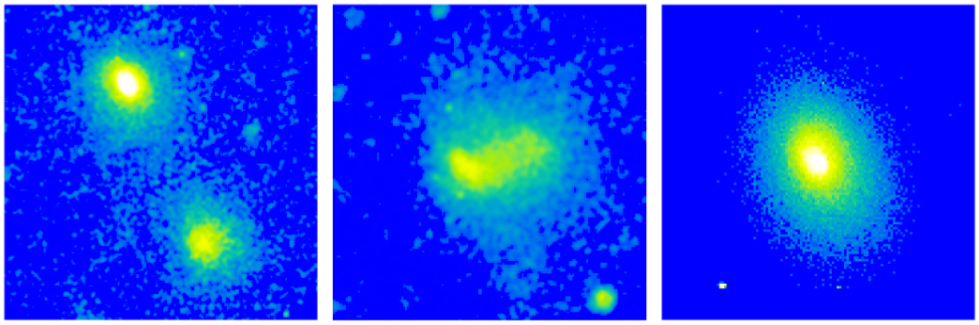

Figure 2.2: Formation and evolution of clusters are driven largely by mergers. Here panels from left to right show: X-ray images of pair of clusters (A399, A401) about to merge, a system (A754) undergoing a merger and a relaxed more massive cluster (A2029) that emerged via mergers in a few Gyr. From Markevitch & Vikhlinin (2007)

Main properties of a cluster are often determined by the initial conditions, dissipationless dark matter (DM) and gravity. So, formation of clusters is represented by models of *DM-driven dissipation-less collapse from cosmological initial conditions in an expanding universe* (Kravtsov & Borgani, 2012). All the models of structure formation need to explain the presence of rich clusters. So far, Kaisers testable hypothesis is successful in doing so (Kaiser, 1986). A complete description of the formation of clusters demand a through understanding of the non-linear evolution of the density fluctuations and baryon physics. During collapse of large regions, gas is heated to very high X-ray emitting temperatures due to adiabatic compression and shocks. Eventually the gas reaches hydrostatic equilibrium. Once the gas is sufficiently dense it can feed star formation in the galaxies by ram pressure stripping. It can also feed accretion into supermassive black holes (SMBH). Formation of stars and SMBH can create very energetic feedback via supernovae and active galactic nuclei. They can heat the ICM and inject heavy metals into it.

Merging of galaxy clusters is the most energetic event in the universe after Big Bang. Major cluster mergers release a gravitational binding energy of almost 10^{64} ergs. Inevitably, they affect the properties of the different components of the cluster including temperature, metallicity, density distribution of the ICM, global dynamics and spatial distribution of galaxies and also star formation rate (Ferrari et al., 2008). Turbulence induced by mergers and other events is of special importance in this thesis, as they accelerate free electrons to an energy high enough to emit synchrotron radiation. Details of this mechanism will be described in chapter 4.

Chapter 3

X-ray observations

3.1 Intracluster medium (ICM)

The most massive baryonic component of a cluster of galaxies is its intracluster medium or ICM which is mainly made of ionized Hydrogen and has a metallicity comparable to that of the Sun. ICM gas has a temperature of $10^7 - 10^8$ K or $1 - 10$ keV. Its particle number density steeply declines from 10^{-2} cm^{-3} in the centre to 10^{-4} cm^{-3} in the outskirts. At this temperature and density the mean free path of electrons ($\sim$ 23 kpc) in the ICM is much shorter than the size (1-2 Mpc) of the cluster. So, the gas in ICM can be treated as fluid. Time-scale for elastic Coulomb collisions between particles ($\sim 3.3 \times 10^5$ years) in the plasma is much shorter than the age (few Gy) or cooling time (compared to Hubble time in the core) of the plasma. So, the free particles can be assumed to have a Maxwell-Boltzmann distribution at the temperature of the gas. The timescale for sound wave propagation ($\sim 6.6 \times 10^8$ years) across the cluster is also shorter than the age of the cluster. So it is likely that the ICM is in hydrostatic equilibrium in the cluster gravitational potential. This assumption allows us to estimate the total cluster mass from its temperature, $T(r)$, and density, $\rho(r)$, profiles.

$$M = -\frac{kT(r)r}{\mu m_p G}\left(\frac{d\ln\rho_{gas}}{d\ln r} + \frac{d\ln T}{d\ln r}\right) \tag{3.1}$$

3.1.1 X-ray emission

X-ray emission in the ICM is produced mainly via three processes: thermal bremsstrahlung (free-free emission), recombination (free-bound) emission and two-photon decay of metastable levels. The radiative recombination emissivity can be calculated using Milne relations as described in (Osterbrock, 1974). The corresponding equation is also given in Sarazin (1988). Two-photon decay continuum comes from the metastable 2s states of hydrogen and helium-like ions. But at high temperature, as present in the ICM, most dominant process is bremsstrahlung which is described in the following section.

Thermal bremsstrahlung

Bremsstrahlung is an electromagnetic emission mechanism that occurs when charged particles with large energies compared to their rest energies are decelerated over a very short distance. Since electrons are much lighter than protons, electron bremsstrahlung is the most common. In bremsstrahlung, a continuous spectrum with a characteristic profile and energy cut-off (i.e., wavelength minimum) is produced. In addition, lines can appear super-imposed, corresponding to the ejection of K and L shell electrons knocked out of atoms in collisions with the high-energy electrons (Eric Weisstein's world of Physics).

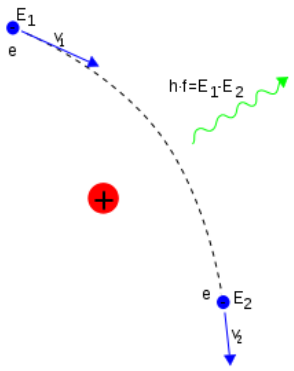

Figure 3.1: A simple schematic diagram of bremsstrahlung radiation. An electron (blue) decelerates while passing near a proton (red). Its energy (E_1) and velocity (v_1) before the interaction is greater than the energy (E_1) and velocity (v_1) after the interaction as it loses some energy ($E_1 - E_2$) via bremsstrahlung radiation. From Trex2001, Wikimedia Commons

As there is thermal equilibrium in the ICM, we can average the single electron speed expression for the emissivity over the thermal velocity distribution and get the expression for thermal bremsstrahlung emissivity. The thermal emissivity at a frequency ν of an ion of charge Z in a plasma with an electron temperature T_g is given by,

$$\epsilon_\nu^{ff} = \frac{2^5 \pi e^6}{3 m_e c^3} \left(\frac{2\pi}{3 m_e k} \right)^{1/2} Z^2 n_e n_i g_{ff}(Z, T_g, \nu) T_g^{-1/2} e^{\frac{h\nu}{kT_g}} \tag{3.2}$$

where n_e and n_i are the number densities of electron and ion respectively. The emissivity is defined by the emitted energy per unit time, frequency and volume,

$$\epsilon_\nu \equiv \frac{dL}{dV d\nu} \tag{3.3}$$

The Gaunt factor $g_{ff}(Z, T_g, \nu)$ corrects for quantum mechanical effects and for the effect of distant collisions, and is a slowly varying function of frequency and temperature given in Karzas & Latter (1961) and Kellogg et al. (1975). From the X-ray spectra and the X-ray flux we can calculate the atomic number density of the ICM gas.

The strongest evidence for bremsstrahlung as the dominant emission mechanism is the strong X-ray line emissions from the clusters. The strong 7 keV Fe line, that is

observed in most of the clusters, cannot be described by any non-thermal mechanism. In the bremsstrahlung model however, this emission occur very naturally if the metallicity ($\sim 0.3\ Z_{\odot}$) is close to the solar metallicity.

3.1.2 Spatial distributions of the cluster components

The ICM gas and the dark matter density distributions of a non-interacting cluster in hydrostatic equilibrium can be described by some functional forms. The X-ray emitting gas component is usually centred on the centre of the cluster. From the early days of X-ray observations it has been known that the X-ray emission from the clusters are diffuse or extended. Density profile of these diffuse X-ray sources can be approximated by the β-model (Cavaliere & Fusco-Femiano, 1976).

$$\rho_g(r) = \rho_{g0}\left[1 + \left(\frac{r}{r_c}\right)^2\right]^{-3\beta/2} \tag{3.4}$$

where ρ_{g0} is the central gas density, r_c is the radius of the X-ray core and β is the asymptotic slope parameter. Assuming isothermality, the gas density profiles of the clusters without cooling flows are represented by a model with $\beta \approx 2/3$ (Ricker & Sarazin, 2001). This profile has a flat core in the centre with typical sizes $r_c \sim 200$ kpc. This description is adequate for one third of all the clusters (Markevitch & Vikhlinin, 2007).

On the other hand, the NFW (Navarro, Frenk & White, 1997) profile allows us to model DM haloes at smaller scales. The density profile of DM haloes on scales from individual galaxies to rich clusters is given by,

$$\rho(r) = \rho_s\left[\left(\frac{r}{r_s}\right)\left(1 + \frac{r}{r_s}\right)^2\right]^{-1} \tag{3.5}$$

where the scaling radius, r_s, and the scaling density, ρ_s depend on the mass of the haloes. r^{-1} dark matter density cusp corresponds to a finite and sharp peak in the centre. This universal density profile is used to approximate the total density (DM+gas) profile of the cluster. Addition of gas might modify this profile, but as DM dominates in the clusters, the total density profile should still be steeper than that of the central gas. After calculating the gas and the total density profiles using equations 3.4 and 3.5, the dark matter density profile can be calculated as,

$$\rho_{dm}(r) = \rho(r) - \rho_g(r) \tag{3.6}$$

The clusters that follow the centrally peaked profile usually have undisturbed ICM and contain a giant elliptical galaxy in the centre marking the position of the dark matter peak. Within around 100 kpc radius of these clusters, ICM temperature declines sharply towards the centre while the gas density and the relative abundance of the heavy elements in the gas increases. Thus a cool, dense and metal rich core is created in the central region. Outside this region the radial temperature profile reverse, i.e. again declines towards the outskirts, but entropy continues to increase.

The ICM gas is usually stable to convection. During convection a bubble rises from the central regions adiabatically keeping its entropy conserved. If entropy of the surrounding material decrease with radius than the rising gas parcel will remain lighter than the ambient medium at equal pressure. So condition for the onset of entropy is a negative entropy gradient which is not the case in usual galaxy clusters. But convection in the clusters can be set off by, for example, central AGN activity. Besides, microscopic transport of heat and momentum in dilute plasmas, like those in clusters of galaxies, is primarily along magnetic field lines. This anisotropic transport can dramatically affect the convective stability of the plasma. In that case convective stability may no longer be determined by the entropy and temperature gradient (Sharma et al., 2009).

3.2 Cooling flow

X-ray luminosity of the ICM gas in a cluster follows the relation, $L_x \propto n_g^2\sqrt{T_g}$ while the energy follows the relation, $E \propto n_g k T_g$. Thus the cooling time of the gas, $t_c = E/L_x \propto \sqrt{T} n_g^{-1}$. Density of the gas decreases with radius. Thus the gas at the centre has shorter cooling time because of its higher density. We can define a cooling radius r_{cool} within which $t_{cool} \sim t_{hubble}$ and the ICM gas can cool effectively. As the gas cools the pressure gets lower, the gas moves further inwards, density increase in the centre and consequently the central gas cools even faster. This inward concentration of gas was named cooling flow.

The observational evidences for cooling flows were, centrally peaked surface brightness profile, low ionization lines in soft X-ray spectra, decreasing temperature gradient towards the centre and low energy absorption features. But no direct evidence of the bulk motion of the gas was found. Homogeneous model of cooling flow suggested that the gas at each radius has one temperature and density and they flow inwards under the pressure of the overlaying gas. It required a constant mass deposition rate. But in that case all the gas of the cluster should be deposited in the centre which is not true. Thus inhomogeneous model of cooling flow was suggested which required gases with different temperature and density to co-exist at every radius. Different phases of gas are in pressure equilibrium. When a given phase cools below 10^6 K it falls out of pressure equilibrium while the other phases continue to flow inwards. Most of the cooling gas actually never makes it to the centre.

The origin of density inhomogeneity in the context of cooling flow model was unknown. Later through higher resolution X-ray observations, no direct evidence of multiphaseness or bulk motion of gas were found. Moreover, no cluster was found with a minimum temperature of less than 1 keV. But the cooling flow model predicted gas with temperature down to almost 0.1 keV. If gas does not cool below 1 keV they will not be deposited in the centre. Thus we will not observe any bulk motion of gas. *Chandra* and *XMM-Newton* observations showed that the central portion of the ICM gas is far from being relaxed as it interacts with the central AGN. In fact, heating the ICM could balance the cooling flow. Two such heating sources are known: interaction with AGN in the central 20-30 kpc and conduction from the large heat reservoirs in the outskirts of the cluster. They might even work together to quench cooling flow as suggested by the mixed models.

3.3 Cold fronts (CF)

Cold fronts were first discovered in the high resolution X-ray image of the merging cluster, A2142. Prominent X-ray surface brightness edges in the central region of this cluster were found (Markevitch et al., 2000) (hereafter M00). A similar edge in A3667 was discovered even before which at that time was interpreted as a shock front. Shock fronts are created when an object or disturbance travels faster than the sound speed within the surrounding medium. Thus gas in the downstream of a shock wave is denser, hotter and have higher pressure and temperature than those of the upstream side. Cold front is just the opposite, the denser and brighter gas on the downstream side is cooler.

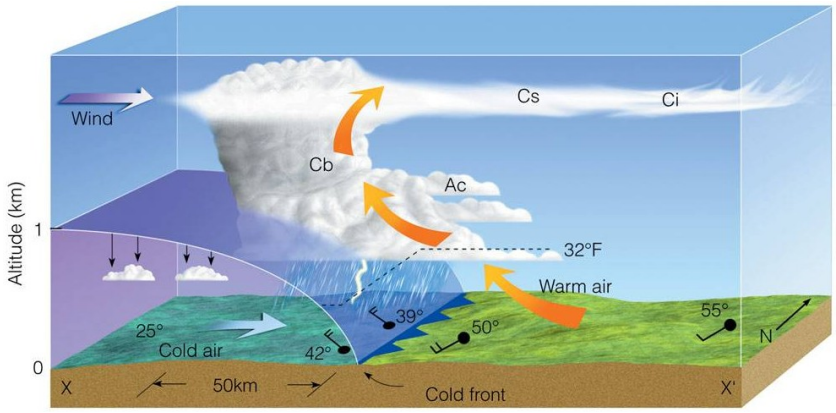

Figure 3.2: Cross section of cold front in the atmosphere of Earth. From *Thomson Higher Education*, 2007 (collected from the educational website of Nolan Atkins)

Interestingly cold fronts were quite well known in the field of meteorology and the definition of the term there is no different than in astrophysics. They form in the atmosphere of the Earth when a moving aggregate of cold air replaces warmer air on its passage. Warmer air on the upstream side is lifted up and over the cold air across the boundary. Frontal boundary is quite steep and can cause intense thunderstorm and shower. A graphic representation of cold front formed in the Earth's atmosphere is shown in figure 3.2.

Before the launch of *Chandra*, sufficiently accurate temperature profiles across the density edges were difficult to achieve. Through *Chandra* observations it was possible for the first time to visualize the jumps clearly and accurately extract their temperature profiles. Cold fronts can be identified by extracting surface brightness and temperature profiles intercepting the brightness edges of an X-ray image. Assuming spherical symmetry of the ICM in the vicinity of the cold front candidates, these projected profiles allow us to model the underlying gas density and temperature using parametric step-like distributions (see details below).

Pressure stays almost constant or changes very little across the cold fronts as an increase in density is compensated by a decrease in temperature in the ideal gas equation. As an ideal example, the X-ray images of A2142 and A3667 are shown in figure 3.3. Presence of two sharp brightness edges can be inferred from the image of A2142, one in the north-west and other in the south of the cluster centre. In A3667,

a prominent edge is visible to the south-east of the centre.

Temperature and X-ray brightness profiles extracted from the regions around the cold fronts in A2142, their corresponding best-fit density models and the respective pressure profiles are shown in figure 3.4. The regions from where they were extracted are shown by red sector annuli in panel (a) of the figure. Brightness profiles of both the edges correspond to the projection of an abrupt, spherical jump of the gas density. Best-fit radial density models are shown in panel (d) and the projections of the density at different radii are overlaid on the brightness data as histograms. As it is impossible to know the exact three-dimensional geometry of the edge, several assumptions need to be made for such kind of fitting. First, that the curvature of the discontinuity surface along the line of sight is the same as in the sky plane. Second, that the center of the radial profiles and 3D models coincide with the center of curvature of the front which is often offset from the cluster center.

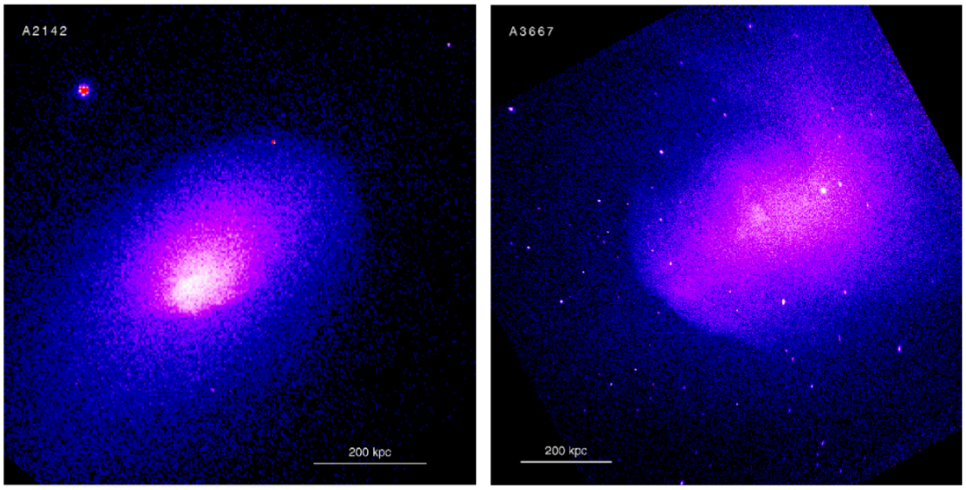

Figure 3.3: Chandra X-ray images of the merging clusters, A2142 and A3667. Two density edges are visible in A2142, one in the north-west between black and blue, other in the south of center between purple and blue. A very prominent edge is visible in A3667 to the south-east of center. From Markevitch & Vikhlinin (2007)

The temperature profiles in the example of A2142 illustrate the behaviour of a cold fronts with respect to a shock front. On the basic assumptions of thermalized shock energy, properties of the ICM across a shock front can be described by Rankine-Hugoniot jump conditions. Consider an element of the surface of a shock. The tangential component of the velocity is continuous at the shock. So a frame is used in which the element of the shock is stationary and the gas has no tangential motion. Let the subscripts 1 and 2 denote the pre-shock and post-shock gas, thus $v_1 = v_s$ is the transverse velocity of the pre-shock gas. Considering the gas to be perfect fluid on either side of the shock jump conditions can be expressed by the following equations deriving from the mass, momentum and energy conservation laws,

$$\frac{P_2}{P_1} = \frac{2\gamma}{\gamma+1}M^2 - \frac{\gamma-1}{\gamma+1} \tag{3.7}$$

$$\frac{v_2}{v_1} = \frac{\rho_1}{\rho_2} = \frac{1}{r} = \frac{2}{\gamma+1}\frac{1}{M^2} + \frac{\gamma-1}{\gamma+1} \tag{3.8}$$

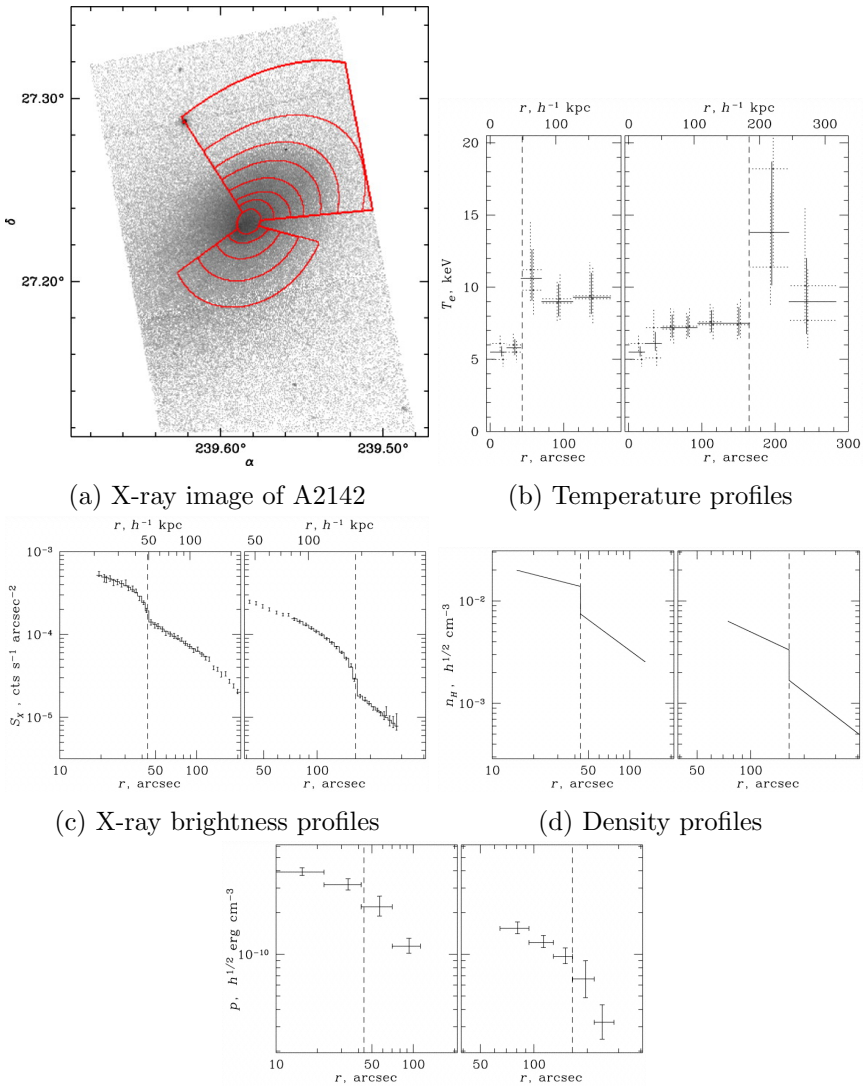

(a) X-ray image of A2142

(b) Temperature profiles

(c) X-ray brightness profiles

(d) Density profiles

(e) Pressure profiles

Figure 3.4: X-ray image and different profiles extracted from the two sector annuli overlaid on the image. There are two edges in the cluster, southern and north-western. Starting from panel (b), in all panels left box corresponds to southern and right box to north-western edge. In the brightness profile, histograms represent the best-fit model. Vertical dashed lines show the position of the density jumps, i.e., cold fronts. From Markevitch & Vikhlinin (2007)

where $r \equiv \rho_2/\rho_1$ is the density jump, γ is the adiabatic index (in our case 5/3 for mono-atomic gas) and M is the Mach number. After defining temperature jump to be $t \equiv T_2/T_1$ we can express the jumps as,

$$t = \frac{\zeta - r^{-1}}{\zeta - r} \tag{3.9}$$

or,

$$r^{-1} = \left[\frac{1}{4}\zeta^2(t-1)^2 + t\right]^{1/2} - \frac{1}{2}\zeta(t-1) \tag{3.10}$$

where $\zeta \equiv (\gamma+1)/(\gamma-1)$.

For the North-West edge of A2142, $r \sim 2$ and $T_2 \sim 7.5$ keV as observed inside the edge. If it was a shock the pre-shock temperature would be $T_1 \sim 4$ keV according to the aforementioned formulae. But the observed value is not only significantly different than this but also completely opposite in terms of jump. As found from the Chandra observation, and shown in the profiles, temperature of the outer less dense gas is actually higher than that of the inner gas. It is true also for the southern edge of A2142 and also for the South-East edge of A3667.

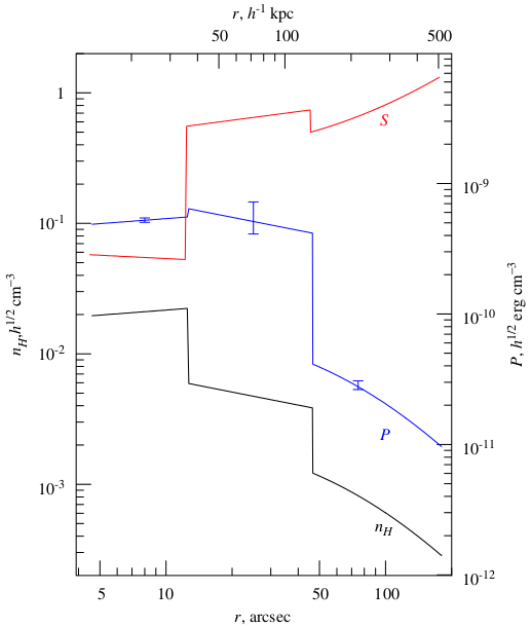

Figure 3.5: Gas density (black line), thermal pressure (blue) and specific entropy (red) profiles across a narrow sector of 1E 0657-56 containing a cold (inner edge) and a shock (outer) front. From Markevitch & Vikhlinin (2007)

As these edges could not be described by the traditional shock scenario, some other mechanisms had to be proposed to explain their nature and origin. As mentioned before, no significant pressure jump is observed across these edges, meaning that the gases on the two sides of the front are in pressure equilibrium. In shock front, however, a large pressure jump is observed. On the other hand, entropy jump can be rather mild in weak shocks, but almost always substantial in cold fronts. Because cold fronts are actually contact discontinuities between two gas aggregates with different entropies, one of them could be the cool core of a cluster or sloshing gas form inner radius. This contrast between cold and shock front is evident in the gas density, thermal pressure and specific entropy profiles across a narrow sector in the famous Bullet cluster or 1E 0657-56 as shown in figure 3.5. The sector contains a cold front at inner radius and a shock front at outer radius. In both the edges, there is substantial density jump. Pressure is almost constant across the inner edge but decreases substantially at the outer edge. In contrast, entropy increases very rapidly at the inner edge compared to the outer edge.

Another hint about the nature of cold front came from the observation of the photon image of A2142. It is obvious from the left panel of figure 3.3 that the NW edge of the cluster is shaped like a comet, as if the surrounding gas is flowing around the

inner comet-like gas aggregate. Based on these kind of observations M00 proposed that cold fronts are *contact discontinuities at the boundaries of the gas clouds moving sub- or transonically through a hotter and less dense surrounding gas.* The term 'cold front' was used in the context of galaxy clusters by Vikhlinin before to describe the discontinuity in A3667. So far, cold fronts have been discovered in at least 2/3 of the known X-ray galaxy clusters.

3.3.1 A simple model of cold front

A cut of the the gas flow surrounding a cold front in the ICM is shown in figure 3.6. Flow of hotter ambient gas around a stationary blunt body is shown in panel (a). Stationarity of the dense and cool gas is simplifying assumption. The flow creates several distinct regions. A stagnation region is formed near the tip of the gas body (zone 0) where the velocity component along the axis of symmetry becomes zero. The external hotter gas slows down at this leading edge but re-accelerates as it is squeezed to the sides. In the stagnation region thermal pressure increases as one goes closer to the front and is continuous across the front. But still one may observe jumps in pressure profile of a moving cold front as the stagnation region is too small and difficult to detect because of line-of-sight projection.

Density and temperature of the ambient gas increase near the stagnation region as the gas is adiabatically compressed. Pressure of the outer gas is taken to be the pressure in the free stream region (zone 1). Grossly speaking, thermal pressure of the gas inside the cold front is equal to the combined thermal and ram pressure of the gas outside. So, difference of thermal pressure across the front directly gives the ram pressure exerted on the blunt body by the flow. This in turn gives the speed of the cloud. The ratio of the thermal pressure at the stagnation point (p_0), which is the same as the pressure inside the cloud (zone 0'), and in the free stream (p_1) directly gives the speed of the cloud. Formula for this ratio is given in equation 3.12 where M_1 is the Mach number of the cloud relative to the sound speed in the free stream region and γ (=5/3 for mono-atomic gas) is the adiabatic index. The ratio is shown in panel (b) of figure 3.6 as a function of M_1.

$$\frac{p_0}{p_1} = \left(1 + \frac{\gamma - 1}{2} M_1^2\right)^{\frac{\gamma}{\gamma - 1}}, \; M_1 \leq 1 \tag{3.11}$$

$$\frac{p_0}{p_1} = \left(\frac{\gamma + 1}{2}\right)^{\frac{\gamma+1}{\gamma-1}} M_1^2 \left(\gamma - \frac{\gamma - 1}{2M_1^2}\right)^{\frac{-1}{\gamma-1}}, \; M_1 1 \tag{3.12}$$

Mach number of the gas cloud has been determined for several clusters hosting cold fronts. For example, for A3667 (Vikhlinin et al., 2001) calculated $M_1 = 1 \pm 0.2$ which corresponds to a cloud velocity of 1400 ± 300 $km\ s^{-1}$. Mazzotta et al. (2003) measured a value of 0.75 ± 0.2 for the Mach number in 2A 0335+096.

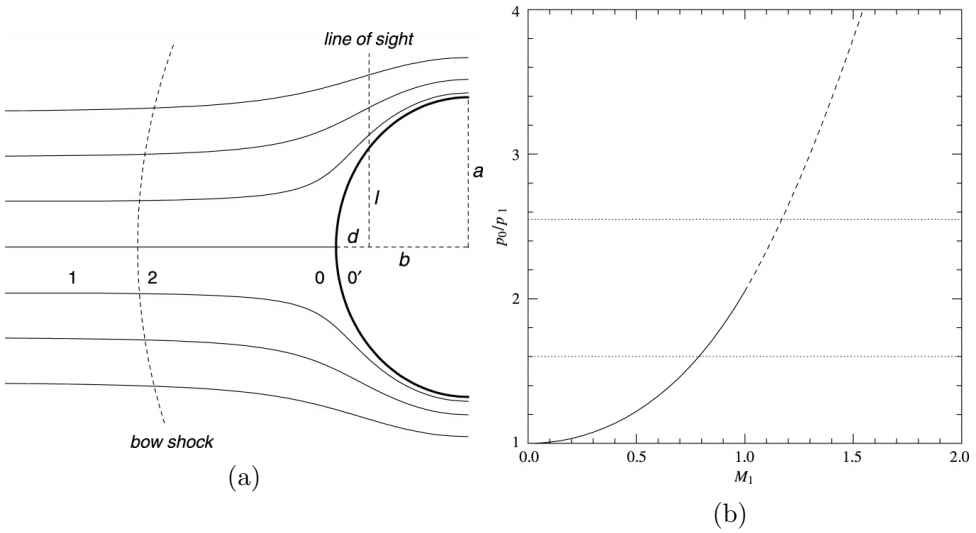

Figure 3.6: (a) Geometrical representation of the flow of gas around and past a spheroidal cold front. Zones 0, 1, and 2 represent regions near stagnation point, in the undisturbed free stream and past the possible bow shock. Point 0' is inside the cold gas. (b) Ratio between the pressure near stagnation point and in the free stream as a function of Mach number in the free stream. The solid and dashed lines correspond to the sub- and supersonic regimes respectively. From Vikhlinin et al. (2001)

3.3.2 Classification of cold fronts

Sufficient number of cold fronts have been discovered to devise a classification scheme. At least six distinct type of cold fronts have been roughly discussed in the (Markevitch & Vikhlinin, 2007) review (hereafter MV07). But they can be broadly categorized into two classes: merger and non-merger cold fronts.

Merger cold fronts

Cold front is the boundary between two gas aggregates that did not mix. These two gases can come from two different clusters or the same cluster. The first kind form in major merging clusters, that is undergoing discernible violent merger, while the later form in non-major merging cool core clusters. In the major-merging clusters CFs can appear to be in two phases: stripping and slingshot. On the other hand, in non-major merging clusters they appear mainly via gas sloshing.

Stripping CFs: When two sub-clusters merge, the outer regions of their gas halos are shocked and stopped, but gas in the inner regions are often dense enough to resist the penetration of shock. These survived gases stay attached to their dark matter hosts and are subjected to ram pressure of the ambient hotter gas. Ram pressure pushes the gas remnants out of their gravitational potential wells. The sub-clusters can be stripped out of their gas completely depending on the gravitational potential, density of the ambient gas and the merger velocity as $P_{ram} = \rho_{amb} v^2$. If it survives, it will be dragged along by gravity lagging behind its dark matter peak. The ambient gas will flow around it creating a cold front. This is the stripping stage of cold fronts. Examples

include 1E 0657-56 (2.1).

Slingshot CFs: Ram pressure is highest when the survived sub-cluster reaches the nearest point to the center of the other cluster, because density is higher towards the center. As it gradually moves away from the center, it enters lower density regions. Thus ram pressure acting on it decreases very rapidly and it rebounds like a slingshot. Utilizing its stored potential energy in this free state it will actually overtake the dark matter sub-halo. The forward region of the sub-cluster will move away from the potential minimum and expand adiabatically and cool, further enhancing the temperature contrast at the edge. It can be called ram pressure slingshot stage of CFs. Examples include A168, where the gas peak is actually located ahead of the dark matter peak instead of lagging behind it.

Sloshing CFs: Many cooling flow clusters host cold fronts but do not show any sign (vigorous gas flow, moving sub-cluster remnants etc.) of recent merger. Density jump across these fronts are very subtle compared to the major-merger CFs and they are mostly found inside or on the boundaries of the cool core, i.e. within a scale of 100 - 200 kpc from the center. They are arc-shaped and usually centred on the gas density peak of the cluster. Sometimes, several such CFs are found at different radii from the center. They are very common, CFs have been found in more than half of the cooling flow clusters. Considering out limitation in detecting CFs because of projection effects, we can say that most, if not all, of the cooling flow clusters host one or multiple CFs. They are called sloshing cold fronts because they are created by the sloshing motion of the central cool gas in the potential well of the cluster. For the purpose of my thesis these cold fronts are most important. So details of their origin and evolution will be described in a separate section.

Non-merger cold fronts

Even though sloshing CFs are not the direct result of a merger, some of them, if not all, require a past minor merger. But merging is not the only way to get CFs. There are speculations about CFs formed by very different mechanisms. Three such CF types have been mentioned in MV07.

AGN-induced CFs: Central gas of a cooling flow cluster can be disturbed very easily. Theoretically, sloshing can also be induced by bubbles blown by the central AGN. It is already known that jets from radio loud AGNs inflates bubbles or lobes in the ICM by replacing the X-ray emitting plasma. These bubbles appear as holes in X-ray image. Possibility of inducing sloshing through this bubble has bot been studied well yet. But some works suggest that it is possible. A a bubble rising due to buoyancy force from the inner region may push the low-entropy inner gas to outer regions. CFs can be formed when these pushed low-entropy gas encounters higher entropy gas at the outer regions.

Ripples: It has been suggested that sound waves from the central AGN explosion can create very subtle brightness edges as observed in the Perseus cluster. Because of this subtelity they are largely affected by projection and temperature

jump is also negligible as the shocks are weak. So they are very difficult to detect.

Iron front: X-ray image of the galaxy group named NGC 507 showed a brightness edge of very different kind. Its spectral analysis showed that the brightness edge is mainly due to difference in metal abundance. Gas on one side of the edge very high abundance of heavy elements. Thus it is called iron front.

3.3.3 Gas sloshing

As mentioned before, CFs may form in the cool cores of the non-major merging clusters within a radius of around 100 kpc. Markevitch et al. (2001, hereafter M01) observed one such cold front in A1795, one of the most relaxed nearby galaxy clusters. They realized that the gas forming the cold front is not in hydrostatic equilibrium in the gravitational potential of the cluster. X-ray surface brightness, temperature, best-fit density, pressure and mass profiles within a sector along this cold front has been shown in figure 3.7.

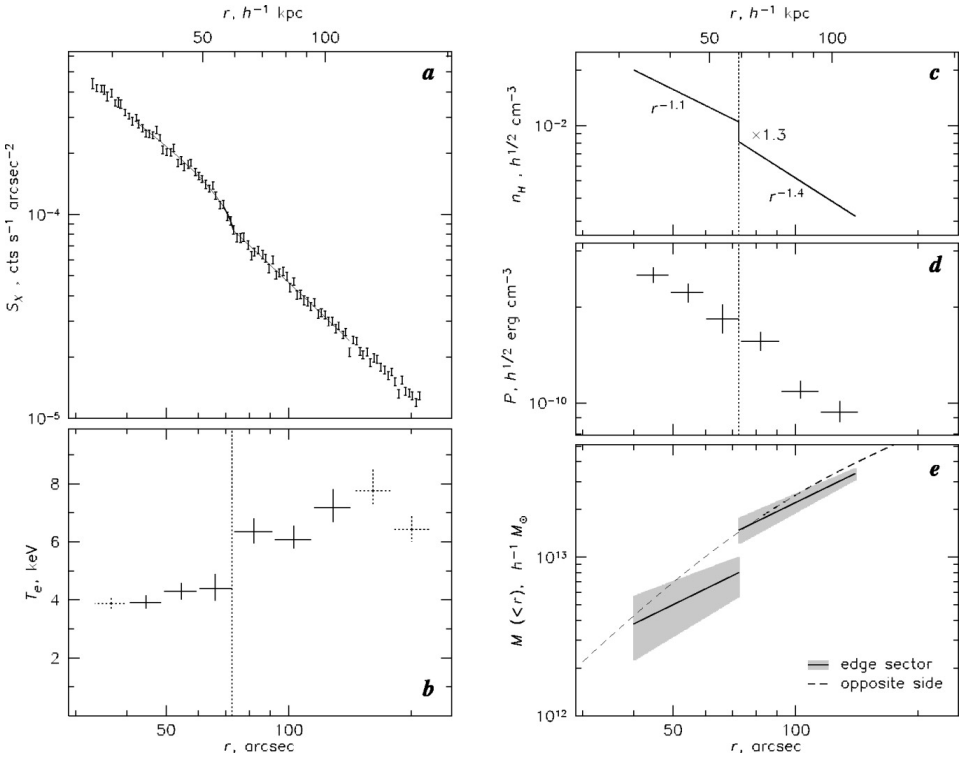

Figure 3.7: All the profiles have been extracted from the sector containing the cold front in A1795. (a) X-ray surface brightness profile, the solid line is the best-fit density model shown in panel (c). (b) Projected gas temperature profile. (d) Pressure profile and (e) Total enclosed mass as a function of radius calculated with the assumption of hydrostatic equilibrium. Solid lines represent the profiles across the cold fronts, while the dashed line show the profile in an opposite sector where no edged have been observed. From Markevitch et al. (2001)

From the brightness (a) and temperature (b) profiles presence of a cold front can be inferred. It also fits perfectly with a density model. From the pressure profile we see

that pressure across the cold front is completely continuous which means that there is almost no relative motion between the cool dense gas and the ambient medium. As the two gas parcels are in pressure equilibrium one might expect them to be also in hydrostatic equilibrium in the cluster gravitational potential. But the mass profile tells a different story. Mass profile has been calculated from the temperature and density profiles under the assumption of hydrostatic equilibrium from equation 3.1. Solid lines represent the enclosed mass within different radii in the sector containing the cold front while the dashed line show the mass profile in a sector on the opposite side of the center where there is no density discontinuity. If the gas parcels are in hydrostatic equilibrium in the cluster potential than mass profiles from both the sectors should be the same. Indeed, it is the same outside the cold front. But inside the cold front mass profile is very different indicating that it is not in hydrostatic equilibrium. But as it is in pressure equilibrium we can say that it has zero velocity. Thus M01 speculated that the gas has now reached the highest distance from the center where the velocity is zero but the centripetal acceleration is not. It was not first observation of un-physical mass discontinuity, Mazzotta et al. (2001) observed a similar discontinuity in the relaxed cluster RX J1720.1+2638.

Gas sloshing mechanism was proposed by M01 to explain this discontinuity. According to the proposition, the cold front forming gas was offset from the central dark matter peak by some disturbance and is now sloshing with respect to the potential minimum. Sloshing motion is very simple to understand in terms of a glass full of liquid. The liquid sloshes inside the glass when a disturbance is introduced, just by stirring it. Observation of cool dense gas at its maximum displacement with zero velocity but non-zero centripetal acceleration is consistent with sloshing scenario. Also a cool gas filament extending from the central cD galaxy of A1795 towards the cold front has been observed which suggests that much of the central gas is actually flowing around the cD galaxy through sloshing.

But for this scenario to work, first the central gas peak has to be offset by some disturbance. One of the most popular explanation is the in-fall of sub-cluster in the remote past. Bubbles in the ICM induced by a central AGN was also proposed as a mechanism for offsetting the gas peak. But in two of the most undisturbed clusters, A2029 and A1795, neither a merger nor central AGN activity was visible. Thus to understand the process more clearly we have to resort to simulations.

3.3.4 Simulation of gas sloshing

We do not observe clear sign of major merger in the relaxed cooling flow clusters of galaxies hosting cold fronts. But even than the onset of gas sloshing can be the result of a minor merger in the remote past. Thus an interesting objective of a simulation could be to check if a minor merger can create disturbance in the central gas peak without leaving any trace of merger elsewhere. One such simulation was presented by Ascasibar & Markevitch (2006) (hereafter AM06). Their simulation showed that:

- Cool gas at the center of a cluster can be easily set off by a minor merger.
- Cold fronts formed due to sloshing of this offset gas can persist for gigayears.

- Only necessary condition is a steep entropy profile of the main cluster which is usually the case in cooling flow clusters.
- Even if the in-falling sub-cluster has no gas during core passage, the gravitational disturbance sets the main mass peak (gas and dark matter together) in motion relative to the surrounding gas.
- A rapid change in the direction of motion of this offset peak occurs after the core passage of the in-falling sub-cluster. Due to sudden change in ram pressure the cool gas peak is displaced from the dark matter peak.
- If impact parameter is non-zero the cool gas acquires angular momentum and follow a spiral pattern while sloshing.
- If the sub-cluster retains its gas during the initial phase of the merger, the cool dense gas of the main cluster us more easily set off from the DM peak. Subsequently, some of that offset gas, and maybe even some gas from the sub-cluster, fall back towards the DM peak and start sloshing. But in this case some tracse of the merger will be left.

Based on this observations from the slices of the simulation they could conclude that, *cold fronts at the centres of relaxed clusters, often spiral or concentric arc in shape, are probably caused by encounters with small sub-halos stripped of all of their gas at the early in-fall stages.* Some details of the simulation will be described in the following sections. We will start with the gasless sub-cluster in-fall scenario as it is the simplest and most relevant to the thesis.

Figure 3.8 shows some results from a slice of the simulation of the in-fall of a gasless sub-cluster onto a main cluster 5 times more massive, with an impact parameter of 500 kpc. First core passage of the sub-cluster takes place 1.37 Gyr after the beginning of the simulation run at a distance of 150 kpc from the main cluster center.

Gas-DM displacement

In figure 3.8 we see that the sub-cluster make two passes near the center around 1.4 Gyr and 4.2 Gyr from the beginning of the simulation run. During the first passage, the gas and DM peak swing along a spiral trajectory relative to the center of mass (white cross) of the main cluster. The DM and gas feel the same gravitational attraction and start to move towards the sub-cluster. But after the core passage direction of their motion quickly changes (compare the directions of arrows in the figure at t=1.43 and 1.6 Gyrs). For the gas peak it means a change on the direction of ram pressure. We see that at 2=1.6 Gyr direction of ram pressure is upward in contrast to the previous downward direction. Due to this change the gas peaks shoots up from the potential minimum of the cluster in a ram-pressure slingshot, similar to the one described in section 3.3.2. Actually there is another weak shock created by the sub-cluster in-fall that works with ramp pressure to set off the gas peak as described in AM06. The first cold front appears when the offset gas starts falling back towards the DM peak as will described in the following section. Form the figure it should be noted that the first CF appears at t=1.7 Gyr.

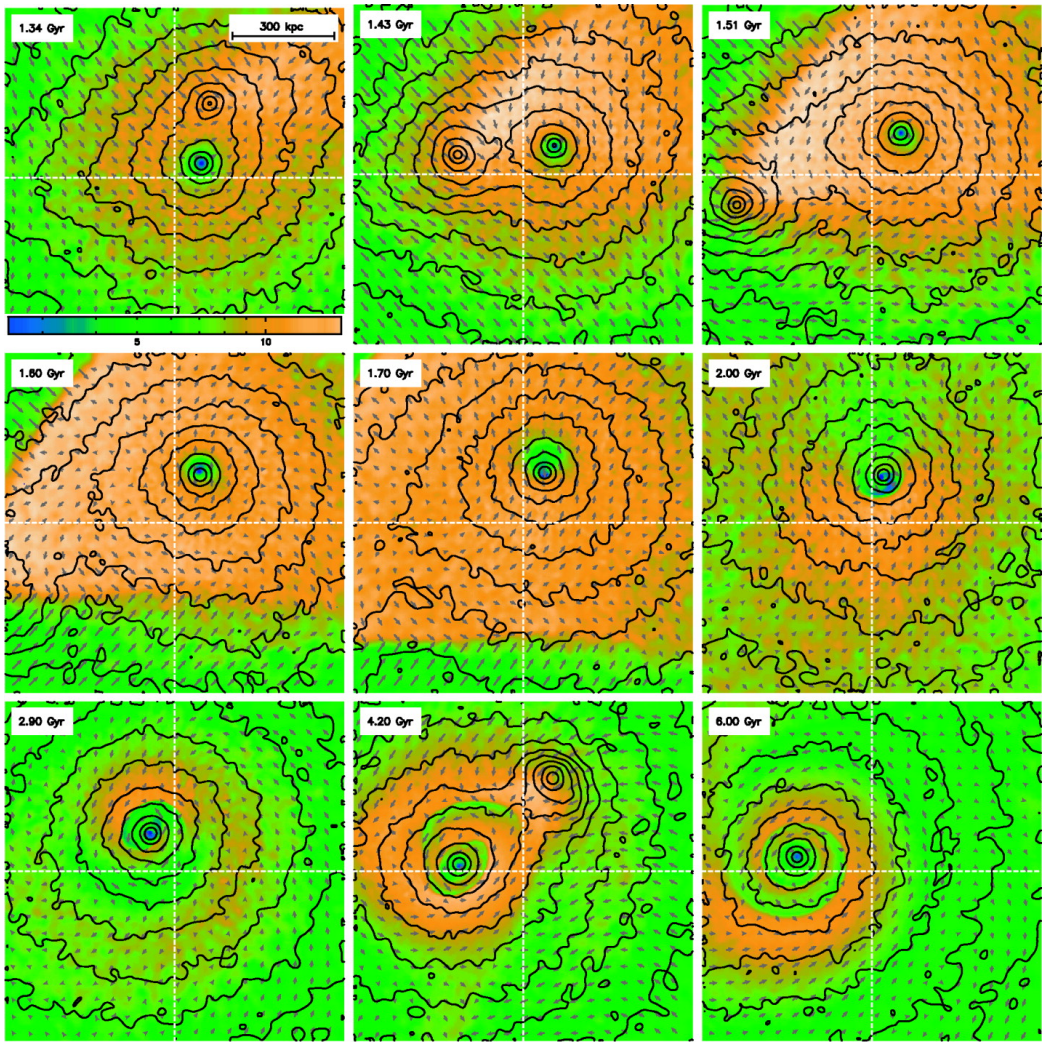

Figure 3.8: Evolution of cold fronts induced by the in fall of a gasless sub-cluster. The main cluster is 5 times more massive than the sub-cluster and the impact parameter is 500 kpc. This color map shows the gas temperature in a slice of the simulation in the orbital plane. Temperature scale is shown below the first panel in keV. Arrows represent the gas velocity field with respect to the dark matter peak. Contours (drawn with a separation of 2) represent the local dark matter density. Intersection of the white dashed lines show the center of mass of the the DM particles of the main cluster. From Ascasibar & Markevitch (2006)

Onset of gas sloshing

When the sub-cluster moves further away from the main cluster and the displacing force diminishes, the displaced gas peak begins to fall back towards the potential minimum. Details of this motion has been shown in a zoomed-in-view of the central region of the simulated cluster at several moments in time in figure 3.9. This scenario should be true for clusters like A2029. The first panel of the figure shows the temperature map at 1.6 Gyr after start of the simulation run, i.e. after the initial displacement of gas peak from the DM peak.

The displaced cool gas expands adiabatically as some portion of it is carried further away due to the flow of ambient gas. But the coolest portion of the gas turns

around and start sinking towards the potential minimum somewhat like an onset of RayleighTaylor instability (RTI). Onset of RTI can be understood by a scenario of two layers of immiscible fluid, the heavier on top of the light one and both subject to gravity. The equilibrium here is unstable to certain perturbations or disturbances. An unstable disturbance will grow and lead to a release of potential energy, as the heavier material moves down under the effective gravitational field, and the lighter material is displaced upwards. Something like this occurs in the simulation first at $t = 1.6$ Gyr and again at $t = 1.8$ Gyr from the opposite side. At 1.7 Gyr, the downward moving cool gas is subjected to ram pressure of gas from the opposite side which are still flowing upwards. Thus the cool dense gas is slowed down and spreads sideways into the regions of lower pressure to form a structure like a mushroom head. It happens whenever a gas jet flows through a less dens gas according to Bernoulli's principle which says, an increase in the speed of a fluid occurs simultaneously with a decrease in pressure or a decrease in the fluid's potential energy. The front edges of these mushroom heads are sharp contact discontinuities called cold fronts.

Emergence of multiple cold fronts

At 1.8 Gyr, we can see that the densest lowest entropy gas in the mushroom head again separates from the rest and starts sinking back towards the DM peak. A structure in the center of the Ophiuchus cluster is somewhat similar to this scenario. In the meantime the rest of the gas of the mushroom head continues to move outwards expanding adiabatically into the regions of lower pressure in the ICM. At 1.9 Gyr this upward moving gas again encounters downward moving hotter gas from the opposite side and like before spreads into a mushroom like structure. The stem of the mushroom is the forward flow of the cool gas while the head is the region where it slowed by ram pressure of the ambient gas.

This process repeats itself and every time the velocity of the densest, lowest entropy gas is reversed with respect to the outer higher entropy gas, a contact discontinuity is formed along the mushroom heads giving rise to multiple cold fronts in the center of the same cluster. As obvious from the figures, the mushroom heads are created on progressively smaller linear scales. Sloshing of the dense cool gas closer to the center occurs with a smaller period and amplitude than that of the gas initially at higher radii.(Churazov et al., 2003) This difference in period brings different gas phases into contact who had initially different off-center distances and entropies. One should remember that DM peak also has an oscillation about the center of mass due to the flyby of the sub-cluster but with a very large period. DM oscillation has a period of 1 Gyr compared to only 0.1 Gyr for the sloshing gas. So DM distribution in the core stays centrally symmetric and the cool gas sloshes back and forth. But DM oscillation can supply some kinetic energy to the sloshing gas.

Now we know how multiple cold fronts form by sloshing motions. But still the precise physical mechanism has not been questioned yet. The question to ask here is, how exactly an initially continuous gas distribution becomes a sharp contact discontinuity? In case of merging cold fronts it is understandable that, tangential flow of gas flow around an in-falling dense gas sub-cluster may remove the outer layers of the sub-cluster's gas until it reaches the radius where the pressure in the cold gas equals the pressure outside. But at the stagnation region (see figure 3.6)

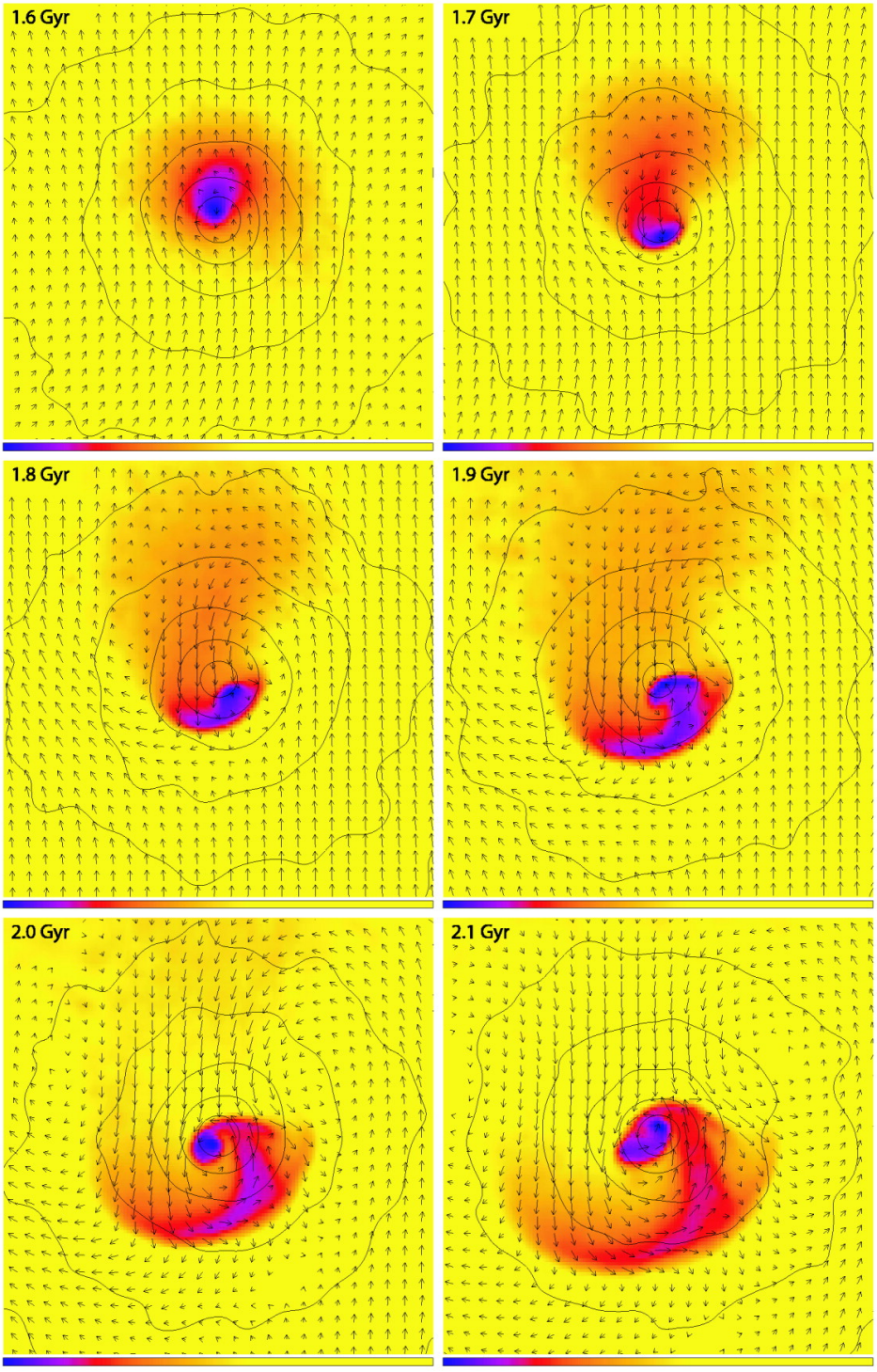

Figure 3.9: Zoomed-in-view of the temperature slices of the simulated cluster (same as in figure 3.8). Blue is 1 keV and yellow is 7-9 keV. Contours represent dark matter density field. The length and direction of the arrows represent the magnitude and direction of the ICM gas velocity respectively, longest arrow stands for $v = 500\ km\ s^{-1}$. Size of the panel is 0.25 Mpc. The velocities are subsonic, as, for example, sound speed at $T = 7 - 9$ keV is $1300 - 1500\ km\ s^{-1}$. From Ascasibar & Markevitch (2006)

of the sloshing cold fronts, there is no stripping. To answer the question we have to focus on figure 3.10. The three panels correspond to the simulation at three different times.

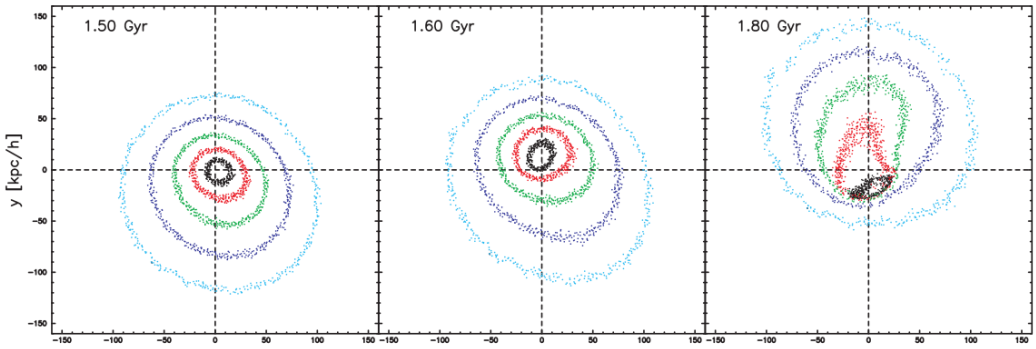

Figure 3.10: Evolution of the simulated particles shown on the merger plane for an in-fall of gasless sub-cluster. Emergence of a sharp contact discontinuity is seen on the right panel. From Ascasibar & Markevitch (2006)

1.55 Gyr is the approximate moment when, after core passage of the sub-cluster, the cool dense gas of the main cluster turns around and starts to fall back towards the DM peak and encounters ram pressure from the ambient gas. Ram pressure is same for each cubic centimetre of the gas in the core near the axis of symmetry assuming subsonic motions. So, denser gas experiences a smaller resulting acceleration. Thus a velocity gradient is produced inside the dense gas along the direction of the force (in the figure that would be downward direction). Then, the lower density outer portion of the cool gas parcel is squeezed to the sides as shown on the right panel of figure 3.10. Thus the inner denser gas gradually comes out and finally comes into contact with the ambient medium. Based on the simulation data AM06 concluded that, *whenever a smooth gas density peak encounters a flow of ambient gas a contact discontinuity quickly forms by "squeezing out" the gas layers near the future stagnation point that are not in pressure equilibrium with the flow. Away from the axis of symmetry of the cold front, such gas is stripped by the shear flow.*

Spiral structure

We can see a clear spiral pattern in figure 3.8 created by the central cold fronts. This picture is consistent with the observations of A2029 (Fig. 14 of Clarke et al. 2004) and Perseus cluster (Fabian et al. 2006). Simulation of AM06 showed that the only condition for getting such spiral structure is a non-zero impact parameter which is defined as the perpendicular distance between the path of the in-falling sub-cluster and center of mass of the main cluster. Because of this distant flyby, cool central gas of the main cluster acquires some angular momentum and cannot fall radially back to the potential minimum. That's why cold fronts are not concentric, rather takes a spiral structure.

Initially there is no coherent spiralling motion as each edge is independent. But as times goes by, circular motions that are against the average angular momentum diminish and mushrooms become more and more lopsided. On large scale it really

looks like a huge spiralling-in flow of cool gas. Low entropy gas flows from one mushroom head to the smaller-scale cap through the stems of the mushrooms.

3.3.5 Summary

Based on the simulations and good agreement with the observations we can come to several conclusions about the origin and evolution of cold fronts and motion of the sub-cluster as pointed out in Johnson et al. (2012):

1. The first cold front does not form until almost 0.3 Gyr after the closest approach of the sub-cluster. For proof compare the panels at $t = 1.6$ Gyr and $t = 1.9$ Gyr of figure 3.9.
2. Cold fronts are formed at successively inner radii. That means, the CF that formed first is always at a higher radius than the ones formed later. So, the distance of the outermost CF from the X-ray peak and the time it takes for sloshing gas to reach there can give us some idea about the time when the sub-cluster passed through the main cluster.
3. The first CF is always formed on the opposite side of the cluster as the initial disturbance induced by the sub-cluster. The reason is, initial displacement of the cool gas peak occurs in the same side as the pericenter of the sub-cluster. But CF forms when the gas peak overshoots the DM peak and reach the opposite side of the cluster.
4. The inclination of the cluster's merger axis with respect to our line of sight dictates how the cold fronts will appear to us. If the merger occurs in the plane of the sky, cold fronts will appear like spiral inflow while for a merger along the line of sight they will appear as concentric crescent shapes. A combination of these two scenarios will be visible is the merger occurred at a certain angle with respect to our line of sight or the plane of the sky.

Chapter 4

Radio observations

Galaxy clusters can host diffuse sources of radio emission. The first diffuse cluster radio source was detected in 1959 by Large et al. while surveying the Coma cluster of galaxies using 250 ft. (70m) telescope in the Jodrell Bank Observatory. The source was named Coma C (figure 4.2). Later its existence was confirmed by Wilson (1970) who also understood that its emission is diffuse and not associated with any member galaxies of the cluster. After that other radio telescopes with higher sensitivity and resolution have been used to study these sources. So far, 42 radio halos have been discovered, and 39 clusters show at least 1 radio relic (for a total of 50 relics) (Feretti et al., 2012). Radio spectrum of their emission follows a power law indicating that the emission mechanism is synchrotron (which will be described in section 4.1). The presence of synchrotron emission proves that there are relativistic electrons (with Lorentz factor, $\gamma \gg 1000$) and magnetic fields (with $\bar{B} \sim 0.1 - 1\ \mu G$) throughout the ICM.

Although X-ray emitting plasma is present in all galaxy clusters, $\sim 10\%$ of them have been found to host non-thermal plasma that can emit synchrotron radiation. There could be two possibilities for this rarity of radio emission, either sensitivity of our radio telescopes is not enough to detect diffuse radio emission in clusters as they have very low surface brightness, and/or creation and sustenance of non-thermal plasma itself is very rare. At present it is not sure which one of these options are dominant but future observations may shed more light on the topic. It is useful to stress here that the physical mechanism responsible for the presence of a non-thermal plasma in the ICM might be related to highly energetic events as suggested by their presence only in the most massive merging clusters.

4.1 Emission mechanism

As mentioned before, the main emission mechanism at radio frequency in the ICM is synchrotron radiation. The basic physics working here is that particles radiate when accelerated by a magnetic field. In case of non-relativistic particles the emission is called *cyclotron* while for relativistic particles we get *synchrotron* emission. Frequency spectrum of cyclotron radiation is quite simple and it extends till the gyration frequency. But synchrotron emission has a complex spectra and its emission

can extend to frequencies equal to many times the gyration frequency. Gyration is known as the rotation of charged particle around a magnetic field. Acceleration of the particles occur due to this gyration. The power of this radiation is given by,

$$P = \frac{4}{3}\sigma_T c\beta^2\gamma^2 U_B \tag{4.1}$$

where $\sigma_T = 8\pi r_0^2/3$ is the Thomson cross section, $\beta = v/c$ and $U_B = \bar{B}^2/8\pi$ is the magnetic energy density. Because of relativistic beaming effects the emitted radiation field appears to be concentrated in a narrow set of directions about the particle's velocity. Thus, radiation from a relativistic particle is effectively concentrated in a cone of angle θ centred in the direction of the instantaneous velocity. An observer in the plane of the orbit of the electron will actually receive pulses of very short length compared to the gyration period. The maximum radiation from the particle occurs at the frequency,

$$\nu_m = \frac{1}{4\pi}\frac{eB}{m_0}\gamma^2 \propto B\epsilon_\nu^2 \tag{4.2}$$

where m_0 is the rest mass of the electron and ϵ_ν is its spectral energy. It can be calculated from the equations that a 1-GeV electron in a magnetic field of 10^{-5} gauss emits maximum radiation at a frequency of almost 60 MHz (Kraus, 1986).

4.1.1 Synchrotron spectrum

Spectrum of a relativistic electron has a large number of closely-spaced lines giving a quasi-continuous spectrum as shown in the upper-right corner of figure 4.1. If we assume that each electron radiates independently, the total emission from a collection of such relativistic electrons will be just the sum of all individual contributions which will be a function of the energy distribution of the electrons. If we assume that all the cosmic ray particles were first produced in a single event, they should have a power law energy distribution like (Kiepenheuer, 1950),

$$N(\epsilon)d\epsilon = N_0\epsilon^{-\delta}d\epsilon \tag{4.3}$$

where $N(\epsilon)d\epsilon$ is the number of electrons per unit volume with energies between ϵ and $\epsilon + d\epsilon$. The total power radiated by them will be,

$$W \propto \int_0^\epsilon W(\epsilon)N(\epsilon)d\epsilon \tag{4.4}$$

where $W(\epsilon)$ is the power radiated per electron. The power radiated by a single electron is a function of the square of its energy. Thus,

$$W \propto \epsilon^{(3-\delta)} = \nu^{(3-\delta)/2} \tag{4.5}$$

And the variation of the total power radiated by an assemblage of electrons would be,

$$\frac{dW}{d\nu} \propto \nu^{(1-\delta)/2} \tag{4.6}$$

Finally the spectral flux density or brightness of a radio source due to such an assemblage would be,

$$F_\nu \propto \nu^{(1-\delta)/2} \text{ or } F_\nu \propto \nu^\alpha \tag{4.7}$$

We see that synchrotron spectrum of a power-law energy distribution is itself a power law. As the total emission is the sum of individual contributions, the total spectrum can be interpreted as the superposition of many contributions from the various electrons each emitting at its characteristic frequency as shown in figure 4.1. But one important thing to note in this figure is that the spectrum is a combination of two power laws, one at low frequencies and the other at high frequencies. Actually the reversal of the usual spectrum of synchrotron emission at low frequencies occur due to synchrotron self-absorption. If the intensity of synchrotron radiation within a source becomes sufficiently high, then re-absorption of the radiation by the synchrotron electron themselves becomes important. This re-absorption of radiation is termed as synchrotron self-absorption. Synchrotron self-absorption will drastically modify the spectrum of the source at low frequencies as obvious from figure 4.1.

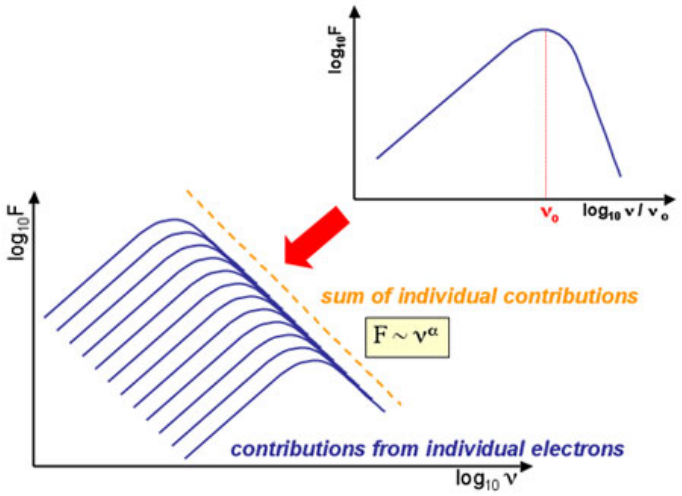

Figure 4.1: Spectra of synchrotron radiation. Each electron emits at its characteristic frequency (ν_0) as shown on the inset. Total spectra is the sum of individual contributions which gives the power law relation, $F \propto \nu^\alpha$. From *Swinburne Astronomy Online*

The cluster radio sources have quite steep spectral index, usually $\alpha \geq 1$. It means the radio emitting particles are ageing and losing their energy. Relativistic electrons may lose energy via synchrotron emission, Compton scattering with CMB photons, Coulomb interaction with other ICM particles, bremsstrahlung emission or adiabatic expansion. In the cluster radio sources most dominant of these processes are Compton scattering with CMB photons and synchrotron radiation. The higher is the energy of the particles, the faster is the energy loss of cluster radio sources. Thus some characteristic change in the shape of the spectral slope is observed. As higher energy particles have shorter energy loss time, the energy spectrum of the system is steepened. Actually, the spectrum falls off rapidly after a certain break frequency (ν^*) which in turn gradually moves to lower frequencies. Steepening in this fashion will continue until there are no more relativistic electrons to emit synchrotron radiation unless there are some re-acceleration mechanism in work. Details of their origin

and evolution will be discussed in section 4.3 although an example of steepening of the spectrum can be seen in figure 4.2.

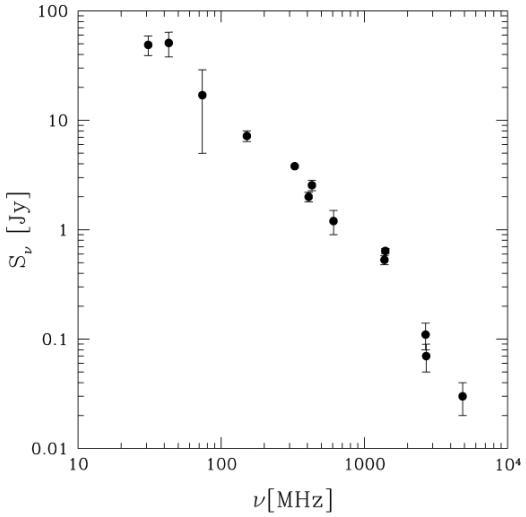

Figure 4.2: Spectrum of the radio halo in the Coma cluster named Coma C. Its clear that at $\nu > 1$ GHz, there is a steepening of the spectrum. Thus 1 GHz can be considered as the break frequency. From Ferrari et al. (2008) as adapted from Thierbach et al. (2003)

4.2 Classification of radio sources

Diffuse radio sources vary in their physical properties like size, position in the host cluster, intensity of polarised signal, morphology and association to other cluster properties. Usually these sources are divided into three broad classes: radio halo, radio relic and radio mini-halo.

4.2.1 Radio halos

The first radio source detected in the galaxy clusters was a radio halo, Coma C (figure 4.3). Radio halos have low surface brightness and are extended throughout the cluster volume. There typical size is around 1 Mpc which is more or less same as the X-ray emitting plasma distribution in the clusters. Their morphology is quite regular and their radio emission is unpolarized upto a level of few percent.

4.2.2 Radio relics

The most important properties that separates relics from haloes is that they are found in the peripheries of the clusters and their emission is usually highly polarized. While in both haloes and mini-haloes less than a few percent of the radiation is polarized, in relics this level is always more than 10% and can reach upto 30% or more. They have an elongated morphology. The prototype relic source is 1253+275 detected in the Coma cluster as shown in figure 4.4.

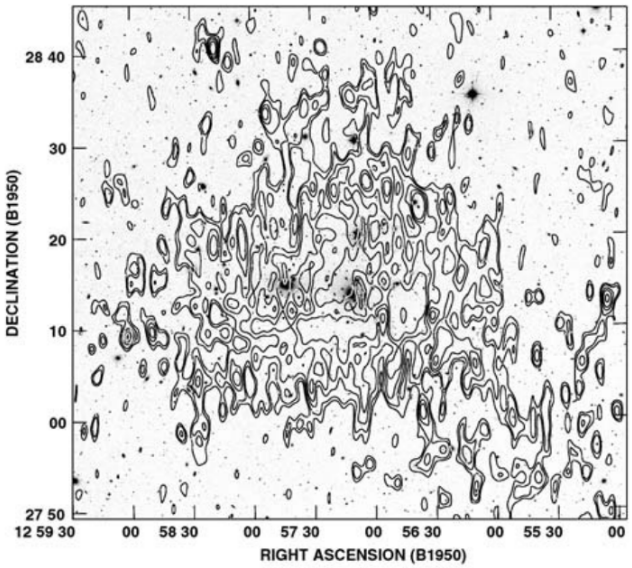

Figure 4.3: 90 cm radio contours of the radio halo in Coma cluster, Coma C, are overlaid on the DSS optical image of the cluster. Radio point sources have been subtracted. From Ferrari et al. (2008) as adapted from Feretti (2002).

Relics are found to be very different from each other. So far, at least three different kind of relics have been discovered: Giant relics, Phoenix and AGN relics. AGN relics have a size of several 10 kpc and low or medium polarisation intensity. They are located near the central cluster regions, close to the cD galaxy. They stay very close to the host AGN and shows an anti-correlation with the ICM density. In some clusters AGN relics have been found where there is a hole in the X-ray emission.

On the other hand giant and phoenix relics are strongly correlated with other ICM properties. They are mostly found in merging clusters. They do not have any parent radio galaxy nearby and their emission is more polarised than AGN relics. Typical Phoenix relics have a size of around 100 kpc while giant relics are extremely large, on the scale of Mpc. All the relics have elongated structure and in case of giant relics the major axis of this structure is usually perpendicular to the direction of the cluster radius.

4.2.3 Radio Mini-halos (MH)

As suggested by the name Mini-halos (MH) are a smaller version of giant radio haloes. This is true in terms of size, as MHs have a typical size of few 100 kpc. But there are other differences between MHs and other radio sources. As a definition we can say, MHs *are diffuse radio sources with a steep spectral index, which are found around powerful radio galaxies at the centre of cooling core clusters.* Total size of a MH is comparable to the cooling region of its host cluster. Major merger can disrupt cooling flows. Thus MHs should not be able to originate in mergers. This is the main difference between halos and MHs, halos are found in merging clusters and MHs are found in non-major merging clusters.

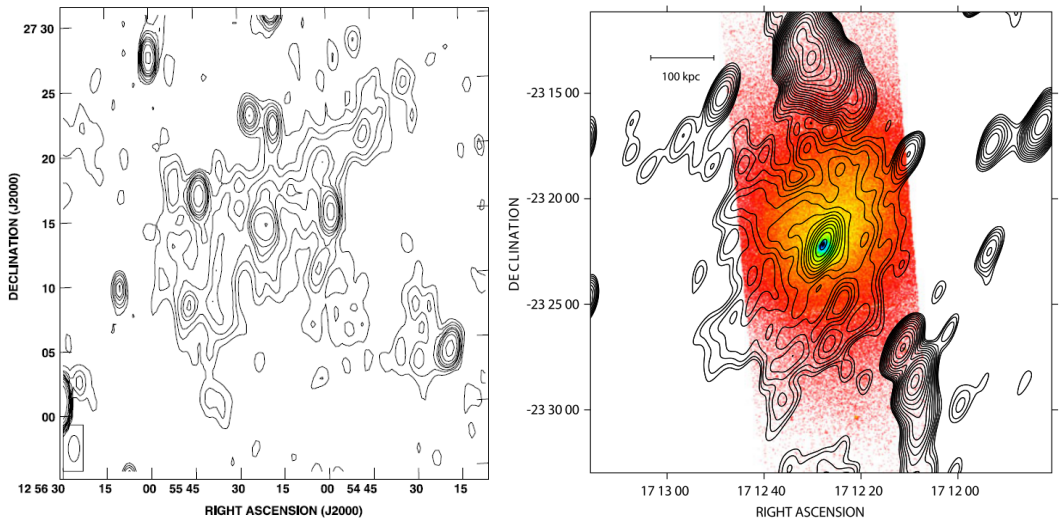

Figure 4.4: Typical examples of radio relics and mini-halos. *Left panel*: 327 MHz WSRT image of the prototype radio relic 1253+275 in the Coma cluster. From Feretti et al. (2012). *Right panel*: VLA 1.4 GHz contours of the radio MH in the Ophiuchus cluster overlaid on the *Chandra* X-ray image of the cluster. From Feretti et al. (2012) as taken from Govoni et al. (2009)

But the relation between cooling flow and MH is not yet established, at least not for all the MHs. Other mechanisms have been proposed to explain different phenomena. For example, in the central regions of the cooling flow clusters RX J1347.5-1145 (Gitti et al., 2007a) (hereafter R1347) and Abell 2142 (Giovannini & Feretti, 2000) signatures of merging activity has been observed even though they host MHs. Both clusters are dominated by two brightest cluster galaxies (BCGs). In A2142 the central cool core has been disturbed but not destroyed by a merger that is observed 1-2 Gyr after the initial core passage. Cooling flow in R1347 is one of the most massive ever detected making it the most X-ray luminous cluster. Thus we can assume that the central part of the cluster has evolved to present relaxed state over a long period of time in an undisturbed way (Gitti et al., 2007b).

However X-ray and sub-mm analyses of the cluster have shown that there is a shock heated high pressure region to the South-East of the centre corresponding to an elongation of the radio source. This suggests that the electron re-acceleration in the excess emission of this MH is related to a shock front propagating into the ICM (Ferrari et al., 2011). Indications of possible mergers have also been found in other clusters hosting MHs, such as Perseus (Furusho et al., 2000) and A2390 (Allen et al., 2001).

So far there has been only 10 confirmed detection of radio MHs (Giacintucci et al., 2011; Zuhone et al., 2012). Diffuse radio sources are actually best studied with low spatial resolution because of their very low surface brightness and large angular size. But, for MHs the condition is different. Due to the strong radio emission from the central radio loud galaxy that needs to be resolved and subtracted from the MH emission, observation of the MHs need much higher dynamic range and resolution than currently available in the surveys. Thus they are very difficult to detect. A list of galaxy clusters that host radio MHs is given in table 4.1. And as an example, the MH in the Ophiuchus cluster is shown in the right panel of figure 4.4.

Table 4.1: Clusters of galaxies hosting radio minihalos

Cluster	Redshift	Coordinates (J2000)	References
MS 1455.0+2232	0.2578	14 57 15.1 +22 20 34	Venturi et al. (2008)
RX J1720.1+2638	0.164	17 20 08.9 +26 38 06	MG08
RXC J1504.1-0248	0.2153	15 04 07.5 -02 48 16	Giacintucci et al. (2011)
RX J1347-1145	0.451	13 47 32.0 -11 45 42	Ferrari et al. (2011)
Abell 1835	0.2532	14 01 02.0 +02 51 32	Murgia et al. (2009)
Abell 2029	0.07728	15 10 56.0 +05 44 41	Murgia et al. (2009)
Perseus cluster	0.0179	03 18 36.4 +41 30 54	Sijbring (1993)
Abell 2390	0.228	21 53 34.6 +17 40 11	Bacchi et al. (2003)
Ophiuchus cluster	0.028	17 12 25.9 -23 22 33	Govoni et al. (2009)
RBS 0797	0.354	09 47 12.9 +76 23 13	Gitti et al. (2006)

4.3 Origin and evolution of cluster radio sources

As discussed before, radio emitting clusters of galaxies must have relativistic electrons and magnetics fields to give rise to the observed synchrotron radiation. The cosmic ray particles gyrate around magnetic field lines. Thus, even if the particles cannot stream out of the gravitational potential of the cluster, they can be diffused along the magnetic field lines. A fraction of relativistic electrons in these clusters that we observe at GHz frequencies have Lorentz factor between 1000 and 5000 and their diffusion time-scale is longer than the Hubble time. Steep spectrum shows that they lose energy over time, radiative lifetime of relativistic electrons being around 10^8 years. Expected diffusion velocity of the relativistic electrons is of the order of 100 km/s. With this speed cosmic rays cannot propagate over the scales of the cluster radio sources within their radiative lifetime and they therefore need to be continuously re-accelerated.

There are two kinds of models for electron re-acceleration in clusters: primary and secondary. Primary models predict that the electrons are re-accelerated to relativistic energies by shocks and turbulence induced during cluster mergers or by cooling flow or gas sloshing depending on the type of the cluster and the diffuse radio source. The secondary models propose that relativistic electrons are continuously injected by hadronic (baryons and mesons) collisions between thermal ions of the ICM and the relativistic protons. Relativistic protons have a significantly larger lifetime than electrons and are thought to be accelerated during the whole cluster history (Dolag & Ensslin, 2000). The strongest evidence in support of the primary model is that radio sources have been detected only in the merging clusters or clusters with some kind of turbulent motions. According to secondary models electron re-acceleration should be possible in all galaxy clusters, but the fact that they have been observed in very few clusters is in better agreement with the primary models. Some more comparisons between between the two models can be found in Ferrari et al. (2008).

Explaining the origin of radio MHs, which is the objective of our work, is more complicated. Like giant radio halos and relics electrons in MHs also have short ra-

diative lifetime to sustain radio emission over the whole MH region for such a long time. Thus the emission is not due to central AGN jets. On the other hand there is also no sign of recent major merger in the clusters hosting MHs. So their origin cannot be explained by the same mechanism as in radio halos and relics. Again, two kinds of explanation have been proposed for the origin of MHs. Relativistic electrons in the core of the relaxed clusters could again have a hadronic origin Pfrommer & Ensslin (2004). Or they could be a relic population of primary relativistic electrons re-accelerated by MHD turbulence induced by various cooling flows or gas sloshing.

The electron re-acceleration by cooling flow induced MHD trubulence model was quite successful in the case of Perseus (Gitti et al., 2002) and Abell 2626 (Gitti et al., 2004) clusters. Perseus surely hosts a MH and there is a candidate MH in A2626. Besides, the power of radio minihalos and cooling flows have been found to be consistent with this scenario (Gitti et al., 2007a). In some peculiar clusters like R1347 (Gitti et al. 2007a, 2007b) and A2142 (Markevitch et al., 2000), however cooling flows and trace of mergers appear to exist simultaneously. In these clusters cooling flows and mergers could have powered MH together.

Mazzotta & Giacintucci (2008, hereafter MG08) presented another possible mechanism of electron re-acceleration in the centres of cooling flow clusters. They found a very interesting correlation between cold fronts and radio MHs in two relaxed clusters, MS 1455.0+2232 (hereafter MS1455) and RX J1720.1+2638 (hereafter R1720). There are two cold fronts in both the clusters opposite to each other with respect to the center. Both of them host radio MHs that are well confined within the cold fronts, i.e. within the boundary of the central sloshing gas. Based on this evidence it was proposed that MHs in these clusters might have originated from the same gas sloshing mechanism that was proposed to explain the origin of cold fronts. In this scenario cold fronts and radio MHs has a common origin, where MHD turbulence induced by sloshing gas re-accelerates the relic population of electrons previously ejected by the central AGN. Objective of this thesis project is to analyse X-ray data of the clusters hosting MHs and check to what extent this scenario is applicable. Before presenting our results we describe the theoretical, observational and computational works that have been carried out so far related to this scenario in brief.

4.3.1 Common origin of CFs and MHs

Both MS1455 and R1720 were known to have sharp surface brightness edges on opposite sides with respect to the cluster center (Mazzotta et al., 2001a,b). The edges were suggested to be CFs but no certain conclusion could be drawn due to the limited photon statistics available at that time. The new deeper observations allowed Mazzotta & Giacintucci (2008) (MG08) to study these features in more detail and confirm their natures. To better highlight the X-ray spiral features a ratio image of both clusters were created by dividing the photon image in the [0.5,2.5] keV energy band by its radial mean values obtained from the corresponding radial profiles centred in the X-ray peak. The resulting function was smoothed using a top-hat function. The final images are shown in figure 4.5. The upper left and right panels show the smoothed ratio photon image and temperature maps of MS1455

respectively. In both the images 610 MHz radio contours of the MH obtained by analysing Giant Meterwave Radio Telescope (GMRT) data are overlaid. In the lower panels same image and map of R1720 are shown with overlaid 1.5 GHz radio contours of the MH obtained from VLA-B archival data.

In both the clusters MG08 found two cold fronts on either sides of the cluster center which are shown by blue arcs in figure 4.5. According to them, the cold fronts are roughly at a radius of 137 kpc and 40 kpc in MS1455, and 99 kpc and 155 kpc in R1720. It is evident from the images that the non-concentric cold fronts combine into a spiral pattern, like what had been predicted in Ascasibar & Markevitch (2006). And most interesting observation is that in both the clusters minihalos are apparently contained within the region delineated by the cold fronts. Also the radio structure is spatially well correlated with the X-ray spiral structure.

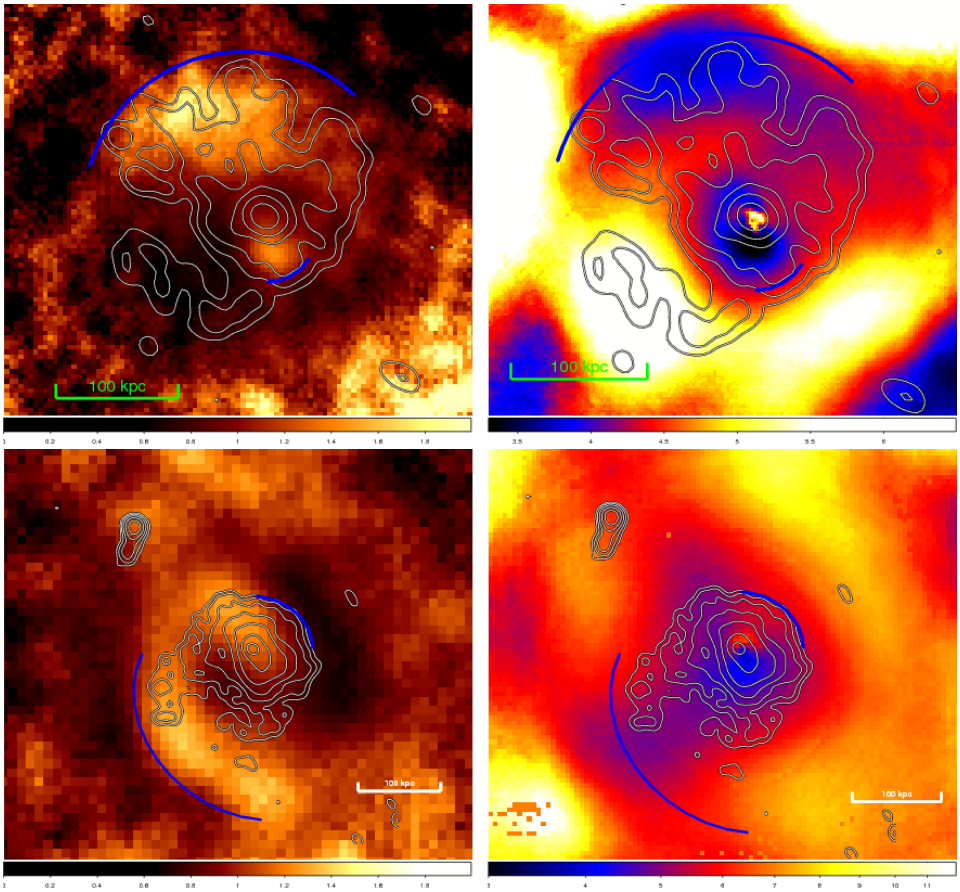

Figure 4.5: *Upper left*: ratio photon image obtained from *Chandra* (explained in the text) in the [0.5,2.5] keV energy band of MS1455, *upper right*: temperature map of the same cluster. In both the panels 610 MHz GMRT radio contours are overlaid. *Lower left*: same ratio image of R1720 using *Chandra* data, *lower right*: temperature map of the same cluster. In both the panels 1.5 GHz VLA-B radio contours are overlaid. Blue arcs indicate the cold fronts. From Mazzotta & Giacintucci (2008)

Based on these evidences MG08 suggested that the radio emitting electrons might be trapped into the same ICM gas parcels that produced CFs. The electrons might have been injected into the ICM by past AGN activity, then trapped into the ICM magnetic field and transported to the radii of the CFs by the motion of low-entropy

thermal gas induced by gas sloshing (section 3.3.3). But it was also shown in AM06 simulation that the velocity of gas sloshing is quite low, $v_{max} \sim 500\ km\ s^{-1}$. In both the MG08 clusters CFs are situated almost 150 kpc away from the center. Assuming radial transport the time needed for sloshing gas to bring relativistic electrons at the radii of the CFs is $t_{min} \geq 3 \times 10^8$ years. This time-scale is much larger than the radiative lifetime of the relativistic electrons. This simple calculation suggested that the electrons had to be re-accelerated somehow to sustain a MH. Mechanism of re-acceleration cannot be thermal shock as the motion of sloshing gas is subsonic. A plausible mechanism could be MHD turbulence. Gitti et al. (2002) already proposed that cooling flow induced MHD turbulence could re-accelerate electrons in the MHs. Also, Brunetti et al. (2004) suggested that merger induced MHD turbulence can explain the origin of giant radio halos in the clusters. It was claimed that the re-acceleration mechanism requires only a modest level of turbulence. But this time sloshing induced MHD turbulence had to be tested.

4.3.2 Simulation of sloshing-induced turbulence and MHs

Several simulations have been already carried out to test the hypothesis that, sloshing induced MHD turbulence can re-accelerate the electrons to relativistic energies to sustain MHs in the cool cores of the clusters. Using high resolution 2D simulation Fujita et al. (2004) showed that gas sloshing could automatically create turbulence in the core. The simulation done by Zuhone et al. (2012, hereafter Z12) is directly related, and complementary, to this thesis, we will describe its theoretical background and results as explained in Z12. Actually objective of Z12 was to test the hypothesis that the correlation between MHs and CFs arises from turbulence generated by sloshing motions which is closely related this thesis.

Electrons in a plasma can be accelerated by the damping of fast magneto-sonic waves on them. The magneto-sonic wave is a longitudinal wave of ions and electrons in a magnetized plasma propagating perpendicular to the stationary magnetic field. Damping, i.e. exponential decrease as a function of time, of waves can occur via energy exchange between a wave with phase velocity v_p and particles in the plasma with velocity close to v_p, which can interact strongly with the wave. Those particles having velocities slightly less than v_p will be accelerated by the wave electric field to move with the wave phase velocity, while those particles with velocities slightly greater than v_p will be decelerated, losing energy to the wave. For a quantitative understanding of such damping in the magnetized plasma of ICM, diffusion coefficient of the relativistic electrons due to the damping has to be known. Assuming phase velocity of the gas to be almost equal to the sound velocity in the medium, Z12 calculated the the momentum-diffusion coefficient of the electrons to be,

$$D_{pp} \approx 4.26 \times 10^{-11} \langle k \rangle v_t^2 p^2 \tag{4.8}$$

where k is the wave-number associated to the scale of the turbulence, v_t is the turbulent velocity and p is the momentum of the electrons. Than each relativistic electron will have an re-acceleration efficiency of,

$$\chi = \frac{4D_{pp}}{p^2} \tag{4.9}$$

and the rate of energy increase for each relativistic particle will be,

$$\left(\frac{d\gamma}{dt}\right)_{acc} = \chi\gamma \tag{4.10}$$

But one has to take into account energy loses which are mainly due to inverse-Compton scattering, synchrotron radiation (or the radiative loses) and Coulomb interactions. Combining these contributions the total change in each relativistic particles' energy can be computed by the following equation,

$$\frac{d\gamma}{dt} = \left(\frac{d\gamma}{dt}\right)_{acc} - \left(\frac{d\gamma}{dt}\right)_{coll} - \left(\frac{d\gamma}{dt}\right)_{rad} \tag{4.11}$$

where the second and third term on the right hand side are the rates of collisional and radiative energy losses. By evaluating k and v_t Z12 could calculate the diffusion coefficients of the tracer particles of their simulation. Increase in the energy of the relativistic particles could be calculated once the diffusion coefficient is known. Based on this theoretical framework Z12 performed a high resolution MHD simulation of gas sloshing in the central region of a cool-core galaxy cluster.

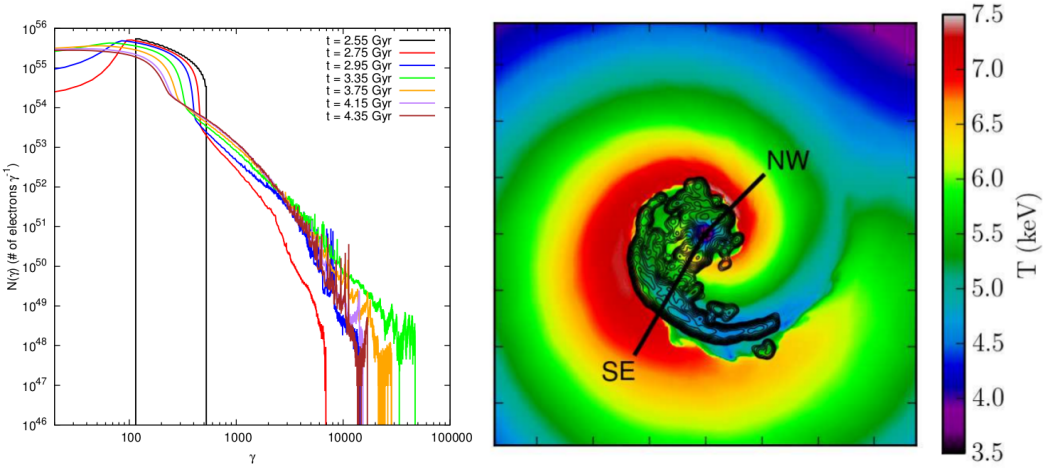

Figure 4.6: *Left panel*: Energy spectra of relativistic electrons for several epochs distinguished by different colors. It begins at $t = 2.55$ Gyr, when the electrons were first injected. *Right panel*: projected gas temperature map of the simulated cluster at the epoch $t = 3.35$ Gyr projected in the z-direction. Tick-marks indicate 100 kpc distances, thus the box is 700 kpc long at each side. 327 MHz radio contours are overlaid. From Zuhone et al. (2012)

From the results of the simulation Z12 discerned two effects of gas sloshing on the relativistic electrons that are important for the formation of minihalos. First is re-acceleration. Relativistic electrons would lose their energy and fail to produce any synchrotron radiation after a certain time unless they were re-accelerated by some mechanism. Electrons inside the sloshing region can be maintained at high enough γ for radio emission to be produced for almost 1 Gyr after the onset of sloshing. The second effect is related to the spatial distribution of relativistic electrons before and after the onset of sloshing. Gas sloshing can redistribute the relativistic electrons throughout the sloshing region. In fact, from the right panel of figure 4.6 we can see that there is a lack of radio emission beyond the cold fronts surfaces. Spatial correlation between the minihalo and spiral structure of the cold fronts is also clear

in this figure which is consistent with the observations of MG08. On the left panel of figure 4.6 energy spectrum of the relativistic particles at different epochs is shown. The electrons have been taken to be injected (through AGNs or secondary origins) at $t = 2.55$ Gyr. We can see that just 0.2 Gyr after the injection of the electrons gas sloshing has re-accelerated them upto an energy equivalent to $\gamma \sim 10^4$.

Based on the results of the simulations and consistency with the observations Z12 anticipated that sloshing could able to re-accelerate and redistribute initially relativistic seed population of electrons so that radio MH emission is produced. Additionally they mentioned that sloshing could also amplify magnetic fields within the cluster core which makes origin of MHs more probable.

Although some MHs are observed to be well confined within the region delineated by the CFs, it should be noted that exceptions to this case have also been found. The MH in R1504 was found to be extended beyond the spiral structure of the CFs (Giacintucci et al., 2011). We have examined the correlation between the MHs and the CFs in four other clusters in addition to the ones done by MG08. Details of the outcomes of our analyses will be presented in chapter 6.

Chapter 5

Data analysis

To fulfil the objectives of the thesis we have analysed archival *Chandra* X-ray data of several clusters of galaxies. We have mapped the ICM brightness and projected temperature using a multi-scale spectro-imaging software dedicated to the X-ray data analysis. Before going into the details of the analysis process we give an introduction to the *Chandra X-ray Telescope* and multi-scale analyses.

5.1 Chandra X-ray telescope

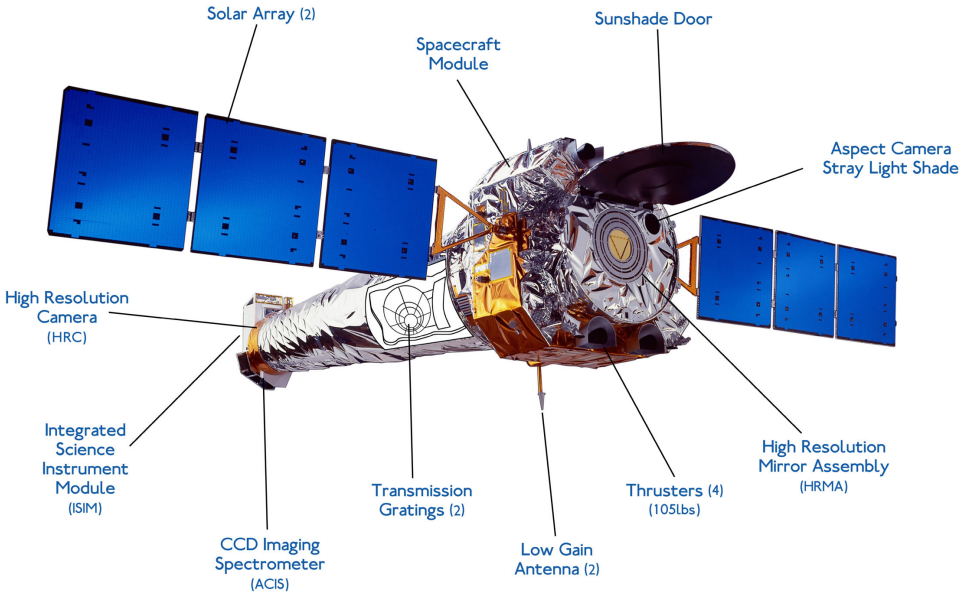

Figure 5.1: A shematic view of the *Chandra X-ray Telescope* with its different parts and instruments labeled. From http://chandra.harvard.edu

Chandra is a X-ray space telescope launched on STS-93, the 95th launch of the space shuttle, by NASA on July 23, 1999. X-ray telescopes before *Chandra* either had low spectral resolution (ROSAT) or low spatial resolution (ASCA). But *Chandra* had both good spectral and spatial resolution. The Chandra spacecraft carries a high

resolution mirror, two imaging detectors, and two sets of transmission gratings. Important *Chandra* features are: an order of magnitude improvement in spatial resolution, good sensitivity from 0.1 to 10 keV, and the capability for high spectral resolution observations over most of this range.

Chandra has an on-axis resolution of 0.5 arcsecond. There are two focal plane instruments in Chandra. One is the High Resolution Camera (HRC). It is used for high resolution imaging, fast timing measurements, and for observations requiring a combination of both. The second instrument, the Advanced CCD Imaging Spectrometer (ACIS), is an array of charged coupled devices. A two-dimensional array of these small detectors does simultaneous imaging and spectroscopy. Pictures of extended objects can be obtained along with spectral information from each element of the picture.

A Schematic view of the Chandra telescope with its main instruments is shown in fig. 5.1. The Advanced CCD Imaging Spectrometer (ACIS) can acquire high-resolution images and moderate resolution spectra at the same time. ACIS contains 10 planar, 1024×1024 pixel CCDs as shown in figure 5.2. Four of the CCDs are arranged in a 2×2 array (ACIS-I) used for imaging, and six arranged in a 1×6 array (ACIS-S) used either for imaging or as a grating readout. Two CCDs in ACIS are back-illuminated and eight are front-illuminated. But all the CCDs in ACIS-I array are front illuminated. Our observations were limited to ACIS-I as we have an improved background model for this instrument.

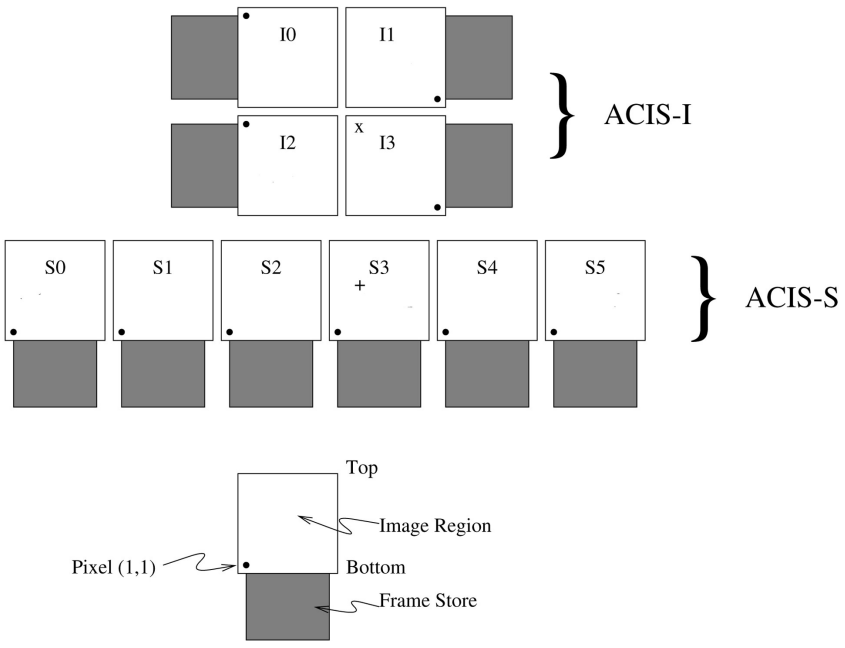

Figure 5.2: Schematic diagram of the Advanced CCD Imaging Spectrometer (ACIS) on-board Chandra X-ray observatory. In the lowest panel different parts of a CCD ship are identified. From http://chandra.harvard.edu

5.2 Multi-scale analyses

Wavelet transforms have been introduced in astronomy in the context of pattern analysis and image de-noising. The success of wavelet transforms is due to the fact in astronomy we usually observe complex hierarchical structures. Using multi-scale analyses, such as the wavelet transform, an image can be decomposed into components at different scales. Astronomical applications of the wavelet transforms include the reconstruction of galaxy iso-density distributions, weak lensing mass maps or ICM brightness maps (see e.g. Slezak et al., 1994; Starck & Pierre, 1998; Starck et al., 2006). More recently in the context of the multiresolution approximation, Bourdin et al. (2004, 2008) proposed to couple wavelet analyses and spatially resolved spectroscopy to map the ICM temperature.

5.2.1 Wavelet transform

Continuous wavelet transform

Wavelets are mathematical functions of zero average with which we can cut up data into different frequency components, and then study each component with a resolution matched to its scale. For an wavelet atom, ψ,

$$\int_{-\infty}^{+\infty} \psi(t)\ dt = 0 \tag{5.1}$$

They are dilated by a scale parameter, s and translated by the position parameter, u,

$$\psi_{u,s}(t) = \frac{1}{\sqrt{s}}\psi\left(\frac{t-u}{s}\right) \tag{5.2}$$

The wavelet transform of a function f at scale s and position u is obtained by correlating the function with a wavelet atom,

$$Wf(u,s) = \int_{-\infty}^{+\infty} f(t)\frac{1}{\sqrt{s}}\psi^*\left(\frac{t-u}{s}\right)\ dt \tag{5.3}$$

It can also be written as a frequency integration,

$$Wf(u,s) = \int_{-\infty}^{+\infty} f(t)\psi^*_{u,s}(t)dt = \frac{1}{2\pi}\int_{-\infty}^{+\infty} \hat{f}(\omega)\hat{\psi}^*_{u,s}(\omega)d\omega \tag{5.4}$$

Thus the wavelet coefficient $Wf(u,s)$ depends on $f(t)$ and $f(\omega)$ in the time-frequency region where the energy of $\psi_{u,s}$ and $\psi^*_{u,s}$ is concentrated. Here $\psi_{u,s}$ is centred at u in time with a spread proportional to s. Its Fourier transform is given by,

$$\hat{\psi}_{u,s}(\omega) = e^{-iu\omega}\sqrt{s}\hat{\psi}(\hat{s}\omega) \tag{5.5}$$

The energy of $\hat{\psi}_{u,s}$ is concentrated over a positive frequency interval centred at η/s whose size is scaled by $1/s$. A wavelet atom can be symbolically represented by a rectangle centred at $(u, \eta/s)$ in the time-frequency plane as shown in figure 5.3.

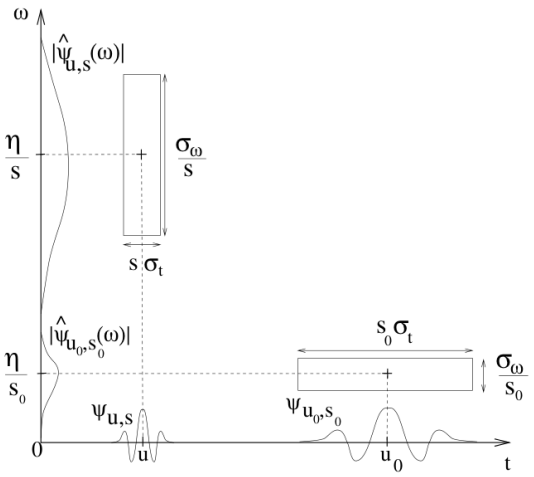

Figure 5.3: Symbolic diagram of two wavelets, $\psi_{u,s}$ and ψ_{u_0,s_0} in the time-frequency plane. When the scale s decreases time support is reduced but the frequency spread increases, shifting the covered frequency interval to higher frequencies. From Mallat (1998)

The spread of time and frequency are proportional to s and $1/s$ respectively. The height and width of the rectangles vary with the variation of s but their area remains same.

Wavelet coefficients, $Wf(u,s)$ calculate the variation of the function f in the neighbourhood of u, whose typical size is close to the scale s. Sharp transitions in the signal result in wavelet coefficients with large amplitude. Thus the local maxima of a wavelet transform can be used to detect the singularities or edges of a 1D signal, or the contours of the various features composing an image. Such analyses can be performed at a given scale or in the overall scale-space following a zooming procedure.

Discrete wavelet transform

Wavelet transforms are two-dimensional representations of a 1D signal (see equation 5.4), which amounts to some redundancy. This redundancy can be reduced by subsampling the time and scale axes of these transforms, provided that such a subsampling allows a complete representation of the signal. In other words, the signal must be reconstructible from the linear combination of a discrete family of wavelet atoms, defining a basis in its space. In particular, orthogonal bases of $L^2(R)$ can be created by dilating and translating the family,

$$\left\{\psi_{j,n}(t) = \frac{1}{\sqrt{2^j}}\psi\left(\frac{t-2^j n}{2^j}\right)\right\}_{(j,n)\in Z^2} \tag{5.6}$$

The partial sum of the wavelet coefficients obtained at scale j from projection of a signal f onto such a basis yield a detail signal,

$$\sum_{n=-\infty}^{+\infty} \langle f, \psi_{j,n}\rangle \psi_{j,n} \tag{5.7}$$

which can be interpreted as the difference between two approximations of f at resolutions 2^{j+1} and 2^{j} [1].

Multiresolution approximation: The multiresolution approximation (Mallat, 1989) actually allow us to decompose f using embedded grids of aproximations obtained at each scale from a projection onto a unique dilated and translated *scaling function*. This scaling function ϕ can be seen as the low-pass, dual function of the wavelet ψ, while the wavelet coefficients can be seen as the loss of information from approximations $j-1$ to j. In this framework, the scaling functions at scale $j-1$ and j are related to each other by a scaling equation,

$$\frac{1}{\sqrt{2}}\phi\left(\frac{t}{2}\right) = \sum_{n=-\infty}^{+\infty} h[n]\phi(t-n) \tag{5.8}$$

where

$$h[n] = \left\langle \frac{1}{\sqrt{2}}\phi\left(\frac{t}{2}\right), \phi(t-n) \right\rangle \tag{5.9}$$

is a discrete analysis filter. The multiresolution approximation thus makes it possible to decompose a discrete signal in separate frequency bands using filter banks.

Filter banks: Decomposition coefficients in a wavelet orthogonal basis may be calculated using fast algorithms that cascade discrete convolutions with h and g (two finite impulse response filters) and subsamples the output. A fast orthogonal wavelet transform decomposes successively each approximation ($P_{V_j}f$) into a coarser approximation ($P_{V_{j+1}}f$) and the wavelet coefficients carried by the local time-frequency energy densities ($P_{W_{j+1}}f$) of the function where $P_V f$ and $P_W f$ correspond to the approximation and detail analysis of f, respectively.

Both the smoothed planes (a_{j+1}) and the wavelet coefficients (d_{j+1}) are calculated from the smoothed plane a_j by applying low-pass (h) and high-pass (g) analysis filters respectively. The wavelet reconstruction is performed by applying at higher and higher resolution the low-pass and high-pass synthesis filters to the smoothed planes and the wavelet coefficients respectively. The filtered wavelets and smoothed planes are added and the right normalization leads to a new smoothed plane and so on at higher and higher resolutions. The last smoothed plane at the highest resolution constitutes the original signal.

5.2.2 Examples of wavelets

Haar wavelets: The two most relevant examples of wavelets in the context of this thesis are Haar and B-Spline wavelets. Haar wavelet is a simple piecewise constant function (as shown in figure 5.4),

$$\psi(t) = \begin{cases} 1 & if\ 0 \geq t1/2 \\ -1 & if\ 1/2 \geq t1 \\ 0 & otherwise \end{cases} \tag{5.10}$$

[1] Here 2^j is a resolution parameter corresponding to the scale parameter, j

whose dilation and translations create orthonormal basis,

$$\left\{\psi_{j,n}(t) = \frac{1}{\sqrt{2^j}}\psi\left(\frac{t-2^j n}{2^j}\right)\right\}_{(j,n)\in Z^2} \tag{5.11}$$

Any finite energy signal f can be decomposed over this basis. Each partial sum of the decomposed coefficients can be interpreted as detail variations at the scale 2^j. These layers of details are added at all scales to progressively improve the approximation of f and finally recover the function. If the function has a smooth variation, an approximation can be obtained by removing the fine scale details.

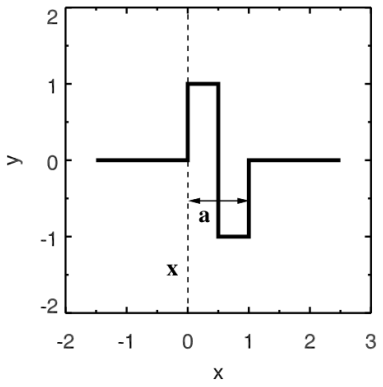

Figure 5.4: The one dimensional Haar wavelet with its characteristic parameters, scale, $a = 2^j$ and position, x. From Bourdin et al. (2004)

B-Spline function: Piecewise constant approximation of smooth functions using Haar wavelet analysis creates approximation errors. Thresholding the Haar wavelet transform generates square artefacts, especially when the signal to be analysed is regular. As signals from ICM are expected to be smooth to some extent Haar wavelets cannot produce the best results. Thus to analyse the spatial correlations of ICM temperature measurements B-Spline wavelets were used in our analysis (Bourdin & Mazzotta, 2008). Spline function is defined as a polynomial that is piecewise defined and possesses a high degree of smoothness at the places where different polynomial pieces connect. A B-Spline (short for box-spline) function of degree m is a translation of $m+1$ convolutions of a top-hat smoothing kernel with itself. It is centred at $t = 1/2$ if m is even and at $t = 0$ if m is odd. A quadratic ($m = 2$) B-Spline wavelet and the corresponding scaling function are shown in figure 5.5.

5.2.3 Undecimated Wavelet Transform (UWT)

Translation invariance is required in pattern analysis in general and astronomical image analysis in particular. Starting from the multiresolution analysis framweork, the Undecimated Wavelet Transform (UWT, Starck et al, 2007) proposes to oversample the orthogonal bases of approximations in order to preserve translation invariance. In this approach, filter banks are constructed with fast and dyadic algorithms, but the decimation step associated with the orthogonal wavelet transform is eliminated. The UWT using the filter bank (h, g) of a 1D signal c_0 leads to a set,

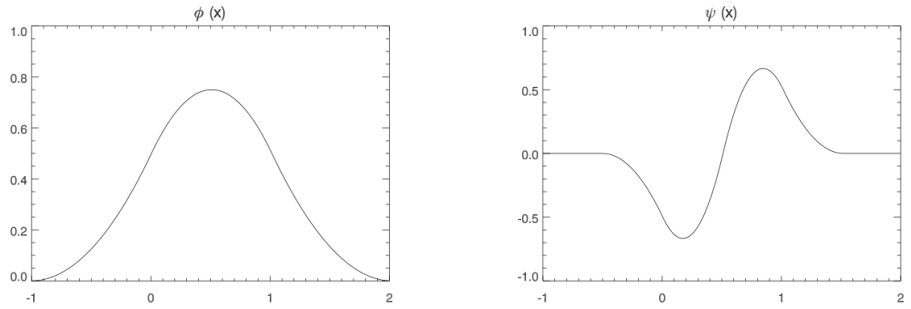

Figure 5.5: The quadratic one-dimensional B-Spline scaling function (ϕ) and dual wavelet (ψ). From Bourdin & Mazzotta (2008)

$W = \{w_1, ..., w_J, c_J\}$ where w_j are the wavelet coefficients at scale j and c_J are the coefficients at the coarsest resolution. The passage from one resolution to the next is obtained by the *à trous* algorithm,

$$c_{j+1}[l] = (\bar{h}^{(j)} * c_j)[l] \tag{5.12}$$

$$w_{j+1}[l] = (\bar{g}^{(j)} * c_j)[l] \tag{5.13}$$

where $\bar{h}$ is a time-reversed version of h, $\bar{h}[k] = h[-k]$. The reconstruction is obtained by synthesis filters $(\tilde{h}, \tilde{g})$ as,

$$c_j[l] = \frac{1}{2}\left[(\tilde{h}^{(j)} * c_{j+1})[l] + (\tilde{g}^{(j)} * w_{j+1})[l]\right] \tag{5.14}$$

As astronomical sources are usually isotropic, astronomers prefer to work with another transform named Isotropic Undecimated Wavelet Transform (IUWT). Conditions for this analysis is that, the filters must be symmetric ($\bar{h}[k] = h[k]$) and in 2D or higher dimensions h, g, ψ, ϕ must be nearly isotropic. Filters do not need to be orthogonal or bi-orthogonal for this purpose. The scaling function if a spline of order 3 and the wavelet function is obtained from the difference between scaling functions in two resolutions. Wavelet coefficients are calculated just from the difference between two resolutions,

$$w_{j+1}[k, l] = c_j[k, l] - c_{j+1}[k, l] \tag{5.15}$$

where $c_{j+1}[k, l] = (\bar{h}^{(j)}\bar{h}^{(j)}c_{j+1}[k, l] * c_j)[k, l]$. At each scale j we obtain only one set of wavelet coefficients unlike the UWT described above. The coefficients have same number of pixels as the input image. The reconstruction is obtained by simple co-addition of all wavelet scales and the final smoothed plane, (Starck et al., 2007)

$$c_0[k, l] = c_J[k, l] + \sum_{j=1}^{J} w_j[k, l] \tag{5.16}$$

5.2.4 Curvelet transform

Wavelet analysis has a limited capability and applicable for only the systems which are isotropic at all scale and locations. They cannot analyse anisotropic components

and only have a limited number of directional elements. For this purpose new multi-scale systems like ridglets and curvelets (Candes & Donoho, 1999) were introduced that have very high directional sensitivity and are highly anisotropic. A ridgelet is shown in figure 5.6. Ridgelets are constant along lines $x_1 \cos\theta + x_2 \sin\theta = \text{const}$. Transverse to these ridges it is a wavelet.

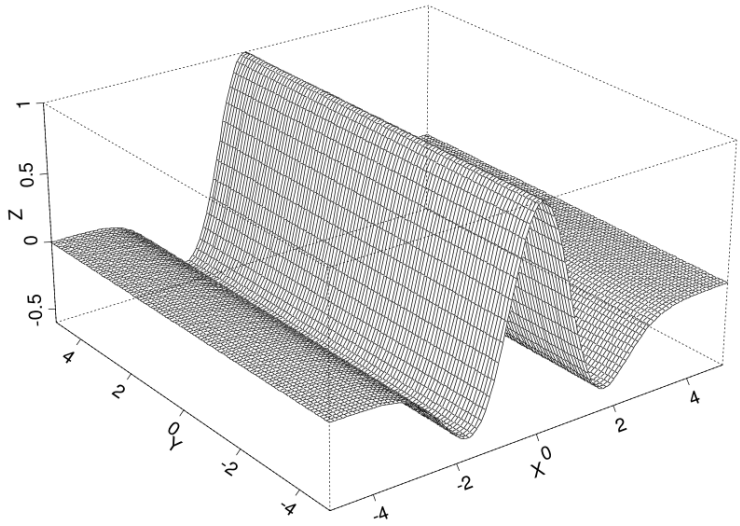

Figure 5.6: A ridgelet. From Starck et al. (2003)

In curvelet transform (CT), first, the image is decomposed into a set of wavelet bands, then each band is analysed by a local ridgelet transform (Starck et al., 2003). The discrete CT of a continuous function makes use of a dyadic sequence of scales and a bank of filters. The CT has three main steps: first the object is decomposed into wavelet subbands, then each subband is smoothly windowed into squares of an appropriate scale, and finally each square is analysed via the ridgelet transform. A flowgraph showing the main steps of curvelet and ridgelet transforms is presented in figure 5.7.

The à trous algorithm is especially well-adapted for subband decomposition in digital curvelet transform. The algorithm decomposes an $n \times n$ image I as a superposition of the form,

$$I(x,y) = c_J(x,y) + \sum_{j=1}^{J} w_j(x,y) \tag{5.17}$$

where c_J is a coarse or smoothed version of the image and w_j represents the coefficients or the details of the image at scale 2^{-j}. Thus this algorithm creates $J+1$ subband arrays of size $n \times n$. This method enjoys exact reconstruction and stability.

5.2.5 Multi-scale de-noising

Multi-scale transforms are powerful tools in signal and image denoising, as they efficiently allow us to separate in the scale-space the sparse multiresolution sum of

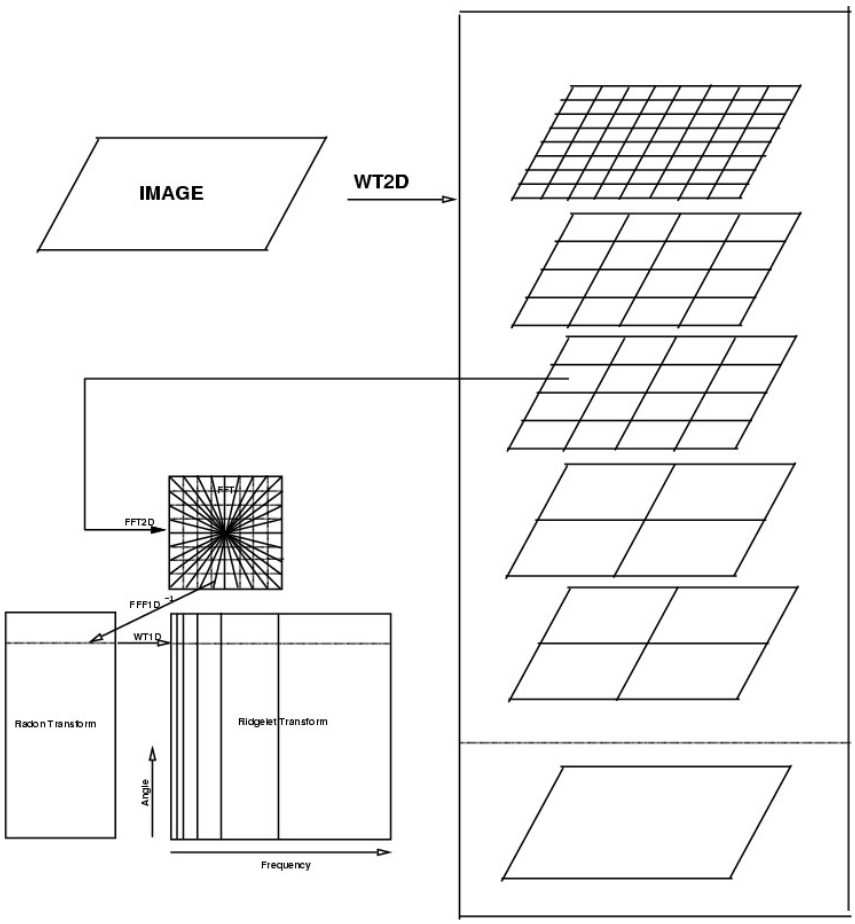

Figure 5.7: Flowgraph of curvelet transform. The image is first decomposed into wavelet subbands followed by spatial partitioning of each subband. Then local ridgelet transform is applied to each block. From Starck et al. (2003)

details present in the signal, from a nearly stationary and uniform noise contribution. This separation allows us to denoise a signal by means of a thresholding of its multi-scale transform, i.e. a partition between a set of *significant* coefficients overcoming a threshold T and a set of *non-significants* with amplitude lower than the threshold. Various thresholding strategies have been proposed so far, in particular the *hard thresholding* which consists of setting all non-significant coefficients to zero, and the *soft thresholding* which further proposes to lower the amplitude of the significant coefficients in order to reduce artefacts (see equations 10.38, 10.39 and 10.40 of Mallat, 1998).

In image denoising, the amplitude of the threshold and thus the risk of such thresholding procedures is estimated from the probability density function (PDF) of the expected noise coefficients (see e.g. Slezak et al., 1994). In the simple case of a noisy data set with additive white noise, the PDF of the noise coefficients will turn out to be Gaussian and the risk of the thresholding can be easily estimated from the variance of the coefficients (see e.g. Murtagh et al., 1995).

In X-ray data we have Poisson noise. We observe a discrete dataset of counts $\mathbf{X} = (X_i)_{i \in Z}$ where X_i is a Poisson random variable with intensity λ_i. Aim of

denoising is to estimate the underlying intensity profile, $\Lambda = (\lambda_i)_{i \in Z}$ from $\mathbf{X}$. The variance stabilizing transform (VST) is a recent attempt to approximate any discrete filtering of X as a Gaussian variable with stabilized variance (Zhang et al., 2008). Combining this transform with the filter-bank *à trous* algorithm, Starck et al. (2009), proposed the so-called Multi-Scale Variance Stabilization Transform (MSVST) to denoise Poisson noisy images. Additionally the VST can be incorporated with any of the multiscale transforms such as wavelets, UWT, IUWT, ridglets and curvelets (Zhang et al., 2008).

For the analyses of the X-ray images of our targeted clusters, VST was combined with the IUWT and curvelet transfrom. IUWT de-noising with the MS-VST is done by following three main steps: first, IUWT of the image is calculated in conjunction with its MS-VST, then significant detail coefficients are detected and in the end the final estimate is reconstructed iteratively using the knowledge of the detected coefficients. The process is illustrated in figure 5.8.

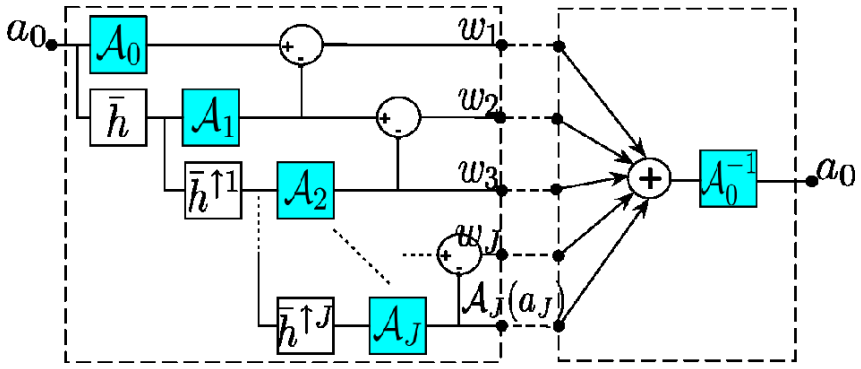

Figure 5.8: Diagram of IUWT denoising with the MSVST. The left dashed frame shows the decomposition part while the right one shows the direct inversion part. Each stage of the left frame corresponds to a scale j and an application of the equations 5.22 and 5.23. From Zhang et al. (2008).

To combine IUWT and VST first the approximation coefficients a_j at a scale j are stabilized using a VST operator. From the stabilized a_j's ($\mathcal{A}_j$) the detail coefficients are calculated in the standard way. The corresponding equations are as follows (Starck et al., 2009),

$$a_j = \bar{h}^{\uparrow j-1} * a_{j-1} \tag{5.18}$$

$$w_j = \mathcal{A}_{j-1}(a_{j-1}) - \mathcal{A}_j(a_j) \tag{5.19}$$

$$\mathcal{A}_j(a_j) = b^{(j)}\sqrt{a_j + c^{(j)}} \tag{5.20}$$

In the third and final step the image is reconstructed by inverting the MSVST,

$$a_0 = \mathcal{A}_0^{-1}\left[\mathcal{A}_J(a_J) + \sum_{j=1}^{J} w_j\right] \tag{5.21}$$

5.3 Data preparation

In each observation package of Chandra there are two directories- primary and secondary corresponding to the primary and the secondary products. The aspect solution file, that gives information on the orientation of the telescope as a function of time, is stored in the primary directory. The detected position of an event and the corresponding telescope aspect are combined for an accurate determination of the celestial position of that event.

The evt1 file is stored in the secondary directory. This level 1 event file contains all the photon impact events (the energy and the position in the detector) recorded for the observation. While many of these events have a status bit set to flag them as *bad*, none of the information has been removed. This file is filtered on good time intervals (GTI) and status bits to create the level 2 event file. Other important files here are mask and pbk files. The mask file records the valid part of the detector element used for the observation. The active portion of an element may be smaller than the default regions if an observation was performed using subarrays or custom windows. This information is used when creating response files, such as ARFs (auxiliary response file). The parameter block (pbk) file is needed in conjunction with the bias maps when creating a new bad pixel list. It is used to determine observational parameters, such as which CCDs are active.

We used the CIAO script, chandra_repro to process data of each observation stored in the primary and the secondary directories. CIAO (Chandra Interactive Analysis of Observations) is an imaging software dedicated to the Chandra X-ray data analysis. The chandra_repro program creates a new bad pixel file, a new level=2 event file, and a new level=2 Type II PHA (Pulse height amplitude) file. chandra_repro can do several steps at a time: removing the *acis detect afterglow* (due to cosmic ray) correction, detect ACIS hot pixels and process them, filter event1 file on GTI and status bits. GTI consists of start and stop times, status bit is a 32 bit number that record information on cosmic ray, bad pixel etc. For further cleaning level 2 event file, bad pixel file and the aspect offsets (a secondary product) files are given as input to the xwsm_start program of the spectro-imaging software we used.

5.3.1 Data filtering

Besides ICM emission, X-ray telescopes gather photons related to other sources such as spatially resolved X-ray emitting galaxies and cosmic X-ray background (CXB). Also, there can be transient contamination from the solar flares. CXB is very hard to separate from the ICM emission. But point sources and solar flares can be detected and removed from the observed signal using spatial and temporal wavelet analyses respectively.

In order to detect high solar flares periods and remove corresponding data sets, light curves with associated high energy events and softer events were analysed. Most prominent flares at high energy where ICM brightness is expected to be negligible are removed first, and then some additional soft flares were removed. For analysing each of the light curves a B3-spline *à trous* algorithm was used. With this analysis disruptions were detected and positive irregularities with amplitude overcoming a

2σ significance threshold were selected. Due to this cleaning effective exposure time of each observation was significantly reduced.

An object separation algorithm was used to analyse the event lists and identify the point sources. Regions in the field of view containing the point sources were masked. While analysing the signal events coming from these masked regions were isolated. For details see (Bourdin & Mazzotta, 2008) and references therein.

5.3.2 Data sampling

Each event in the event list contain the information about the energy of a photon and the corresponding position on the detector. Sky coordinates can be obtained from the detector positions. To analyse the signal with discrete wavelet transform the events are grouped and spatially sampled into sky coordinate grids. Each sample has an associated angular resolution. The events are also sampled in energy to enable spectral analysis. Thus 3D event cubes sampled in position (k, l) and energy (e) are obtained.

In order to facilitate imaging and spectral mapping, a set of similarly sampled local effective exposure and background cubes are associated to the event cubes. The sampled effective exposure, $E(k, l, e)$ at pixel $[k, l]$ is defined as the linear combination of CCD exposure times $t_{CCD}(k, l, p)$ for an individual observation, p. But there is spatial variation in the effective area of the mirror which is called the vignetting effect. Corrections due to this effect were imposed using a vignetting factor, $\Delta a(k, l, e, p)$. Other corrections to the effective exposure were due to transmission by other focal plane instruments $(tr(k, l, e, p))$ and gaps and bad pixels in the detector pixel area, $a_{CCD}(k, l, p)$. Mathematically it can be written as,

$$E(k,l,e) = \sum_{p=1}^{K} t_{CCD}(k,l,p) \times \Delta a(k,l,e,p) \times tr(k,l,e,p) \times a_{CCD}(k,l,p) \tag{5.22}$$

For creating background cubes with space and energy sampling we need to first model the background. The overall background contribution to the event spectrum is modelled as a combination of normalised spectral contributions associated with CXB (F_{CXB}), cosmic ray induced particles (F_p), i.e. the particle background, and the readout noise (F_{oot}). Particle background is a result of the interaction between the cosmic ray particles and the detector. Readout noise corresponds to a known fraction of events registered during readout periods of the detectors. The overall background can be written as,

$$n_{bck}F_{bck}(k,l,e) = E(k,l,e) \times n_{CXB}F_{CXB}(e) + n_{oot}(k,l)F_{oot}(k,l,e) + n_pF_p(e) \tag{5.23}$$

where n_{CXB}, n_{oot} and n_p are the normalisation terms and F_{CXB} is corrected for spatially variable exposure $E(k, l, e)$ as it is related to a physical observation. The CXB spectrum is modelled as the combination of a soft radiation associated with foreground galactic gas and a broad band contribution accounting for extragalactic background of unresolved galaxies. To model the galactic and extragalactic parts of

the CXB, a two temperature thermal radiation and a power law were used, respectively.

The particle background has been modelled from cumulated expositions of the telescope to the particles, during in-flight calibration phases. The readout noise was estimated by integrating and normalising the overall signal along CCD columns. Normalisation for readout noise is known a priori. But to calculate the normalisations for CXB and particle background the model needed to be fitted to an observed background spectrum. To extract this spectrum events from an external ring of the field of view were selected. The ring corresponds to a region where background emissivity is significant while uncertainties over effective area are not (Bourdin & Mazzotta, 2008).

5.4 Data analysis

5.4.1 Temperature map

A spectral mapping algorithm coupling a spectroscopic and multi-scale analysis of the X-ray signal to a wavelet mapping of the parameters was used to map the ICM temperature structure. The scheme is detailed in Bourdin et al. (2004). First, the field-of-view is sampled using square grids according to a dyadic scheme. Then, the local gas temperature, T and its fluctuation, σ_T were estimated by fitting a spectral model to the data within each pixel of the different grids. Thus a set of temperature maps is obtained with associated noise expectation maps. The temperature variations are coded as wavelet coefficients with expected noise by filtering the maps using high-pass analysis filters. Significant temperature structures are detected as wavelet coefficients with amplitude overcoming a significance threshold. Finally the gas temperature map was computed by thresholding of the wavelet transform.

The local estimation of the ICM temperature is performed by fitting a normalised spectral model to the data set associated with the pixels. The model is constructed combining the cluster emission and the overall background. It is sampled in energy and a function of temperature, metal abundance and neutral hydrogen column density. To map the global ICM temperature structure the spatial correlation of temperature measurements was analysed using wavelet coefficients. The temperature map was filtered by a B2-spline (as described in section 5.2.2) analysis filter which gives the wavelet coefficients. To reconstruct the signal the wavelet coefficients are first convolved using high-pass inverse filters associated with bi-orthogonal wavelet analysis. Addition of the thresholded coefficients gives the reconstructed map.

5.4.2 ICM brightness map

In the algorithm to map the ICM brightness structure, the local brightness $L_X(k, l)$ is first estimated from a brightness model associated with the pixel [k,l]. Then is is iteratively de-noised in the scale-space by means of MSVST + curvelet analysis. To get an idea about the joint representation of MSVST and curvelets see sections 5.2.4 and 5.2.5. The local ICM brightness is estimated by correcting the number

of events detected at the pixel from the expected background contribution and the exposure weighted instrument area.

In addition to the reconstructed brightness map, we calculated the sum of MSVST curvelet coefficients discarding the final smoothed plane for every cluster that we analysed. Basically, we followed the reconstruction formula presented in equation 5.21. The smoothed plane at scale J from this equation was discarded and certain curvelet coefficients were added. The edges were more clearly visible in the image constructed via this procedure.

5.4.3 Cold front modelling

Cold fronts can be modelled by a simple analytic function for the electron density (n_e) and 3D temperature T, both with a discontinuity at the front given as,

$$n_e = n_0 \times \begin{cases} D_n \left(r/r_j\right)^{\alpha_1}, & r < r_j \\ \left(r/r_j\right)^{\alpha_2}, & r > r_j \end{cases} \tag{5.24}$$

and,

$$T = T_0 \times \begin{cases} 1, & r < r_j \\ D_T \left[\frac{1+(r_j/r_T)^2}{1+(r/r_T)^2}\right]^c, & r > r_j \end{cases} \tag{5.25}$$

where r_j is the jump radius. Assuming spherical symmetry the 3D distribution models n_e and T can be projected to obtain the X-ray surface brightness and *spectroscopic like* (Mazzotta et al., 2004) temperature profiles according to the following equations,(Bourdin & Mazzotta, 2008)

$$\Sigma_x(r) = \frac{1}{d^2(1+z)^4} \int \epsilon_{ICM}[T(r_l)][n_p n_e](r_l) \tag{5.26}$$

$$T_x(r) = \frac{1}{\int \omega(r_l) dl} \int \omega(r_l) T(r_l) dl \tag{5.27}$$

These projected profiles can be fitted with the observations.

Chapter 6

Results

Following the procedure detailed in chapter 5, we created the X-ray images and calculated the surface brightness maps, the temperature maps and the sum of MSVST curvelet coefficients. Presence of the CFs were inferred from the maps. Then projected brightness, temperature and density profiles across the inferred edges were extracted. After determining the locations of the CFs the MH radio contours were overlaid on the temperature maps and the sum of MSVST curvelet coefficients. From the correlation of the X-ray and the radio data we examined the hypothesis that the CFs and the MHs can be produced by the same gas sloshing mechanism that has been previously proposed as a possible mechanism for the formation of CFs. Before presenting the individual results we present a list of the targeted clusters and describe the general procedure that was followed to find the CFs and correlate them with the corresponding MHs.

6.1 Observations

Table 6.1: Targeted clusters of galaxies hosting MHs

Cluster	Redshift	Chandra obs. Ids	Radio observations
MS 1455.0+2232	0.2578	4192, 7709	GMRT 610 MHz
RX J1720.1+2638	0.164	3224, 4361, 549	VLA-B 1.5 GHz
RXC J1504.1-0248	0.2153	5793	GMRT 327 MHz
RX J1347-1145	0.451	3592	GMRT 610 MHz
Abell 2029	0.07728	6101	VLA 1.4 GHz
Abell 1835	0.2532	49896, 511, 6880, 6881, 7370	VLA 1.4 GHz

So far there has been only 10 confirmed detection of radio MHs as listed in table 4.1. Seven of the clusters have been observed using the ACIS-I instrument of the *Chandra* telescope. We have the radio MH maps for six of these clusters. List of these six targeted clusters with their central coordinates, redshifts and Chandra

observation IDs are listed in table 6.1. Some information about the corresponding radio observations are also mentioned in the last column.

6.2 Cold front detection

The easiest way to detect cold fronts is to look for brightness edges in the X-ray photon image of ICM. We created the exposure and vignetting corrected and background subtracted Chandra images in the [0.5-2.5] keV energy band of all the targeted clusters (e.g. figure 6.1[a]). In almost all the clusters we could detect two edges by following the sudden color changes in the brightness color maps (e.g. change of color from blue to purple in the north-west sector of R1720 in figure 6.3[a]).

Then we analysed the photon image by MSVST+curvelet (see section 5.4.2) analysis. In the reconstructed brightness map we could see the edges more clearly (e.g. change of color from yellow to green in the south-east sector of MS1455 in figure 6.1[b]). Brightness contours logarithmically separated by a factor of $\sqrt{2}$ were overlaid on these maps. We know that, contour lines become compressed in the regions with sharp discontinuities. We could infer the positions of the CFs from these compressions.

To locate the CFs more precisely we created a smooth brightness map by summing the MSVST curvelet coefficients discarding the smoothed image at the finest resolution (see section 5.4.2). The sum of MSVST curvelet coefficients (e.g. figure 6.1[c]) showed the edges as positive coefficients represented by the black color. Two arcs were drawn in the positions of the CFs using the Inkscape graphics tool.

Brightness edges alone cannot prove the existence of CFs. There has to be a temperature jump opposite to that of brightness. So curvelet brightness contours were overlaid on the corresponding temperature maps. In this way we could correlate the sudden change of temperature with the compression of the brightness contours. By comparing the brightness and temperature maps we can clearly see the increase in temperature corresponding to a decrease in brightness across the edges (e.g. compare panels [b] and [d] of figure 6.1). These trends became more clear in the brightness and temperature profiles extracted from the regions containing the edges. The edges are indicated by arrows in the temperature maps (e.g. figure 6.1[d]).

Sectors from where the brightness and temperature profiles were extracted are overlaid on the corresponding temperature maps (e.g. figure 6.1[d]). The projected brightness and temperature profiles were fitted with a model as described in section 5.4.3. Best-fit of the projected profiles is shown by dotted lines along the observed profiles (e.g. first two rows of figure 6.2).

The 3D distribution of density and temperature in the corresponding sectors are also calculated. Projected brightness and temperature profiles overlaid on the observed ones are actually obtained from the line of sight integration of the 3D distributions as described in section 5.4.3. From 3D fits we could calculate the jump radius (r_j, distance of the CFs approximately from the X-ray peak) more clearly. The dot-dashed lines along the jumps in the profiles (e.g. figure 6.2) correspond to the approximate distance of the corresponding CFs from the X-ray peak of the cluster.

Other dot-dashed lines define the boundaries of the regions that are used for profile fitting. For some clusters the spiral structure created by the sloshing gas was also discernible (e.g. figure 6.1[c] and 6.3[c]). For others it was not so obvious because maybe they are not located in the plane of the sky.

6.3 Correlation between CFs and MHs

MG08 hypothesized that the MHs might have originated from the intergalactic gas sloshing which is one of the mechanisms responsible for the formation of CFs. If this is the case, MHs should be confined within the region delimited by the CFs and also spatially correlated with the spiral structure created by the gas sloshing. To examine this possibility we correlated radio and X-ray data of six clusters. As mentioned before, the CFs are identified by arcs in the map obtained from the sum of MSVST curvelet coefficients. We overlaid the corresponding MH radio contours on these maps to check if the MH is correlated with the CFs (e.g. figure 6.1[c]). The same radio contours were also overlaid on the temperature maps (e.g. figure 6.1[d]) and it also shows that MHs are confined within CFs.

In some clusters we observe that the MH emission is not only contained within the edges but also spatially correlated with the X-ray spiral pattern. For example, in figure 6.3(c) we see a spiral structure whose inner part runs from south to north in counter-clockwise direction (follow the violet color). The outer part runs again from north to south ending at the position of the south-east CF shown by the green arc. We also observe that the inner portion of the MH is well correlated with the spiral structure (violet color). From the corresponding temperature map (figure 6.3[d]) we see that the MH is spatially correlated with the cool central gas (blue color) that is sloshing in the potential minimum.

Our observations can also be compared with the simulations of Ascasibar & Markevitch (2006) and Zuhone et al. (2012). The simulations have showed that the locations and radii of the CFs with respect to the cluster centre can give us some idea about the merger history of the cluster. Thus something about merger history of clusters can be understood by comparing with simulations.

6.4 Results for individual clusters

Our results for all the clusters are presented in a fixed format. The panels (a) to (d) in all the odd numbered figures, i.e. 6.1, 6.3, 6.5, 6.7, 6.9 and 6.11, correspond to the soft X-ray image, X-ray surface brightness map of the ICM obtained by curvelet analysis, decomposed brightness map obtained by summing MSVST curvelet coefficients and the temperature map obtained by B2-spline wavelet analysis, respectively if not mentioned otherwise. In panel (b) brightness contours are overlaid on the corresponding brightness map. In panel (c) radio contours are overlaid on the sum of MSVST curvelet coefficients. Finally in panel (d) radio contours and the sectors from where the profiles were extracted are overlaid on the temperature map. Cold fronts are detected examining the figures in these panels following the procedure detailed in the beginning of this chapter.

Table 6.2: Parameters of the Cold Fronts in the targeted clusters

Galaxy clusters	Cold fronts	Jump radii (r_j) (kpc)	Position angles (degree)
MS 1455.0+2232	North-East	148.4 ± 1.4	45-160
	South-West	$54.287^{+5.76}_{-1.15}$	270-330
RX J1720.1+2638	North-West	$70.6^{+1.7}_{-7.9}$	2-80
	South-East	$192.4^{+1.3}_{-0.8}$	180-280
RXC J1504.1-0248	North-West	$59.2^{+5.3}_{-0.11}$	2-80
	South-East	46.8^{+8}_{-1}	180-280
RX J1347-1145	Eastern	$90.8^{+2.5}_{-1}$	300-60
	Western	41.9 ± 2.2	100-190
Abell 2029	North-West	$111.5^{+0.5}_{-1.4}$	20-80
	Eastern	$86^{+1.8}_{-0.25}$	120-220
Abell 1835	North-East	55.1 ± 0.9	95-185
	North-West	51.7 ± 0.8	30-90

In the even numbered figures, i.e. 6.2, 6.4, 6.6, 6.8, 6.10 and 6.12, we present the profiles extracted from the regions shown in the corresponding temperature maps of the clusters. We show four profiles for each CF: the observed projected X-ray surface brightness profile and temperature profile, and the projected density and temperature profiles obtained from the 3D density and temperature models. Thus for every cluster we present eight profiles corresponding to the two CFs. Parameters of the CFs in each cluster are presented in table 6.2. A short description of the maps and profiles for the individual clusters are presented in the following sections.

6.4.1 MS 1455.0+2232

We analysed two Chandra observations of MS1455 with a total exposure time of 102 ks. After cleaning (as described in section 5.3) the effective exposure time became 88.4 ks. Results of our analysis are presented in figures 6.1 and 6.2.

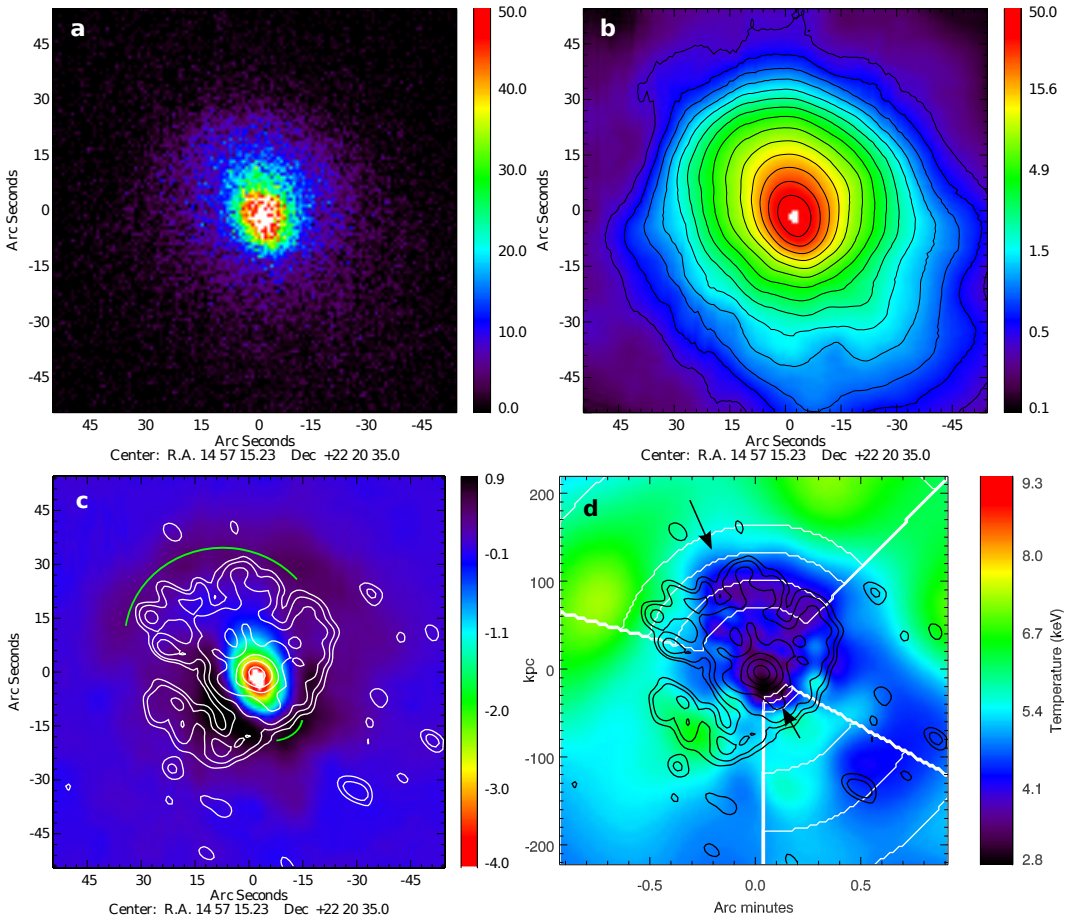

Figure 6.1: Chandra X-ray image in the [0.5,2.5] keV energy band (a), brightness map obtained by curvelet analysis with overlaid brightness contours (b), sum of MSVST curvelet coefficients with radio contours overlaid (c) and temperature map obtained by B2-spline wavelet analysis with radio contours overlaid (d) of MS1455. 610 MHz GMRT radio contours are logarithmically separated by a factor of 2 and start from a 3σ noise level of 90 μJy/beam. The beam size is $11.3'' \times 10.4''$. X-ray brightness contours are logarithmically separated by a factor of $\sqrt{2}$ and has a resolution of $0.86''$. In panel (d) white sector annuli correspond to the sectors from where brightness and temperature profiles (as shown in figure 6.2) are extracted. The arcs and arrows in panels (c) and (d) show the positions of the CFs.

We detected two CFs in this cluster, one $\sim$ 148 kpc to the north-east of the centre and the other $\sim$ 54 kpc to the south-west of the centre. Parameters of the CFs are presented in table 6.2. In figure 6.1(a) the NE edge is discernible between purple and black colors while the SW one between green and purple. We see a compression of the brightness contours (b) in the same regions and sum of MSVST coefficients shows the edges clearly in black colors where the CFs are also marked by two arcs. From panels (c) and (d) we see that the MH emission is confined within the region delimited by the CFs and also spatially correlated with the X-ray spiral structure

created by the gas sloshing.

Our observation agrees with that of MG08 (compare with the upper left panel of figure 4.5). It also matches with the simulation of AM06 (compare with the last panel of figure 3.9). Recalling the discussion of section 3.3.5 we can say that he CFs in MS1455 are in a stage that might be represented by the panel at $t = 2.1$ Gyr of figure 19 in AM06. But in case of MS1455 the pericentre passage of the sub-cluster might have occurred from the south-west direction.

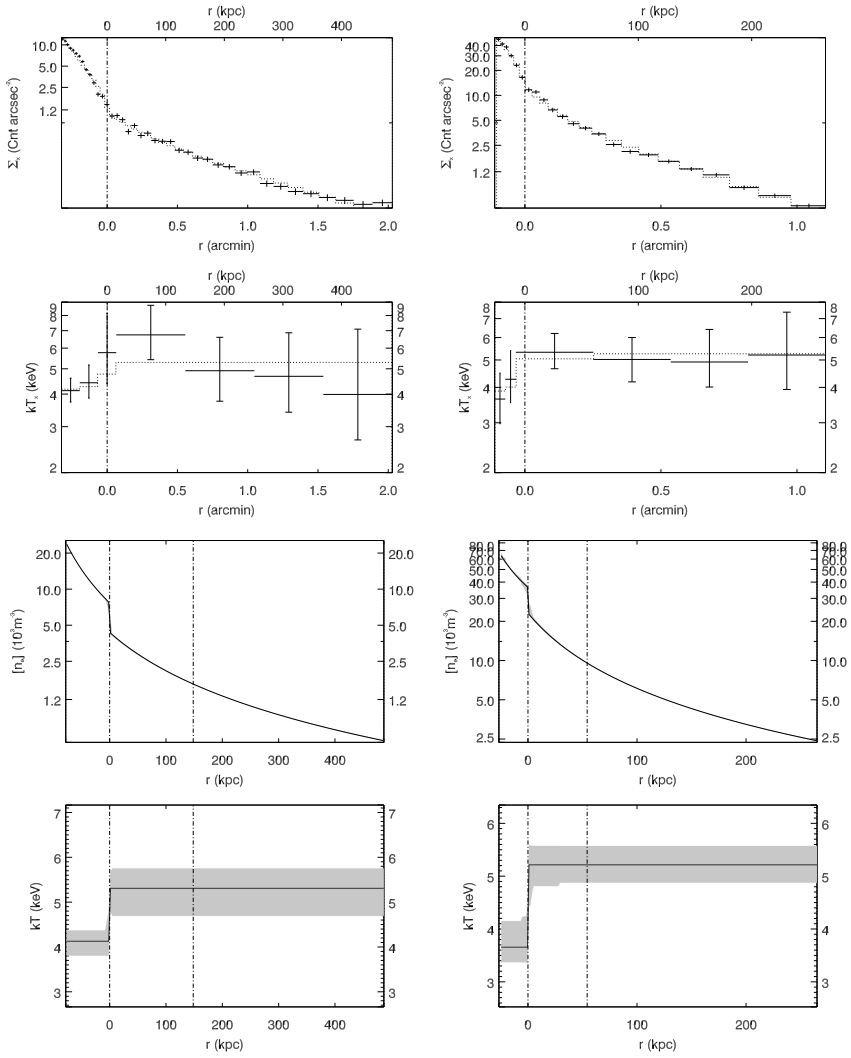

Figure 6.2: *From top to bottom*: Projected gas brightness (Σ_x), spectroscopic temperature (kT_x), and derived density (n_e) and temperature (kT) profiles corresponding to the sectors shown in figure 6.1(d). Profiles in the left and the right columns correspond to the North-East and South-West cold fronts of MS1455, respectively. Dashed lines along the brightness and temperature profiles correspond to fits of the projected functions. The vertical dot-dashed lines along the jumps indicate the positions of the CFs. Front modelling and fitting regions are bounded by the dot-dashed lines on the right.

6.4.2 RX J1720.1+2638

We analyzed three Chandra observations of R1720 (table 6.1) with a total exposure time of 49.7 ks. After cleaning the effective exposure became 33.3 ks. Our results are presented in figures 6.3 and 6.4. Examining the maps in figure 6.3 we detected two CFs, the north-west one at a radius of $r_j \sim 70$ kpc and the south-east one at a radius of $r_j \sim 192$ kpc. The parameters of these CFs obtained from the best-fit density and temperature models (figure 6.4) are given in table 6.2. The CFs are also indicated by arcs in figure 6.3(c) and by arrows in figure 6.3(d). From the panels (c) and (d) of figure 6.3 we can see that the MH is confined within the CFs and also spatially correlated with the spiral in-flow of the sloshing gas. This also agrees with the observations of MG08.

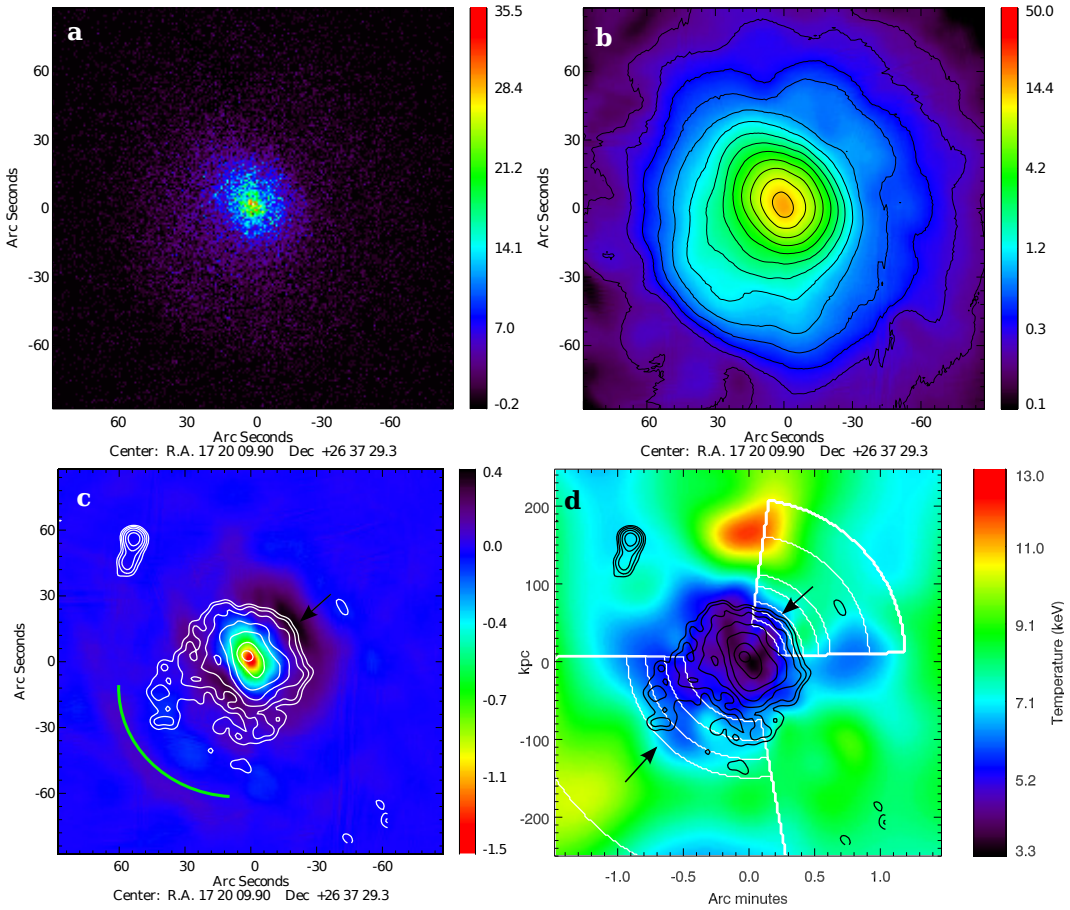

Figure 6.3: Chandra X-ray image in the [0.5,2.5] keV energy band (a), brightness map obtained by curvelet analysis with overlaid brightness contours (b), sum of MSVST curvelet coefficients with radio contours overlaid (c) and temperature map obtained by B2-spline wavelet analysis with radio contours overlaid (d) of R1720. 1.5 GHz VLA radio contours are logarithmically separated by a factor of 2 and start from a 3σ noise level of 0.1 mJy/beam. The beam size is $5.7'' \times 4.8''$. X-ray brightness contours are logarithmically separated by a factor of $\sqrt{2}$ and has a resolution of $0.86''$. In panel (d) white sector annuli correspond to the sectors from where brightness and temperature profiles (as shown in figure 6.4) are extracted. The arcs and arrows in panels (c) and (d) show the positions of the CFs.

The gas sloshing scenario in this cluster can be explained by comparing it with the last panel of figure 3.8. In the simulation of AM06, a gasless sub-cluster had to

approach the main cluster from the north-west side to give rise to the characteristic CFs. The cool dense gas in the simulation spiral-in towards counter-clockwise direction as opposed to the clockwise spiralling-in flow of gas in R1720. Thus we can assume that a sub-cluster approaching from the north-east direction gave rise to such cold fronts in R1720. We can discern the spiral flow to some extent which means the minor merger must have occurred on the plane of the sky or at a very small angle to the plane of the sky. By analysing the SE CF, Mazzotta et al. (2001b) found that the angle between the merger plane and the plane of the sky must be less than 35° for us to see the CFs in this way.

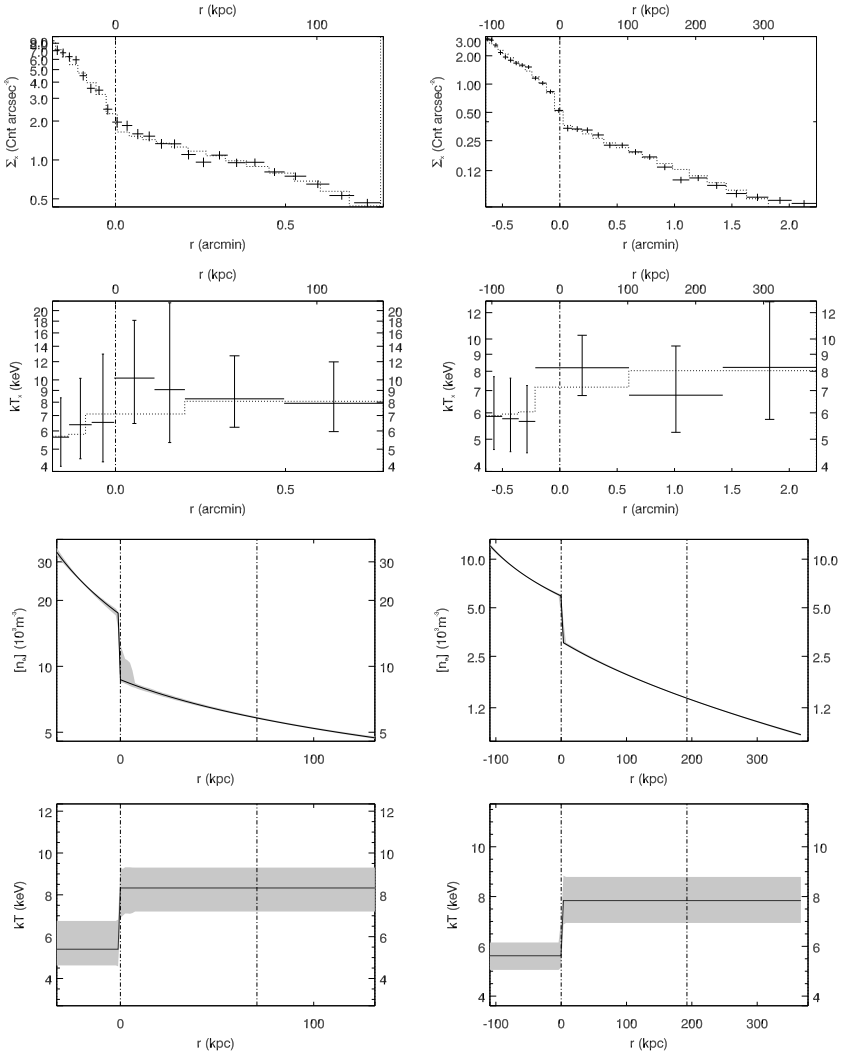

Figure 6.4: *From top to bottom*: Projected gas brightness (Σ_x), spectroscopic temperature (kT_x), and derived density (n_e) and temperature (kT) profiles corresponding to the sectors shown in figure 6.3(d). Profiles in the left and the right columns correspond to the North-East and South-West cold fronts of R1720, respectively. Dashed lines along the brightness and temperature profiles correspond to fits of the projected functions. The vertical dot-dashed lines indicate the positions of the CFs. Front modelling and fitting regions are bounded by the dot-dashed lines on the right.

6.4.3 RXC J1504.1-0248

We analysed one Chandra observation of R1504 with an exposure time of 40 ks which after cleaning became 31.3 ks. Our results are presented in figures 6.5 and 6.6. We have found two CFs in this cluster, the north-west one at radius of $r_j \sim 59$ kpc and the south-east one at $r_j \sim 46$ kpc.

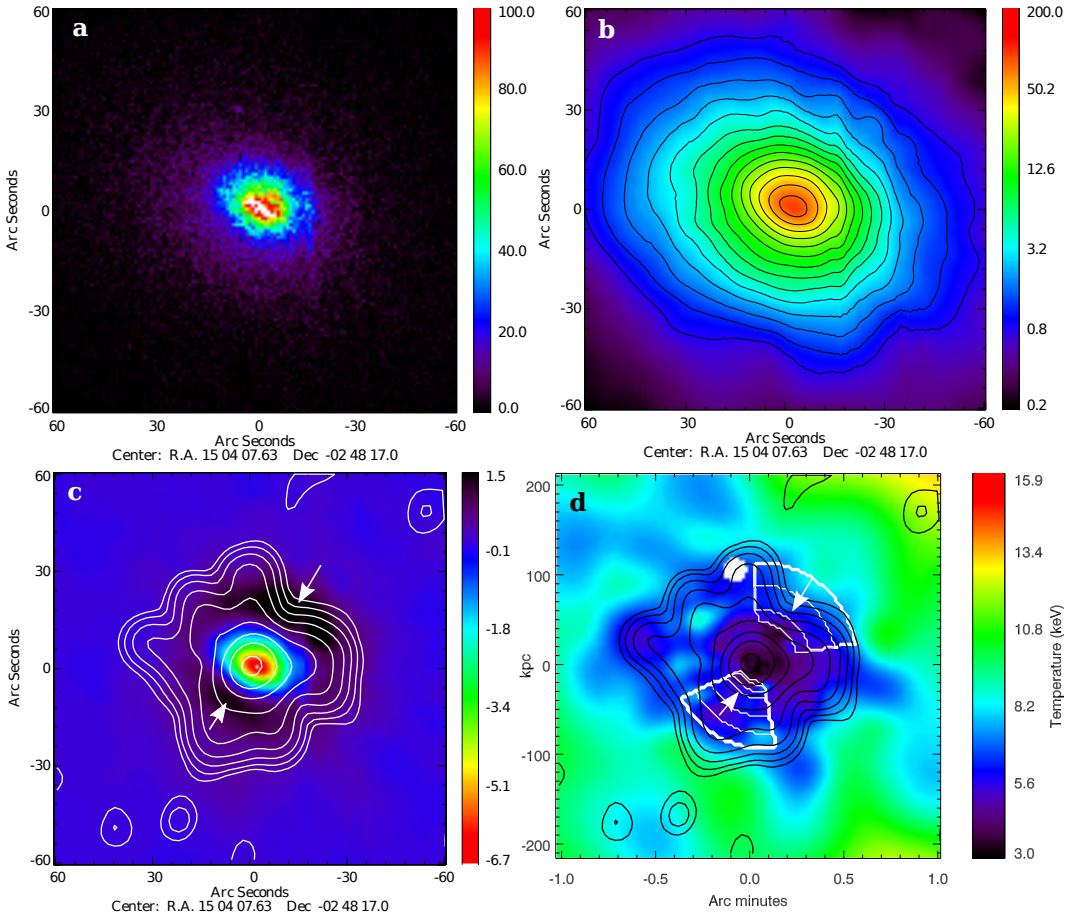

Figure 6.5: Chandra X-ray image in the [0.5,2.5] keV energy band (a), brightness map obtained by curvelet analysis with overlaid brightness contours (b), sum of MSVST curvelet coefficients with radio contours overlaid (c) and temperature map obtained by B2-spline wavelet analysis with radio contours overlaid (d) of R1504. 330 MHz GMRT radio contours are logarithmically separated by a factor of 2 and start from a 3σ noise level of 0.3 mJy/beam. The beam size is $11.3'' \times 10.4''$. X-ray brightness contours are logarithmically separated by a factor of $\sqrt{2}$ and has a resolution of $0.96''$. In panel (d) white sector annuli correspond to the sectors from where brightness and temperature profiles (as shown in figure 6.6) are extracted. The arrows show the locations of the CFs.

Giacintucci et al. (2011, hereafter SG11) discovered a radio minihalo at the centre of this cluster using archival *GMRT* and 1.46 GHz *VLA* observations. At the same time by inspecting *Chandra* image they speculated the existence of at least two subtle brightness edges in the cool core. To better illustrate the edges they fit a symmetric β-model to *Chandra* image and subtracted it from the real image. By comparing it to the temperature map they showed that these edges were cold fronts. We show the positions of the CFs by two arcs in figure 6.5(c). The MH radio contours are

overlaid on both (c) and (d) panels. We can estimate that the MH is extended upto a radius of almost 140 kpc (Giacintucci et al., 2011). Interestingly, cooling radius of the cluster is also extended to almost 140 kpc. Our observation agrees with that of SG11 (compare figure 6.5[c] with figure 3 of SG11).

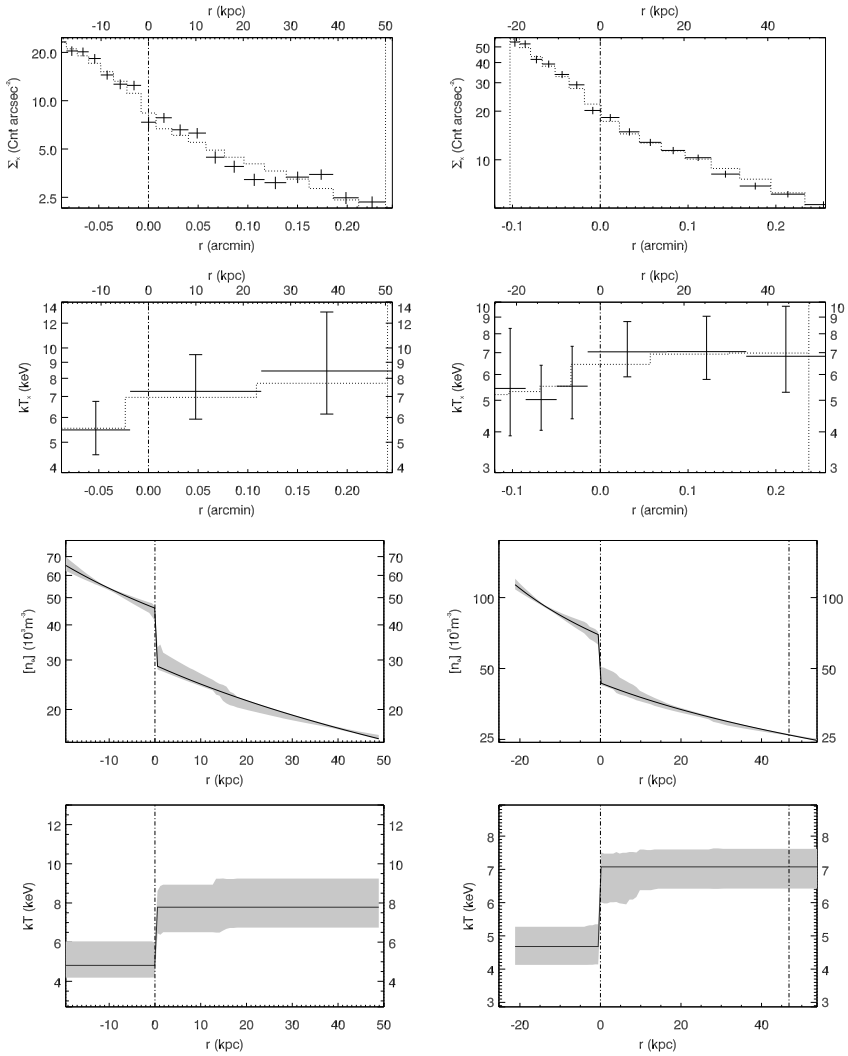

Figure 6.6: *From top to bottom*: Projected gas brightness (Σ_x), spectroscopic temperature (kT_x), and derived density (n_e) and temperature (kT) profiles corresponding to the sectors shown in figure 6.1(d). Profiles in the left and the right columns correspond to the North-East and South-West cold fronts of R1504, respectively. Dashed lines along the brightness and temperature profiles correspond to fits of the projected functions. The vertical dot-dashed lines indicate the positions of the CFs. Front modelling and fitting regions are bounded by the dot-dashed lines on the far right.

According to figure 6.5(c) the NW CF is very close to the NW boundary of the MH, but the SE CF is located in the inner part of the MH. This GMRT data has a comparatively low resolution ($11.3'' \times 10.4''$). In the right panel (inset) of figure 1 in SG11, higher resolution ($4'' \times 4''$) radio contours of this MH obtained by VLA 1.46 GHz pointed observation are shown. Here the radius of the SE boundary of the MH is not more than 50 kpc. In that case the SE CF at $r \sim 46$ kpc coincides with the SE boundary of the MH. However, if the radio observations have a higher resolution,

they could also have a lower sensitivity. On the other hand short baselines are needed to image diffuse sources in their whole extent. The MH might seem more compact in the VLA image because of lower sensitivity and lack of short baselines. Deeper observations with proper u-v coverage are needed to associate the MH with the CFs in R1504 more precisely.

6.4.4 RX J1347-1145

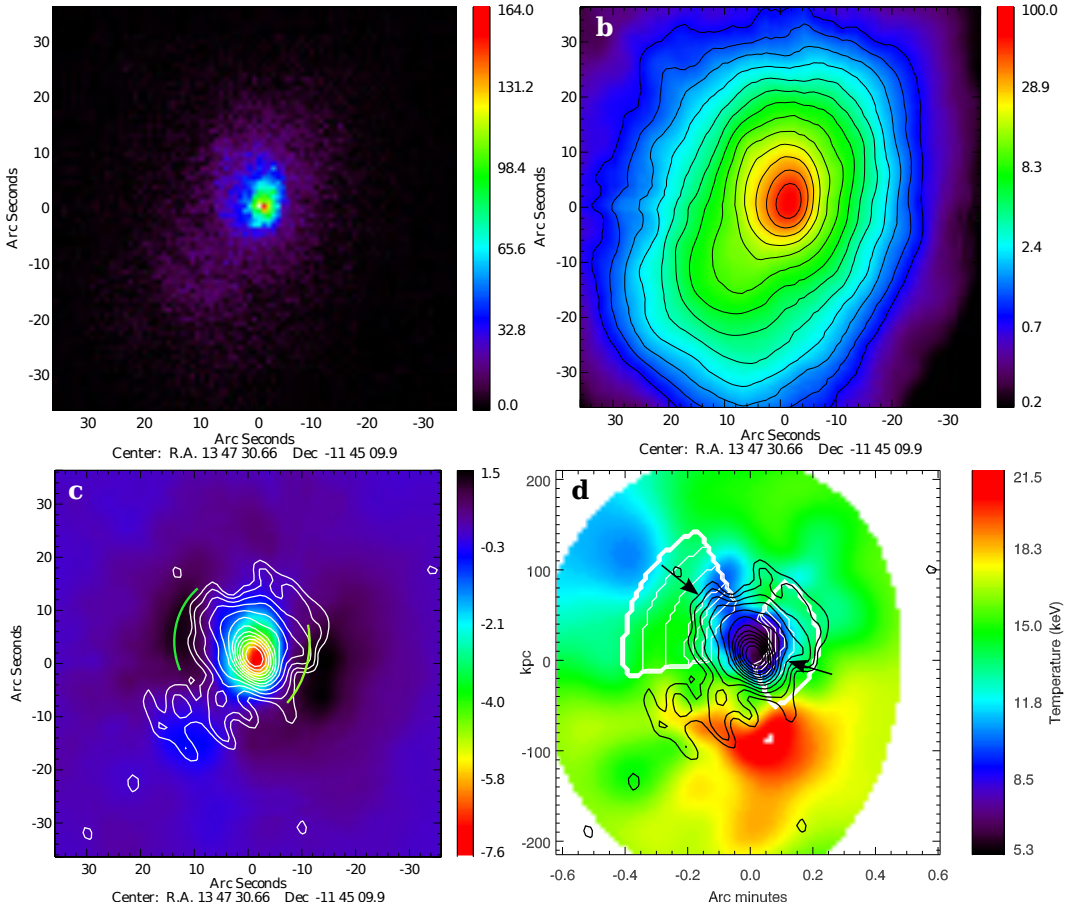

Figure 6.7: Chandra X-ray image in the [0.5,2.5] keV energy band (a), brightness map obtained by curvelet analysis with overlaid brightness contours (b), sum of MSVST curvelet coefficients with radio contours overlaid (c) and temperature map obtained by B2-spline wavelet analysis with radio contours overlaid (d) of R1347. 610 MHz GMRT radio contours are logarithmically separated by a factor of 2 and start from a 5σ intensity level. The beam size is $4.8'' \times 3.5''$. X-ray brightness contours are logarithmically separated by a factor of $\sqrt{2}$ and has a resolution of $0.86''$. In panel (d) white sector annuli correspond to the sectors from where brightness and temperature profiles (as shown in figure 6.8) are extracted. The arrows show the locations of the CFs.

Johnson et al. (2012, hereafter RJ11) found two CFs in R1347, the western one at a distance of $\sim 30\ h^{-1}$ kpc and the eastern one at a distance of $\sim 60\ h^{-1}$ kpc from the X-ray peak. We analysed one Chandra observation of this cluster with an exposure time of 57.7 ks which became 51.1 ks after cleaning. Our results are presented in figures 6.7 and 6.8. We also found two CFs: the western one at a radius of $r_j \sim 42$ kpc and the eastern one at $r_j \sim 90$ kpc.

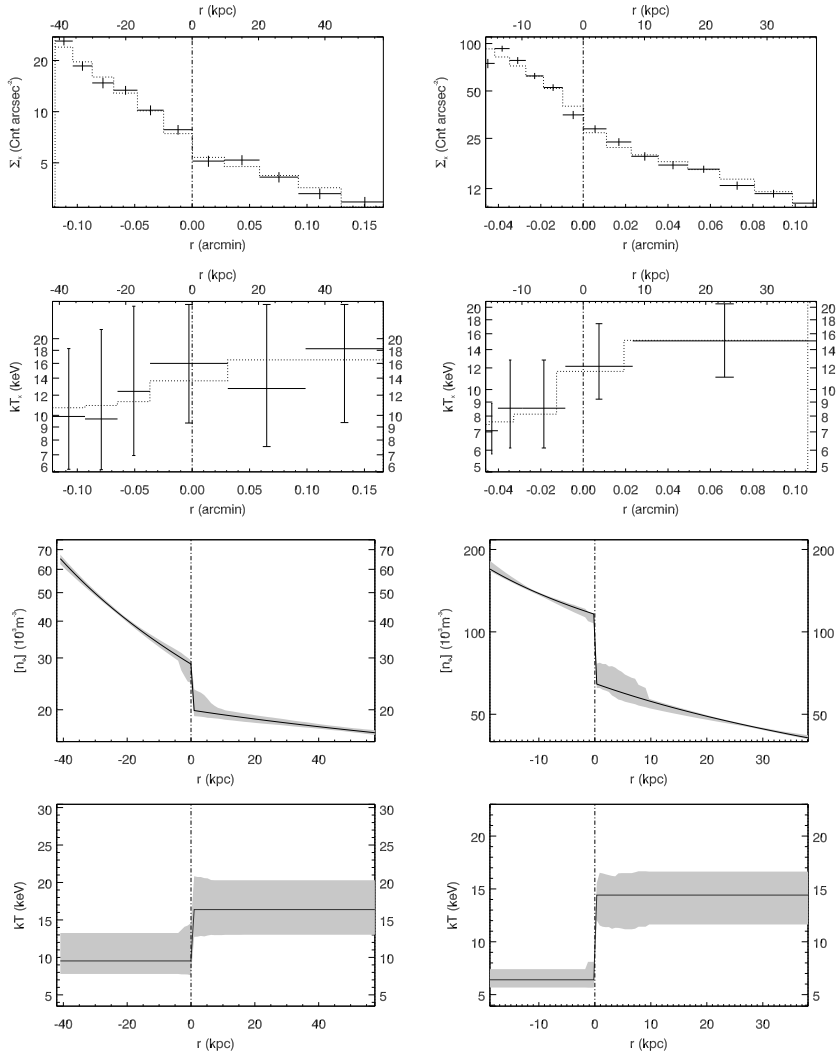

Figure 6.8: *From top to bottom*: Projected gas brightness (Σ_x), spectroscopic temperature (kT_x), and derived density (n_e) and temperature (kT) profiles corresponding to the sectors shown in figure 6.7(d). Profiles in the left and the right columns correspond to the Eastern and Western cold fronts of R1347, respectively. Dashed lines along the brightness and temperature profiles correspond to fits of the projected functions. The vertical dot-dashed lines indicate the positions of the CFs.

The locations of the CFs are marked by two arcs in panel (c) and by two arrows in panel (d). RJ11 found a second cD galaxy ~ 160 kpc south-east of the X-ray peak. The location of the cD2 is coincident with that of the subcluster that set off the gas sloshing. Considering the distance of the CFs and the separation of the subcluster from the X-ray peak they hypothesized that it might be the *second crossing* of the subcluster. We find that the radio emission is confined within the CFs (from panels [c] and [d] of figure 6.7). The north-west portion of the MH is spatially correlated with the X-ray emitting gas, but it is elongated to the south-east direction. This SE excess was found to be the consequence of a shock front propagating into the ICM (Ferrari et al., 2011).

6.4.5 Abell 2029

We analysed one Chandra observation of A2029 with an exposure time of 10 ks. We created the brightness and temperature maps by analysing the data prepared by Iacopo Bartalucci. Our results are presented in figures 6.9 and 6.10. We found two CFs in this cluster one $\sim$ 110 kpc to the North-West and the other $\sim$ 86 kpc to the East with respect to the centre.

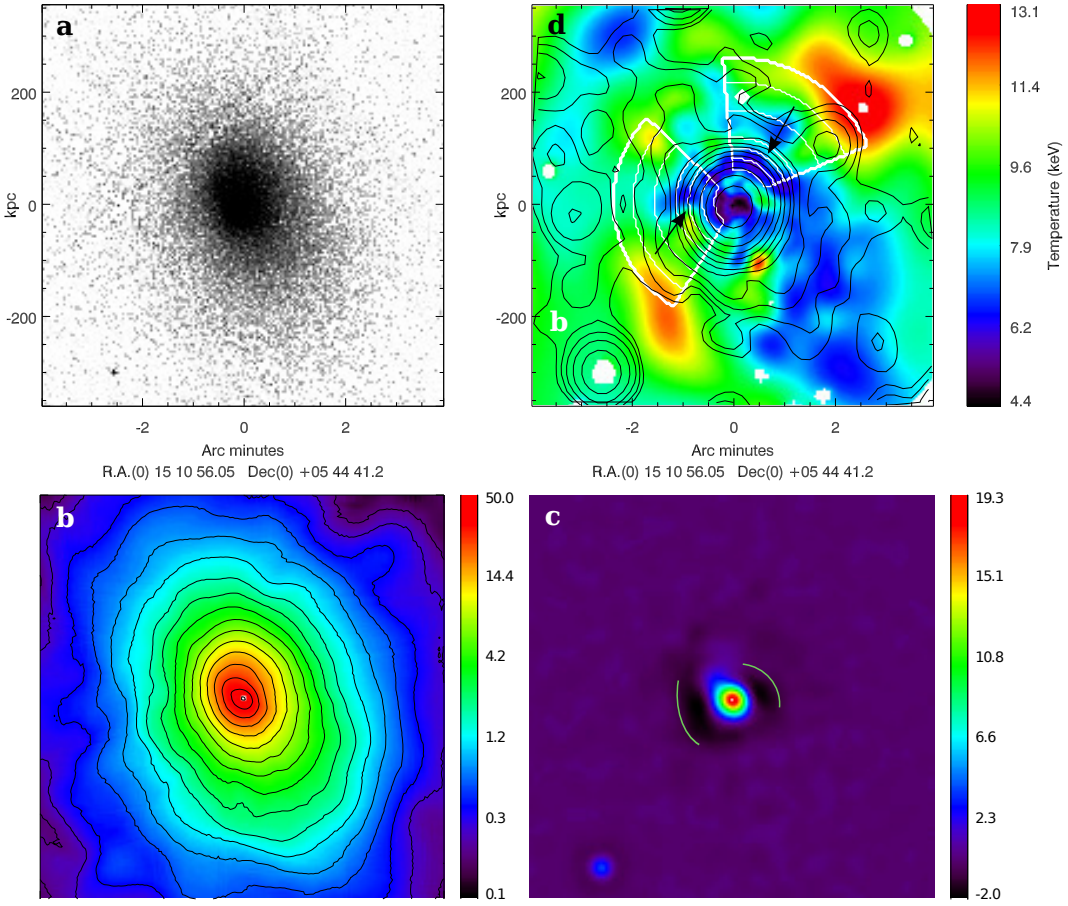

Figure 6.9: Chandra X-ray image in the [0.5,2.5] keV energy band (a), brightness map obtained by curvelet analysis with overlaid brightness contours (b), unsharp image (c) and temperature map obtained by B2-spline wavelet analysis with radio contours overlaid (d) of A2029. 1.4 GHz VLA-D radio contours are logarithmically separated by a factor of 2 and start from an intensity level of 0.12 mJy/beam. The beam size is $49.8'' \times 45.5''$. X-ray brightness contours are logarithmically separated by a factor of $\sqrt{2}$ and has a resolution of $2.78''$. In panel (d) white sector annuli correspond to the sectors from where brightness and temperature profiles (as shown in figure 6.10) are extracted. The arrows show the locations of the CFs.

We can guess the locations of the CFs by looking at the compressions in the brightness contours. The spiral structure can be inferred very clearly from the temperature map (cool gas represented by blue color in figure 6.9[d]). The CFs can be identified clearly in the unsharp brightness map shown in panel (c) of figure 6.9. This image was created by subtracting two Gaussian smoothed images at different scales, with FWHM 8 and 16 pixels, respectively. Profiles corresponding to the sectors around the CFs are presented in figure 6.10. Clarke et al. (2004) also detected a spiral excess (see figure 9 and 10 of their paper) in this cluster which is in agreement with

our observation.

The radio MH emission is much more extended than the region delimited by the CFs in this cluster (see figure 6.9[d]). The regular radio contours in the inner part are associated with the central unresolved point source. Figure 6.9(d) shows that the scale of the MH is much larger than the radii of the CFs. The southern part of the MH spatially correlates with the spiral structure.

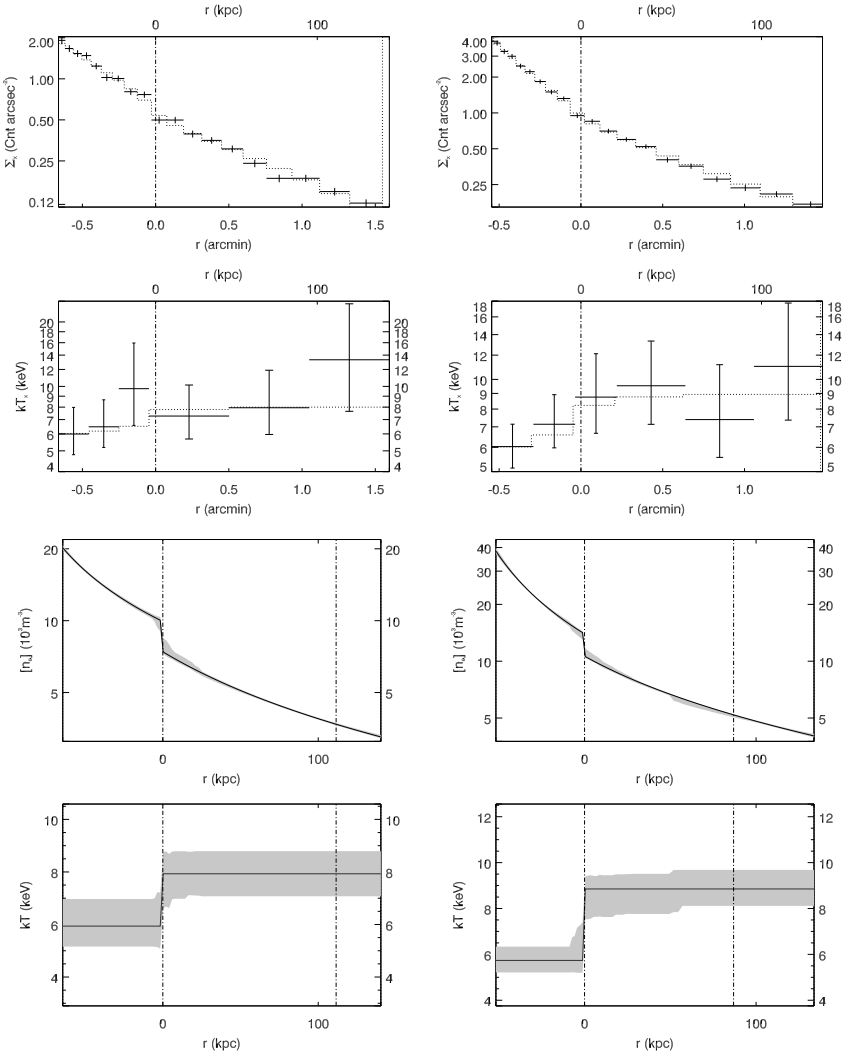

Figure 6.10: *From top to bottom*: Projected gas brightness (Σ_x), spectroscopic temperature (kT_x), and derived density (n_e) and temperature (kT) profiles corresponding to the sectors shown in figure 6.9(d). Profiles in the left and the right columns correspond to the North-West and Eastern cold fronts of A2029, respectively. Dashed lines along the brightness and temperature profiles correspond to fits of the projected functions. The vertical dot-dashed lines indicate the positions of the CFs. Front modelling and fitting regions are bounded by the dot-dashed lines on the right.

6.4.6 Abell 1835

We analysed three Chandra observations of A1835 with a total exposure time of 193.7 ks which became 149.2 ks after cleaning. The results are presented in figure

6.11 and 6.12. From panels (a), (b) and (c) of figure 6.11 we can see that there is an extended ring all the way from the north-west to the north-east of the centre. In panel (c) this ring can be seen in black color.

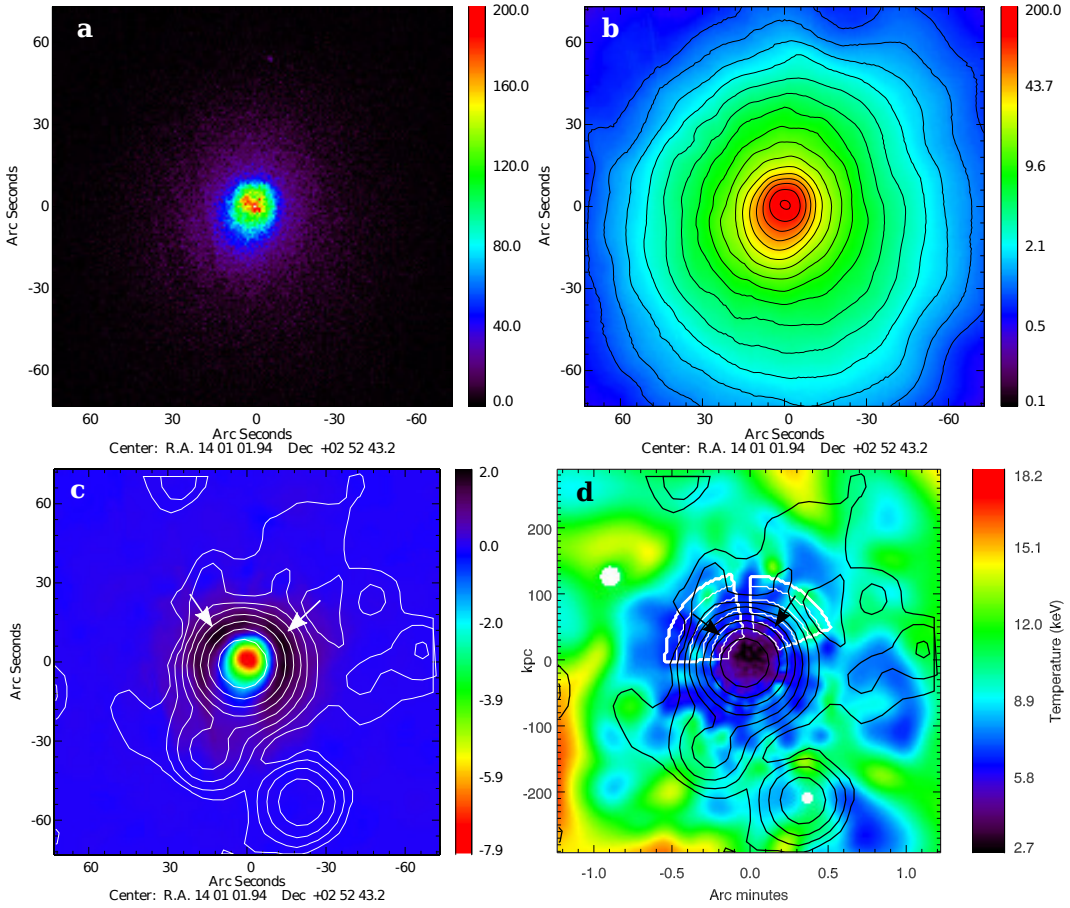

Figure 6.11: Chandra X-ray image in the [0.5,2.5] keV energy band (a), brightness map obtained by curvelet analysis with overlaid brightness contours (b), sum of MSVST curvelet coefficients with radio contours overlaid (c) and temperature map obtained by B2-spline wavelet analysis with radio contours overlaid (d) of A1835. 1.4 GHz VLA-C radio contours are logarithmically separated by a factor of 2 and start from a 3σ intensity level of 0.12 mJy/beam. The beam size is $18'' \times 18''$. X-ray brightness contours are logarithmically separated by a factor of $\sqrt{2}$ and has a resolution of $0.86''$. In panel (d) white sector annuli correspond to the sectors from where brightness and temperature profiles (as shown in figure 6.12) are extracted. The arrows show the locations of the CFs.

We tried to extract profiles from the regions across this ring. CF-like jumps in brightness and temperature were observed in two regions as shown in figure 6.12. There might be more than one CF in this cluster, one to the north-west and the other to the north-east. But both of them are approximately at the same radius from the centre, $r_j \sim 50$ kpc. Thus it might be speculated that they are part of an extended structure. Sanders et al. (2010) extracted brightness and temperature profiles (figure 5 of their paper) along spherically symmetric annuli in A1835. They found a temperature glitch at $r \sim 70$ kpc but no associated brightness jump. Inconsistency with our results might be because of the fact that we extracted profiles from specific sectors to the north of the centre.

Even though we do not see any CF to the south of the centre, we cannot dismiss

the possibility that the cool gas might be sloshing. While the first CF may form just ~ 0.3 Gyr after the core passage of the merging sub-cluster, the second CF can only be formed after ~ 0.6 Gyr (Johnson et al., 2012). Thus we can speculate that, the cool sloshing gas is just turning back towards the dark matter peak and when it encounters hotter ambient gas on the southern side of the cluster, another CF will form.

From the radio contours overlaid on the temperature map (figure 6.11[d]) we see that the MH emission is confined within the cool core. The CFs are indicated by arrows in panel (c) of the figure which suggests that the MH extends beyond the CFs. Spatial correlation between the CFs and the MH cannot be understood properly from our analysis as radio observation has a poor resolution.

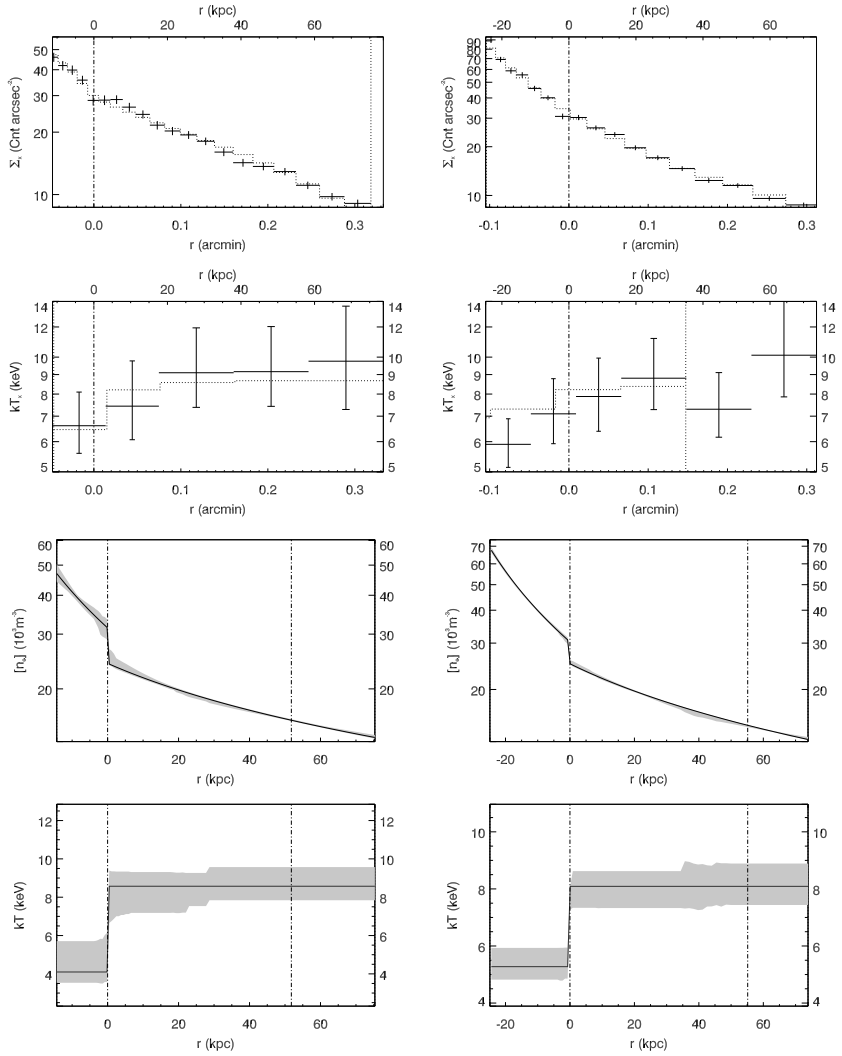

Figure 6.12: *From top to bottom*: Projected gas brightness (Σ_x), spectroscopic temperature (kT_x), and derived density (n_e) and temperature (kT) profiles corresponding to the sectors shown in figure 6.9(d). Profiles in the left and the right columns correspond to the North-West and North-East cold fronts of A1835, respectively. Dashed lines along the brightness and temperature profiles correspond to fits of the projected functions. The vertical dot-dashed lines indicate the positions of the CFs. Front modelling and fitting regions are bounded by the dot-dashed lines on the right.

Chapter 7

Conclusions

We have analysed X-ray observations of six galaxy clusters that host radio mini-halos (MH) and found a pair of cold fronts (CF) in each of the clusters. We correlated the X-ray data with the corresponding MH radio emission and observed that most of the MHs are confined within the regions delimited by the CFs. In some clusters the MHs are also spatially correlated with the X-ray spiral structure created by the gas sloshing. But the visibility of spiral structures is strongly affected by the inclination of the merger plane of the clusters. It is clearly visible only if the merger occurs in the plane of the sky.

Based on the strong correlation between the CFs and the MHs in MS1455 and R1720, Mazzotta & Giacintucci (2008) hypothesized that the relativistic electrons responsible for the MH radio emission can be re-accelerated by turbulence created by the cool gas that is sloshing in the cluster potential minimum. Through simulation Zuhone et al. (2012) found that the sloshing-induced turbulence is strong enough to re-accelerate relativistic electron seeds. Our observations of MS1455 and R1720 agree with that of MG08. Besides, the MH and the CFs are also correlated in R1347. In R1504, the north-west CF defines the northern boundary of the MH, but the southern CF is located inside the MH. A2029 also exhibits two CFs on opposite sides w.r.t the centre. Thus the cool gas must be sloshing in all of these five clusters which can re-accelerate electrons. In A1835, we found only the northern CFs. We can speculate that the sloshing gas did not have enough time to create another CF in this cluster.

Results of our new analyses are in agreement with that suggested by MG08, i.e. the relativistic electrons in MHs might be re-accelerated by the turbulence induced by the sloshing ICM gas.

Bibliography

Abell, G. O., 1958, ApJ Suppl., 3, 211

Allen, S. W., Ettori, S., Fabian, A. C., 2001, MNRAS 324, 877

Allen, S. W., Fabian, A. C. et al., 1996, MNRAS 283, 263-281

Ascasibar, Y., Markevitch, M., 2006, ApJ, 650, 102

Bacchi, M. et al., 2003, A&A 400, 465-476

Bartelmann, M., Schneider, P. 2001, Phys. Reports, 340, 291

Boehringer, H., Burwitz, V., Zhang, Y.-Y., et al., 2005, ApJ, 633, 148

Bourdin, H., Sauvageot, J.-L. et al., 2004, A&A, 414, 429-443

Bourdin, H. & Mazzotta, P., 2008, A&A 479, 307-320

Brunetti, G., Setti, G., Feretti, L., Giovannini, G., 2001, MNRAS, 320, 365-378

Brunetti, G., Blasi, P., Cassano, R., Gabici, S., 2004, MNRAS 350, 737

Candes, E. J., Donoho, D. L., 1999, in *Curves and Surfaces*, L. L. Schumaker et al. (eds), Vanderbilt University Press, Nashville, TN.

Cassano, Gitti, Brunetti, 2008, A&A, 486, L31

Churazov, E., Forman, W., Jones, C., Bhringer, H., 2003, ApJ. 590, 225

Clarke, T. E., Blanton, E. L. and Sarazin, C. L., 2004, ApJ, 616, 178-191

Clowe, D., Bradac, M., 2006, ApJ, 648:L109L113

Dolag, K., Ensslin, T. A., 2000, A&A 362, 151157

Donoho, D., 1993, Proceedings of Simposia in Applied Mathematics, 47

Feretti, L. et al., 2012, Astron. and Astrop. Rev. 20:54

Ferrari, C., Govoni, F. et al., 2008, Space Sci. Rev., 134, 93-118

Ferrari, C., Intema, H. T., 2011, A&A 534, L12

Fujita, Y., Matsumoto, T., Wada, K., 2004, ApJ 612, L9-L12

Furusho, T., N.Y. Yamasaki, T. Ohashi, R. Shibata, H. Ezawa, 2001, ApJ. 561, L165

Giacintucci, Markevitch, Brunetti et al., 2011, ApJ 525, L10

Gitti, M., Brunetti, G., Setti, G., 2002, A&A, 386, 456

Gitti, M., Brunetti, G. et al., 2004, A&A 417, 1-11

Gitti, M., Feretti, L. and Schindler, S., 2006, A&A 448, 3

Gitti, M., Ferrari, C. et al., 2007, A&A 470, L25-L28

Gitti, M., Piffaretti, R., Schindler, S., 2007, A&A 472, 383-394

Giacintucci, S., Markevitch, M. et al., 2011, A&A 525, L10

Giovannini, G., Feretti, L., 2000, New Astronomy, 5, 335-347

Govoni, F., Murgia, M. et al., 2009, A&A 499, 371-383

Johnson, R., Zuhone, J. et al., 2012, ApJ 751:95

Kaiser N. 1986. MNRAS 222:323345

Kraus, John D., 1986, Radio Astronomy (Cygnus-Quasar Books)

Kravtsov, A., Borgani, S., 2012, arXiv:1205.5556v1 [astro-ph.CO]

Mallat, S., 1998, A wavelet tour of signal processing (Academic Press)

Mallat, S., 1989, IEEE Trans. on Pattern Analysis and Machine Intelligence, 11, 7

Markevitch, M., et al., 2000, ApJ. 541, 542

Markevitch, M., Vikhlinin, A., Mazzotta, P., 2001, ApJ, 562, L153-L156

Markevitch, M., Vikhlinin, A., 2007, Phys. Reports, 443, 1-53

Mazzotta, P., Markevitch, M., Forman, W. R., Jones, C., Vikhlinin, A., VanSpeybroeck, L., 2001a, preprint (astro-ph/0108476)

Mazzotta, P., Markevitch, M., Vikhlinin, A., Forman, W. R., David, L. P., VanSpeybroeck, L., 2001b, ApJ 555, 205

Mazzotta, P., Markevitch, M., Forman, W. R., Jones, C., Vikhlinin, A., & VanSpeybroeck, L., 2001a, arXiv:astro-ph/0108476v1

Mazzotta, P., Markevitch, M., Vikhlinin, A., Forman, W. R., David, L. P., & VanSpeybroeck, L., 2001b, ApJ 555, 205

Mazzotta, P., Rasia, E., et al., 2004, MNRAS 354, 10-24

Mazzotta, P.; Giacintucci, S., 2008, ApJ 675, L9-L12

MacGillivray, H.T. Stobie, R.S., 1984, Vistas Astr., 27, 433

Murgia, M., Govoni, F. et al., 2009, A&A 499, 679-695

Murtagh, F., Starck, J.-L. and Bijaoui, A., 1995, A&A Supplement, 112, 179

Owers, M. S et al., 2009, ApJ 704, 1349-1370

Pfrommer, C., Ensslin, T. A., 2004, A&A 413, 17-36

Ricker, P., Sarazin, C., 2001, ApJ 561, 621-644

Roediger, E., Brueggen, M., Simionescu, A. et al., 2009, MNRAS, 1201, 317-320

Sanders, J. S., Fabian, A. C. et al., 2010, MNRAS, 402, L11L15

Sarazin, C. L., 1988, X-ray emission from clusters of galaxies, Cambridge University Press

Sarazin, Craig L., Baum, Stefi A., O'Dea, Christopher P., 1995, ApJ, 451, 125

Selesnick, I. W., 2007, Physics Today, October 2007

Sharma, P., Chandran, B. D. G. et al., 2009, ApJ 699, 348361

Shechtman, S.A., Landy, S.D., Oemler, A., Tucker, D.L., Lin, H., Kirschner, R.P., Schechter, P.L., 1996, ApJ, 470, 172

Slezak, E., Durret, F. and Gerbal, D., 1994, Astronomical Journal 108, 6, 1996-2008

Starck, J.-L. and Pierre, M., 1998, A&A Supplement, 128, 397-407

Starck, J.-L., Donoho, D. L. and Candes, E. J., 2003, A&A 398, 785-800

Starck, J.-L., Pires, S and Réfrégier, A., 2006, A&A, 451, 3, 1139-1150

Starck, J.-L., Fadili, J. and Murtagh, F., 2007, IEEE Trans. on Img. Proc. 16, 2

Starck, J.-L., Fadili, J. et al., 2009, A&A 504, 641-652

Venturi, T., Giacintucci, S. et al., 2008, A&A 484, 327340

Vikhlinin, A., Markevitch, M., Murray, S. S., 2001, ApJ, 551, 160-171

Zhang, B., Fadili, J. and Starck, J.-L., 2008, IEEE Trans. on Img. Proc. 17, 7

Zuhone, Markevitch, Brunetti, Giacintucci, 2012, arxiv:1203.2994, submitted to ApJ

Zwicky, F. 1937, ApJ, 86, 217

Zwicky, F., E. Herzog, P. et al., 1961 - 1968, *Catalogue of galaxies and clusters of galaxies*, Vol. 1-6, Pasadena: Caltech